UNIVERSIDADE DE LISBOA
FACULDADE DE MEDICINA

How nuclear envelope grows old: exploring the biomechanical features of the nucleus during Human Aging

Francisco Xavier Santos Rocha

Orientadores: Dr. Maria João Martins Sarmento
Prof. Dr. Nuno Fernando Duarte Cordeiro Correia dos Santos

Dissertação especialmente elaborada para a obtenção do grau de Mestre em Investigação Biomédica

2024

UNIVERSIDADE DE LISBOA
FACULDADE DE MEDICINA

How nuclear envelope grows old: exploring the biomechanical features of the nucleus during Human Aging

Francisco Xavier Santos Rocha

Orientadores: Dr. Maria João Martins Sarmento
Prof. Dr. Nuno Fernando Duarte Cordeiro Correia dos Santos

Dissertação especialmente elaborada para a obtenção do grau de Mestre em Investigação Biomédica

2024

A impressão desta dissertação foi aprovada pelo Conselho Científico da Faculdade de Medicina de Lisboa em reunião de 5 de dezembro de 2024.

INDEX

Acknowledgements

First and foremost, I would like to express my gratitude to my supervisor, Maria João, for all the knowledge shared and for giving me the opportunity to work with her. It has been a pleasure learning from you. Thank you for giving me the freedom from the beginning to the end to experiment with everything I wanted, without ever holding me back. It was with that freedom that I now leave this master's program not only with a suitcase full of headaches from reaching dead ends at times but, above all, with a suitcase full of lessons and knowledge. A special thanks also to my co-supervisor, Nuno Santos, for welcoming me into his lab and allowing me to experience what it's like to work in a cutting-edge laboratory with abundant resources. I leave now, slightly spoiled by the experience.

My second thanks go to all my lab colleagues. To Nelly, for being the special person you are; to Pedro, for being the coolest postdoc; to Joana, for being the best lab manager in the world; to Filomena, for all the time spent with me on AFM; to Catarina, for all the patience and for being my companion during the less appropriate lab hours; and especially to Aivaras, Inês, Tomás, Renata, and Teresa, for the much-needed and precious coffee breaks, and for always knowing what to say during the toughest moments. I carry you all in my heart.

I cannot forget to thank all the facilities and technical staff who helped me complete this work. To the TEM facility at IGC, especially Dr. Ana Sousa; to the bioimaging facility at iMM for their unconditional support; to Professor Fábio Fernandes from iBB at IST for giving me the opportunity to use his microscope and FLIM; and, above all, to the technicians Rute, Andreia, Margarida, and Mariana, the Head of the flow cytometry facility at iMM. Words cannot express my gratitude for your kindness, patience, and work with me. I can only apologize for overloading you and making you endure the worst sorting at iMM.

Finally, the most important and special thanks. Thank you, Mom, brother, and sister, for all the support, help, patience, sustenance, and love. If I am reaching the end of this stage today, it is largely because of you, for the support and care you have always given me. I can never repay you enough. Thank you to the Simões cousins for allowing me to live in your dream house during these years. Thank you to Hugo and Raquel, who started as master's colleagues and now end up as lifelong friends! Thanks to my lifelong friends, especially Filipa, for pulling me out of the lab when I needed it most, for making me enjoy Lisbon, and for continuing to be

a friend for all occasions, and to Tó Zé, for keeping me company while writing this thesis and for showing me that if it's true friendship, no matter how many years pass, nothing changes. Thanks to group 9(1)1, proof that college friends can last a lifetime, who, even from afar, always made a point to stay close.

Near the end, I cannot forget to thank the Moinho family. To Pe Filipe, for everything and more, and even more, you will never know how much you helped me. To Pe Rui, for being the person you are, the example you have always been, and for instilling in me the desire to always seek more knowledge. To Ir. Natália, for the affection and prayers that were fundamental in helping me reach the end. To Matilde and Margarida, the new big sisters I gained—thank you for being examples and role models. To Madalena and Maria, for being a source of joy and for all the smiles you brought me this year, from places I didn't even know I had them. To Filipe and Carolina, for teaching me that there is always time for others, always room for one more, and that in everything we do, we should give our best and take the utmost care. To João Adão and João Paulo Rodrigues, for the companionship, the hugs, and for teaching me that you don't need to be physically present to be a friend. To Margarida Gaspar, João, and Sara, for showing me how wonderful it is to belong to a family, where you draw strength to wake up the next day and try again. Lastly, thanks to the other friends from the Seminary, Pe Miguel, the Pereira family, the Dona Maria's family, the Beja family, Daniel and to all the seminarians. You are crazy, beyond epic!

Finally, to all the guiding and shining stars in the sky, especially the most special one of all, thank you.

To everyone who helped me throughout these years.

"Tudo posso naquele que me fortalece" (Fl 4, 13)

Extra-curricular activities and communications

- Activities

Creation of the Biophysics Club at the Institute of Molecular Medicine

Organisation of the first Biophysics Networking Event in Portugal sponsored by the Biophysical Society – April 11, 2024

Member of the Portuguese Young Biophysicists – 2023-2024

Organisation of the 4th Meeting of the Young Biophysics Festival – May 9-10, 2024

Image Analysis and Macro Scripting in ImageJ Courses – COLife – March 4-6, 2024

Python Initiation Course - coursera

- Communications

Rocha FS, Sarmento MJ, Santos NC (2024), Portugal, *Bridging the Ggap: Nuclear Biomechanics in the Ageing Puzzle*, 4th Meeting of the Young Biophysics Festival, Covilhã

Sarmento MJ, Vilutis A, Rocha FS, Kohutova P, Hof M, Santos NC (2024), Germany, *Nuclear Envelope Ether Lipids in Human Healthy Aging*, DGfB Meeting of Membrane Biophysics, Drübeck, Germany.

Abstract

The nuclear envelope (NE) is a fundamental cellular structure responsible for maintaining genomic stability and regulating various nuclear-cytoplasmic interactions, which are critical for proper cellular function. However, the ageing process leads to profound alterations in the NE, contributing to the decline in cellular function and the onset of age-related diseases. This thesis aims to elucidate the biomechanical and biophysical changes that occur in the NE during human ageing, focusing on the interplay between nuclear stiffness, membrane tension, lipid composition, and Lamin A dynamics. By integrating advanced techniques such as Atomic Force Microscopy (AFM), Confocal Microscopy, and Fluorescence Lifetime Imaging Microscopy (FLIM), this research provides a comprehensive analysis of how these properties evolve with age.

A key achievement of this study is the development of a robust, detergent-free protocol for the isolation of nuclei from primary human fibroblasts, preserving the structural integrity of the NE. The results demonstrate that ageing is associated with increased nuclear stiffness, which may be driven by alterations in Lamin A processing and distribution, as well as changes in membrane tension and order. These biomechanical changes are hypothesized to impair NE flexibility and its ability to maintain nuclear key functions, contributing to cellular senescence and age-related pathologies.

In addition to characterising these age-related changes, this thesis sets the initial foundations for the use of Large Unilamellar Vesicles (LUVs) as a model to mimic the aged nuclear environment. By isolating lipids from aged nuclei and using them to form LUVs, this work provides a novel platform for studying the specific contributions of lipid alterations to NE mechanics in a controlled setting. These findings not only advance our understanding of nuclear ageing but also highlight potential targets for preventive interventions aimed at preserving nuclear function and promoting healthy ageing.

Keywords: ageing, nuclear envelope, lipids, lamin A, biomechanical properties

Resumo

O envelhecimento é um processo biológico complexo que afeta todas as células, tecidos e órgãos do corpo, levando a uma diminuição progressiva da capacidade funcional e aumentando a suscetibilidade a doenças. Este fenómeno resulta da acumulação gradual de danos moleculares e celulares ao longo do tempo, causados por uma variedade de fatores, como o stress oxidativo, a disfunção mitocondrial, diminuição dos telómeros, instabilidade genómica, perda da proteostase, entre outras. O envelhecimento também está associado à deterioração das funções dos mecanismos de reparo celular e à redução da capacidade regenerativa dos tecidos, particularmente devido à senescência celular — um estado em que as células perdem a capacidade de se dividir e de desempenhar as suas funções naturais. Assim, o envelhecimento para além de ser um processo biológico inevitável, é também um dos principais fatores de risco para o desenvolvimento de doenças crónicas, como as doenças cardiovasculares, neurodegenerativas, e diversas formas de cancro, exigindo uma compreensão mais profunda dos seus mecanismos subjacentes para o desenvolvimento de intervenções terapêuticas eficazes. Neste projeto, a nossa atenção centra-se no núcleo das células, estrutura particularmente interessante no contexto do envelhecimento, e numa caraterística específica, as alterações das propriedades mecânicas do núcleo.

O Envelope Nuclear (EN) é uma estrutura essencial do núcleo, é responsável por isolar o conteúdo nuclear do citoplasma e manter a estabilidade do genoma. Além da sua função como barreira física, o EN regula interações nucleocitoplasmáticas, como o transporte de proteínas e ARN, a organização cromossómica e a resposta a sinais celulares. Alterações significativas na estrutura e função do EN surgem com o envelhecimento, associadas à perda de funcionalidade celular e ao desenvolvimento de doenças relacionadas com a idade, como a Progeria de Hutchinson-Gilford (HGPS) e outras laminopatias. Estas doenças são muitas vezes usadas como modelos para estudar o envelhecimento.

Esta tese visa explorar as mudanças biomecânicas e biofísicas que ocorrem no EN ao longo do envelhecimento, com foco na rigidez nuclear, tensão e ordem da membrana nuclear, e dinâmica da Lâmina A. Para isso, foi desenvolvida uma abordagem multidisciplinar que integra técnicas avançadas de microscopia e criação de modelos de membrana *in vitro*. As técnicas empregadas incluem a Microscopia de Força Atómica (AFM) para avaliar a rigidez do EN, a Microscopia Confocal para observar a organização estrutural da Lâmina A e a ordem da membrana nuclear e a Microscopia de Tempo de Vida de Fluorescência (FLIM) para investigar a tensão da membrana.

Um dos principais resultados foi o desenvolvimento de um protocolo sem detergentes para isolar núcleos de fibroblastos humanos primários, preservando a integridade do EN. Este protocolo permitiu estudar as propriedades biofísicas do EN em condições mais próximas ao ambiente fisiológico, fundamentais para compreender como as alterações biomecânicas poderão afetar a funcionalidade celular. Observou-se que o envelhecimento provoca um aumento significativo na rigidez do EN, o que pode estar relacionado com mudanças no processamento e distribuição da Lâmina A. A Lâmina A, componente essencial da lâmina nuclear, confere suporte estrutural ao EN e a sua desregulação durante o envelhecimento pode resultar num EN mais rígido e menos adaptável às exigências celulares.

Outro achado relevante refere-se às medições de tempo de vida de fluorescência, que revelaram uma associação entre envelhecimento e aumento da tensão na membrana nuclear. Essa maior tensão, junto com a rigidez, pode comprometer a capacidade celular de responder a deformações mecânicas, influenciando o transporte de materiais entre o núcleo e o citoplasma, bem como a organização da cromatina. Adicionalmente, observou-se um aumento da ordem lipídica na membrana nuclear de células envelhecidas. Estas mudanças sugerem uma diminuição da flexibilidade necessária para manter a integridade nuclear, contribuindo para a senescência celular.

Este estudo também identificou uma conexão entre alterações no EN e doenças relacionadas ao envelhecimento. Em células de pacientes com HGPS, foram identificadas mudanças que se assemelham às observadas no envelhecimento saudável, como desorganização da Lâmina A e aumento da rigidez nuclear. A correlação entre a rigidez do EN e a disfunção da Lâmina A sugere que o envelhecimento saudável e as laminopatias compartilham mecanismos biológicos semelhantes.

Além de caracterizar estas alterações em células envelhecidas e em células de pacientes com HGPS, esta tese avança no desenvolvimento de modelos *in vitro* para estudar o EN em ambientes controlados. Um avanço significativo foi o uso de Vesículas Unilamelares Grandes (LUVs) para mimetizar o EN envelhecido. Ao isolar lipídios de núcleos de dadores idosos e usá-los para formar LUVs, foi possível criar um modelo simplificado para estudar as propriedades da membrana nuclear envelhecida. Este modelo poderá ser utilizado como uma plataforma inovadora para investigar como as mudanças lipídicas contribuem para as propriedades mecânicas do EN e o envelhecimento nuclear.

As observações deste estudo destacam a importância da composição lipídica e da Lâmina A na manutenção da funcionalidade do EN. Intervenções que preservem a organização da Lâmina A e a homeostase lipídica podem potencialmente retardar os efeitos do envelhecimento

no EN. Dado o papel central do EN na regulação de funções celulares essenciais, estas intervenções poderiam ter implicações significativas na promoção de um envelhecimento saudável e no desenvolvimento de terapias contra doenças relacionadas ao envelhecimento.

Por fim, este trabalho sugere que estudos futuros devem focar em ampliar as investigações para células intactas, tanto de dadores jovens quanto idosos, bem como aumentar o número de pacientes com HGPS no estudo. Validar os resultados dos núcleos isolados em contexto celular permitirá avaliar se as alterações mecânicas e biofísicas observadas no EN se mantêm no ambiente celular completo. Este esforço contínuo ajudará a confirmar as conclusões desta tese e a direcionar o desenvolvimento de terapias para restaurar a função nuclear em células envelhecidas, potencialmente melhorando a qualidade de vida em estádios avançados da idade.

A modulação da composição lipídica e da dinâmica da Lâmina A poderá abrir caminho para novas abordagens terapêuticas, capazes de preservar a integridade funcional do núcleo em células envelhecidas. Essas estratégias podem resultar em tratamentos inovadores que, ao estabilizarem a organização do envelope nuclear, reduzam o risco de doenças associadas à sua disfunção.

Outro exemplo promissor é o uso de nanomedicina para introduzir lípidos específicos na membrana nuclear, visando restaurar a fluidez e elasticidade da mesma. A encapsulação de lípidos em nanopartículas direcionadas pode permitir uma distribuição precisa e controlada, com potenciais benefícios para a reversão de disfunções ligadas ao envelhecimento celular.

Para além disso, paralelamente, o uso de ferramentas de edição genética, como a correção de mutações na Lâmina A e noutras proteínas do EN, representa uma área de investigação emergente com grande potencial terapêutico. Em conjunto, estas estratégias não só ambicionam tratar doenças associadas ao envelhecimento, mas também contribuir para uma melhoria significativa na qualidade de vida em idades avançadas, abrindo um novo horizonte na medicina regenerativa.

Além disso, há uma necessidade crescente de aprofundar o estudo das interações entre os componentes do EN e outras estruturas, como o citoesqueleto, para entender melhor como o envelhecimento afeta a integridade global da célula. O EN não atua isoladamente e as suas funções estão intimamente ligadas a redes celulares complexas. Alterações nas suas propriedades mecânicas e biofísicas podem ter um efeito cascata, destabilizando outras estruturas celulares e contribuindo para o declínio funcional observado no envelhecimento. Estudos futuros que utilizem técnicas de imagem de alta resolução e modelos computacionais podem fornecer novas ideias sobre essas interações dinâmicas e identificar pontos de intervenção que possam preservar a homeostase celular como um todo.

Palavras-chave: envelhecimento, envelope nuclear, lípidos, lamin A, propriedades biomecânicas

Abbreviations

AFM - Atomic Force Microscopy

Chol - Cholesterol

DPPC - 1,2-dipalmitoyl-sn-glycero-3-phosphocholine

ECM - Extracellular Matrix

ER - Endoplasmic Reticulum

FLIM - Fluorescence Lifetime Imaging Microscopy

HB - Hypotonic Buffer

HGPS - Hutchinson-Gilford Progeria Syndrome

INM - Inner Nuclear Membrane

LADs - Lamin Associated Domains

LA - Lamin A

Laurdan - 1-(6-(dimethylamino)naphthalen-2-yl)dodecan-1-one

LUVs - Large Unilamellar Vesicles

NE - Nuclear Envelope

NL - Nuclear Lamina

NPC - Nuclear Pore Complexes

ONM - Outer Nuclear Membrane

PC - Phosphatidylcholine

PE - Phosphatidylethanolamine

POPC - 1-palmitoyl-2-oleoyl-glycero-3-phosphocholine

preLA - Prelamin A

Rhod-DOPE - 1,2-dioleoyl-sn-glycero-3-phosphoethanolamine-N-(lissamine rhodamine B sulfonyl) (ammonium salt)

SM - Sphingomyelin

TEM - Transmission Electron Microscopy

1. INTRODUCTION

1.1. Ageing

The idea of the "arrow of time", as proposed by the astronomer Arthur Eddington, suggests that increasing entropy determines the direction of time's flow – a captivating and simple idea that may be used to tell us what ageing is.

However, defining ageing is not that simple. Is a challenge comparable to comprehending the complexities of the brain, exploring the ocean's deepest depths, or measuring the vast expanse of the universe. The question is: why is this like that, and will it always remain so? However, presently, we lack the necessary tools and knowledge to fully address questions such as: why do we age in this manner and not otherwise? Why can our cells perform complex tasks and then struggle with simpler ones? We lack the tools and the knowledge to fully understand the minute details of systemic alterations, cellular changes, and molecular interactions (or their absence) that underlie the complex and intricate mechanisms of ageing. Another reason defining ageing is so challenging is that it can be considered from numerous perspectives, including social, behavioural, physiological, morphological, cellular, and molecular changes.

Nevertheless, this first chapter compiles various theories and attempts to explain what ageing is and why it occurs. Additionally, it addresses the importance of continuing to study ageing.

1.1.1. Defining Ageing

In 1956, Alex Comfort, in his book *The Biology of Senescence*, suggested that ageing is a progressive increase throughout life, or after a specific age, in the likelihood that an individual will die during the next unit of time from randomly distributed causes [1]. In 1981, Harman suggested that aging involves the gradual buildup of changes over time, which are linked to or contribute to the growing vulnerability to illness and death as age progresses [2]. By 1991, the book *Evolutionary Biology of Ageing* described ageing as a persistent decline in the age-specific fitness components of an organism due to internal physiological deterioration [3]. In 2000, Scott F. Gilbert´s *Developmental Biology* characterised ageing as a time-related deterioration of the physiological functions necessary for survival and fertility, affecting all individuals of a species [4]. More recent definitions have incorporated various hallmarks of ageing (see section *1.2.1*) [5]. Over the decades, the definition of ageing has evolved, incorporating elements from the accumulation of random changes to reproduction and finally to observable modifications (known as ageing hallmarks).

Nowadays, the consensus among scientists is that ageing is a physiological and universal process experienced by all individuals, albeit at varying rates and with a lack of uniformity, characterised by molecular-level degeneration that progresses to cellular and, consequently, tissue alterations, culminating in systemic deregulation [6].

Nevertheless, the question remains: Why do we age?

1.1.2. Why do we age?

An early hypothesis for the evolution of ageing proposed that senescence was programmed to limit population size or expedite generational turnover, thereby enhancing organismal adaptation to changing environments [7]. However, in natural settings, there is minimal evidence that senescence significantly contributes to mortality, as wild animals typically do not live long enough to experience old age. Thus, natural selection has limited influence over the process of senescence [8].

The rarity of aged animals in the wild suggests a key principle underlying current evolutionary theories of ageing. Due to extrinsic mortality factors (predation, starvation, environmental factors not under the control of the individual, among others), the force of natural selection weakens with increasing age [8]. Once wild survivorship declines to very low levels, selection cannot effectively counteract the accumulation of late-acting deleterious germ-line mutations. This principle is central to the *mutation accumulation* theory, which posits that these unselected deleterious alleles accumulate, leading to considerable genetic variation among individuals within a population [8].

Another prominent theory is *antagonistic pleiotropy*, proposed by Williams [8]. This theory suggests that genes with beneficial effects early in life are favoured by natural selection, even if they have harmful effects later on. The early-life fitness advantages provided by such genes outweigh their late-life detriments, even leading to senescence and death. This concept introduces life-history trade-offs, which are also very important to the *disposable soma* theory. This theory focuses on the optimal allocation of resources between somatic maintenance and reproduction. For example, since over 90% of wild mice die within their first year, investing in survival mechanisms beyond this age benefits only a small fraction of the population. Therefore, mice prioritise resources for thermogenesis and reproduction over repair mechanisms, resulting in ageing [8].

Contrary to these genetic theories, some scientists argue that ageing might not be genetically programmed. They draw analogies to mechanical engineering, where "mean time to failure" describes the average lifespan of devices before they require major repairs. This

concept is similar to human life expectancy, which historically was about 30 years until recent advances in civilisation extended it to around 75 years [9]. They argue that, since there was no selective advantage for the survival of older humans throughout most of human history, biological ageing might be an artefact of civilisation since, unlike wild animals, humans have learned to avoid natural causes of death long after their reproductive years [9].

However, as mentioned before, ageing can be approached from multiple perspectives, ranging from those that focus on human perception, such as theological, philosophical, and sociological viewpoints, to more empirical domains like biomedical research, molecular biology, and gerontology. This multidisciplinary interest has led to numerous explanations for why ageing occurs, each dependent on the specific field of study. For instance, geneticists may attribute ageing to genetic factors, while biogerontologists might focus on the biological and physiological processes involved.

Consequently, the scientific community has shifted from questioning why we age to investigating why humans have the lifespan they do [9]. This reframing of the inquiry allows researchers to design experiments to gain deeper insights into the fundamental nature of ageing and longevity.

Nonetheless, regardless of the area of study or expertise, one undeniable fact for all sciences is that ageing leads to changes in the body, some of which are apparent even to the naked eye.

1.1.3. Ageing consequences

As individuals age, a multitude of physiological changes occur beyond the need for reading glasses, greying hair, and stiff joints. For instance, the body's capacity to retain fluids diminishes, leading to the shrinkage and loss of elasticity in spinal discs, which results in a decrease in height over time [10]. Beginning at around age 55, there is an accelerated loss of muscle mass, and the body's muscle-to-fat ratio shifts, often leading to weight gain [11]. Additionally, organs such as the kidneys and liver experience a decline in functionality, thereby slowing the body's detoxification processes [12]. Figure 1.1 illustrates a summary of additional changes associated with the ageing process.

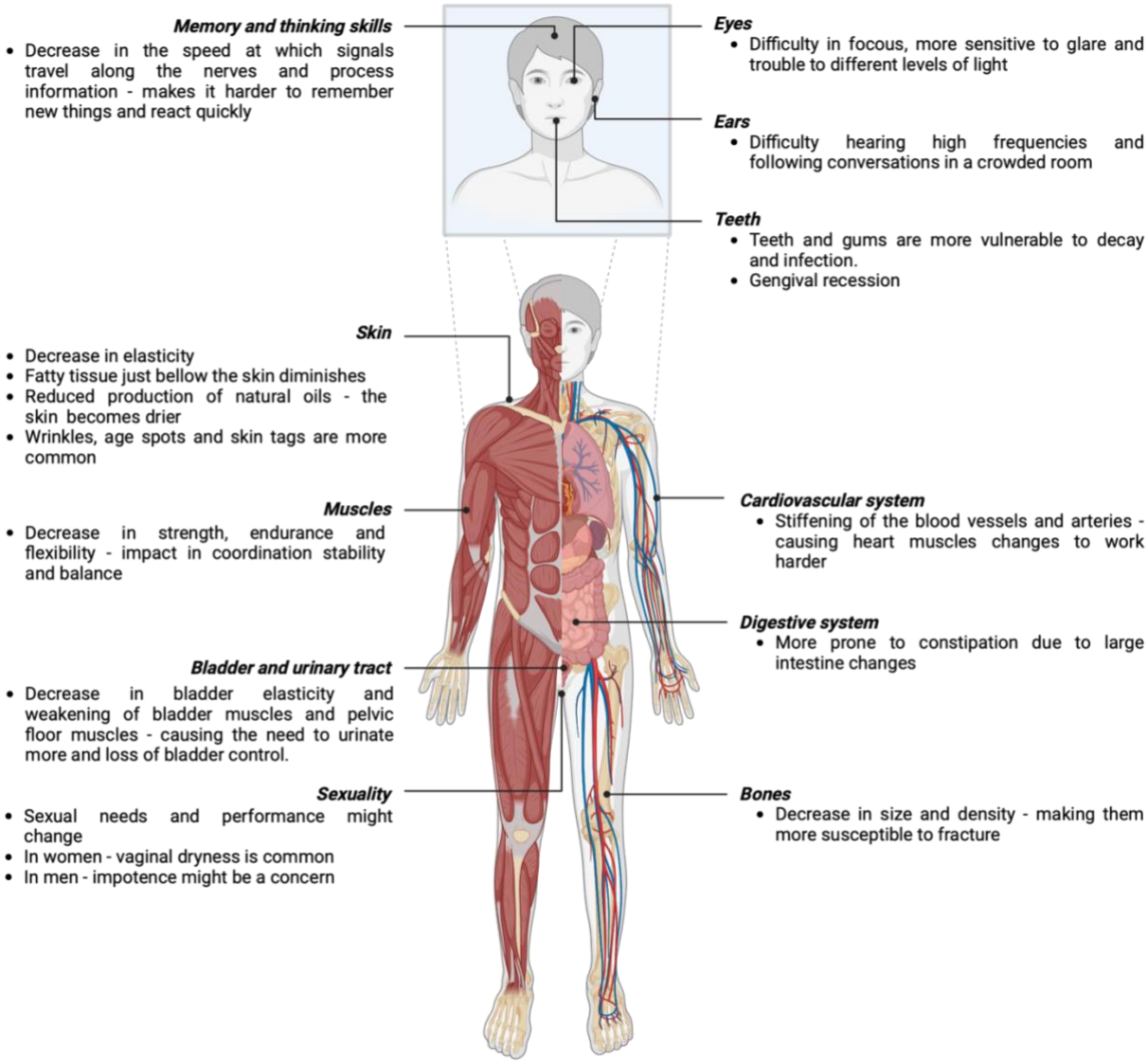

Figure 1.1 Age-related alterations in the body. Ageing impacts multiple organs and systems; here are some examples of the changes the human body experiences as we grow old. These changes encompass complications in the nervous system, and alterations in sensory organs, such as eyes, ears and mouth, and extend to issues with the skin, muscles, and bones. Furthermore, ageing presents challenges in the cardiovascular, and digestive systems, along with impacts on sexual and bladder functionalities.

Moreover, as we age, we become more susceptible to serious and potentially life-threatening conditions like cancer, neurodegenerative disorders, and cardiovascular diseases, since ageing is the most significant risk factor for most chronic diseases [13, 14].

Taking this into account, is important to explain what healthy ageing is, and how can we define it.

1.1.4. Healthy Ageing

Healthy ageing can be divided into multiple subdomains, however, for the purposes of this thesis, it will be addressed as a whole.

Given the potential variations in individual ageing rates and the continually increasing life expectancies, the concept of healthy aging emerged as the ideal model for biological, sociological, and physiological development throughout one's lifespan. Historically, healthy ageing has been referred to through various lenses, including successful, healthy, productive, or active ageing, but defining it - and the process of ageing itself - is complicated [12, 15–17].

The World Health Organization (WHO) defines healthy ageing as a continuous process of optimising opportunities to maintain and enhance physical and mental health, independence, and quality of life throughout one’s life [15].

The concept of healthy ageing has evolved significantly over time, shaped initially by negative views of ageing until the 1960s, which portrayed it as a decline towards death. Shifts towards more positive perspectives began with theories like Havighurst's Activity Theory [6], emphasising active engagement in later life. Definitions such as Rowe and Kahn's distinction between "usual" and "successful" ageing further refined the idea, focusing on maintaining high function despite age-related changes [6].

Subsequent concepts like selective optimization with compensation and broader definitions by Schmidt and others aimed to make successful ageing more inclusive, acknowledging the challenges of perfect health in older age. This includes staying physically, mentally, and socially active, effectively managing chronic diseases, and sustaining a high quality of life [6, 16]. Conversely, unhealthy ageing is marked by significant declines in physical and mental health, often exacerbated by chronic conditions, reduced mobility, cognitive impairment, and social isolation, collectively diminishing an individual's quality of life and independence. However, it is critical to note that healthy ageing does not equate to the absence of diseases but rather the adept management of health conditions and the maintenance of functional abilities [17].

The Decade of Healthy Aging (2021-2030), declared by the United Nations General Assembly in December 2020, represents a major global strategy to build a society inclusive of all ages. This initiative unites the efforts of governments, civil society, international agencies, professional groups, academia, the media, and the private sector to enhance the lives of older individuals, their families, and their communities [18].

Ongoing research and advancements in understanding and measuring are essential for the progression of the healthy ageing concept, ensuring it not only includes longevity but also quality of life and resilience in later years [19].

As we attempt to enhance the quality of life for the elderly, it becomes increasingly crucial to continue studying ageing. Continued research is essential for uncovering new insights and developing effective health interventions that can enhance the quality of life and address the unique health challenges faced by an ageing population.

1.1.5. Why is it important to continue studying ageing?

Over the years, there has been a global trend towards increased longevity, with projections indicating that by 2030, the population of individuals aged 60 and older will surpass that of youth and double the number of children under five [20]. In the European Union (EU), the population is expected to peak at 453 million in 2026 before declining to 432 million by 2070, with an anticipated overall increase in the average age and the proportion of older individuals across all Member States (Figure 1.2) [21].

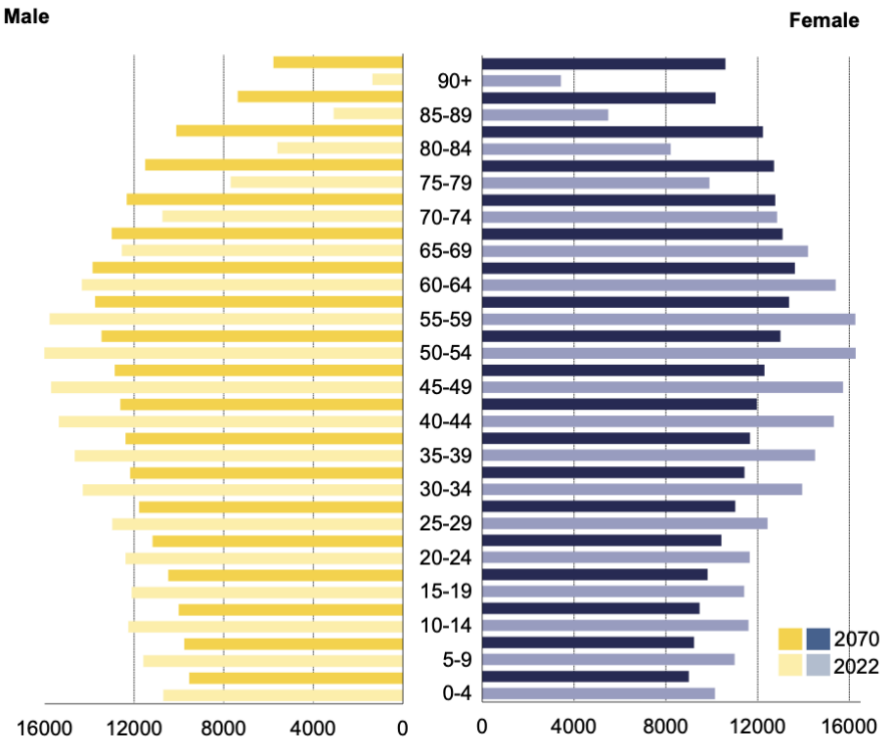

Figure 1.2 Projections of the population growth (thousands) per age group and gender in the European Union from 2022 to 2070 [21].

As depicted in Figure 1.2, the demographic shift will see a growth in older age brackets, while younger age brackets diminish. This shift impacts not only healthcare but also economic,

political and social sectors, among others. Recalling the recent pandemic, the increased fatality rates among older populations highlighted ageing as a significant risk factor for disease and mortality.

For this reason, it is important to continue studying ageing, not necessarily for an increase in lifespan but to enhance healthspan, which is an extended period of good health and well-being during later years. Existing healthcare and treatments are in place to treat patients and prolong their lives by controlling disease and relieving the symptoms of ageing. Still, these measures do not reverse the decline in the overall health of these patients, leading to a reduction in mortality but not in morbidity [22]. As a result, the human healthspan does not match the rising life expectancy, causing older adults to suffer from numerous chronic illnesses for longer periods rather than enjoying their lives to the fullest.

The following sections will delve into cellular components that influence the ageing process. Zooming in from the cell to the nucleus, emphasis will be placed on nuclear structures and molecules, touching on aspects of the most well-studied premature ageing disease, Hutchinson-Gilford Progeria Syndrome (HGPS). Although not molecularly equivalent to ageing, HGPS partially replicates some of its underlying mechanisms and has been widely used as a cellular model for studying physiological ageing.

1.2. Cell

All living organisms consist of cells, which are small units enclosed by a membrane, containing a concentrated aqueous solution of chemicals (cytosol). These cells possess the remarkable ability to replicate themselves by growing and dividing into two [23].

The cell theory, formulated in the mid-nineteenth century by Theodor Schwann, Matthias Jakob Schleiden, and Rudolf Virchow, asserts that all organisms are composed of at least one cell and that all cells originate from preexisting ones [24]. Vital functions of an organism occur within cells, and these structures harbour the hereditary information necessary for regulating their functions and transmitting this information to the next generation [23].

There are two types of cells: eukaryotic and prokaryotic. Eukaryotic cells, unlike prokaryotic ones, contain various membrane-bound organelles. These organelles compartmentalise the cells and create optimal conditions for different metabolic reactions [25].

Recent advances in cellular biology have significantly deepened our understanding of the contribution of cells and their organelles in the ageing process, particularly through the identification of fourteen cellular and molecular hallmarks of ageing. These hallmarks, which outline key mechanisms of cellular dysfunction, have shed light on the complex relationship

between ageing and age-related diseases. Their identification has also provided a framework for developing interventional and therapeutic strategies aimed at mitigating the effects of ageing.

1.2.1. Cellular and molecular hallmarks of ageing

Understanding the mechanisms of the ageing process is pivotal to treating the root cause of multiple age-related diseases. Figure 1.3 shows the set of ageing hallmarks that are currently identified due to extensive research on this topic.

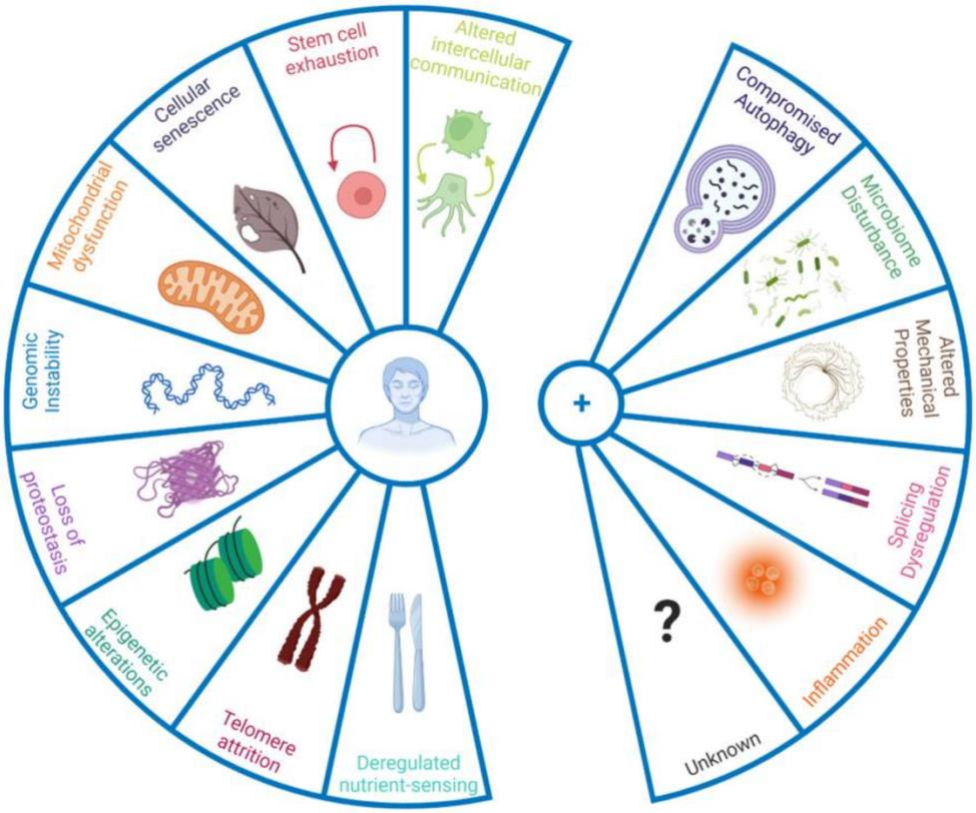

Figure 1.3 Ageing hallmarks. Latest compilation of the fourteen hallmarks associated with ageing that includes (left) the original nine hallmarks of ageing proposed by López-Otín in 2013 [3] (deregulated nutrient-sensing, telomere attrition, epigenetic alterations, loss of proteostasis, genomic instability, mitochondrial dysfunction, cellular senescence, stem cell exhaustion and altered intercellular communication), and (right) the five newly added hallmarks (compromised autophagy, microbiome disturbance, altered mechanical properties, splicing dysregulation, and inflammation). There is also an open door for future hallmarks since this is a field with continuous research where new information is discovered every day [4].

In this project, our focus is on the specific hallmark of Altered Mechanical Properties, as detailed below.

1.2.1.1. Altered Mechanical Properties

Altered mechanical properties are a fundamental hallmark of cellular ageing, encompassing changes in both intracellular structures and the extracellular environment. These mechanical alterations influence various cellular processes, including cell motility, signal transduction, and the maintenance of structural integrity within tissues, thereby contributing to age-related functional decline and disease [26]. The nucleus, cytoskeleton, and the extra cellular matrix (ECM) are particularly affected, with their mechanical properties playing a critical role in the ageing process [27].

In cellular ageing, fibroblasts, for example, undergo a significant transition in their mechanical structure. Senescent fibroblasts shift from a dynamic pool of actin, which is typically polymerised and depolymerised during cell movement, to stable stress fibres of F-actin, anchored through focal adhesions to the substrate [28]. This change is especially pronounced in patients with premature ageing symptoms and likely affects cell motility and communication. Altered cell motility is also relevant to the ageing of the innate immune system. Neutrophils from older donors, for instance, cause significant tissue damage when migrating to sites of inflammation. Modifying small G protein signalling pathways that regulate cytoskeletal motility through statin treatment has been shown to significantly improve the function of older neutrophils *in vitro* and reduce six-month mortality rates in older adults admitted to the ICU with pneumonia [28].

Similarly, the nucleoskeleton experiences ageing-related alterations, leading to the destabilisation of the nuclear lamina and the extrusion of chromatin into the cytoplasm as cytoplasmic chromatin fragments. These fragments trigger the senescence-associated secretory phenotype, contributing to cellular dysfunction. The nuclear lamina is notably defective in HGPS, and clinical trials with farnesyl transferase inhibitors have demonstrated improved nuclear envelope integrity and increased patient lifespan [28].

In addition to changes within the cell, the ECM also undergoes significant modifications with ageing. Increased rigidity and loss of elasticity, often due to glycation cross-links between collagen molecules, contribute to age-related diseases such as hypertension and related kidney and neurological defects. These cross-links may also play a role in the accelerated ageing observed in diabetic patients [27, 28].

While the composition and chemistry of the ECM determine tissue mechanical properties, their role in ageing and age-related diseases has been underappreciated. Mechanobiology, which explores the impact of mechanical stimuli on various cellular characteristics such as

shape, movement, and gene expression, protein regulation, cell growth, is shedding light on how the stiffness or elasticity of the environment influences cellular behaviour [27]. Cells respond to a rigid environment by stiffening their cytoskeleton and nucleoskeleton. As a result, the study of mechanobiology, particularly in the context of ageing, holds great potential for future rejuvenation research [27].

The nucleus is particularly significant in ageing, as it is associated with several hallmarks such as genomic stability maintenance, telomere dynamics, and mechanical properties [27]. Below we explore in further detail the role of the nucleus and its association with the loss of mechanical properties during ageing.

1.3. Nucleus

The nucleus was the first intracellular structure discovered. It has attracted much attention because of its fascinating behaviour during cell division and its evident roles in essential processes, such as fertilisation and inheritance [29].

The nuclear compartment, responsible for enclosing the DNA, is the principal site of DNA and RNA synthesis [23] and is the largest structure in most cells, which can alter greatly depending on the particular cell cycle stage [30].

The Nuclear Envelope (NE) encloses de nuclear material and consists of two concentric membranes: the Inner Nuclear Membrane (INM) and the Outer Nuclear Membrane (ONM), which are penetrated by nuclear pore complexes (NPC). These components will be reviewed in detail in the following subsections.

1.3.1. Nuclear Envelope (NE)

The NE plays a dual role as both a protective membrane for the genome and a flexible communication interface between the nucleus and cytoplasm. It primarily consists of three components: the nuclear lamina, a double lipid bilayer, and NPCs [31]. The double membrane is made up of the INM and the ONM, separated by the perinuclear space. The ONM is continuous with the endoplasmic reticulum (ER), and the perinuclear space connects directly to the ER lumen. Despite the continuity between NE and ER, the ONM and INM contain distinct proteins absent in the ER [32]. NPCs act as gateways through the NE, allowing controlled molecule exchange between the nucleus and cytoplasm [30]. Figure 1.4 illustrates the structure and elements of the NE.

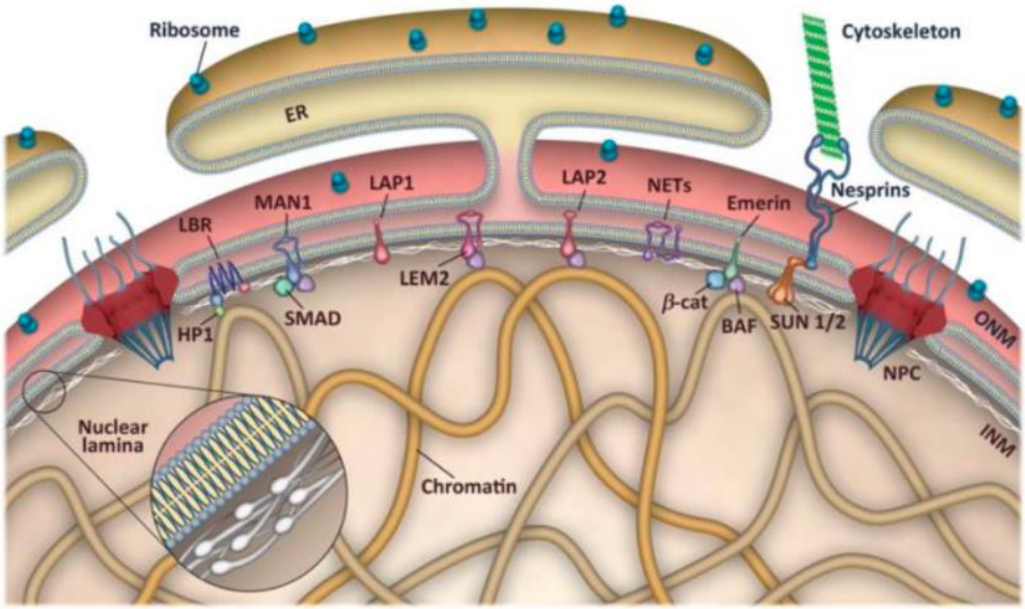

Figure 1.4 - Nuclear Envelope. NE illustration showing its main components, which include the outer (ONM) and the inner nuclear membrane (INM), connected through nuclear pore complexes (NPC). The ONM is linked to the endoplasmic reticulum (ER) and contains ribosomes, as well as proteins like nesprins, connecting the nucleus to the cytoskeleton. The INM has various nuclear envelope transmembrane (NET) proteins, with LEM domain proteins interacting with chromatin-binding protein BAF and transcription factors. Additionally, the lamin B receptor (LBR) associates with heterochromatin protein 1 (HP1) and modified histones [33].

Beyond its role in protecting genetic material and regulating gene expression, the NE is crucial for several physiological processes, including cell division [32]. During interphase, the NE expands and then fully disassembles during mitosis [34]. After cell division, the NE reassembles to form a sealed barrier that facilitates selective transport between the nucleus and cytoplasm [35]. Once reformed, the NE enlarges and undergoes further structural changes crucial for the cell cycle and transcription processes, including the creation of new NPCs [36]. This requires the NE to be adaptable, allowing it to remodel and integrate new components [32].

1.3.1.1. Outer Nuclear Membrane (ONM)

The ONM is part of the NE that interfaces with the cytoplasm. It is continuous with the ER membrane, often being studded with ribosomes, but also has distinct roles. Proteins such as nesprins are embedded in the ONM and play a key role in positioning the nucleus within the

cell. This positioning is essential for various cellular processes, such as cell polarization, pronuclear migration, and syncytia organization [37].

Nesprins and other ONM proteins are part of the Linker of Nucleoskeleton and Cytoskeleton (LINC) complexes [38]. These complexes span the perinuclear space, linking the ONM to the INM via SUN domain proteins (as depicted in Figure 1.4) [39]. This linkage maintains a consistent separation of about 50 nm between the ONM and INM, facilitating interactions between the nucleus and cytoskeleton [32].

Furthermore, the LINC complexes connect the cytoskeleton to chromatin, influencing crucial nuclear functions such as transcription, replication, and DNA repair [32, 38]. By affecting chromatin organization and gene expression, the ONM plays a vital role in maintaining nuclear structure and coordinating interactions between nuclear and cytoplasmic activities [40–42].

1.3.1.2. Inner Nuclear Membrane (INM)

The INM, adjacent to the nuclear lamina and facing the nucleoplasm, is a crucial part of the NE. It contains over 60 integral membrane proteins, known as nuclear envelope transmembrane proteins (NETs) [32]. Although many remain uncharacterized, several proteins, including lamin B receptor (LBR), lamina-associated polypeptide (LAP) 1, LAP2, emerin, and MAN1 (Figure 1.4), are known to interact with lamins and chromatin [43].

INM proteins are vital for nuclear functions, such as chromatin organization, gene expression, and DNA metabolism. Their mislocalization and dysfunction have been linked to various human diseases, driving increased interest in NE biology [44, 45]. Many INM proteins contain LEM domains, which interact with the Barrier to Autointegration Factor (BAF), a protein that binds strongly to DNA, core histones, linker histones, and nuclear lamina proteins. These interactions allow LEM domain proteins to anchor chromatin to the INM, providing structural support and contributing to regulatory functions [43].

LBR is another critical INM protein involved in chromatin anchoring. It is a transmembrane protein with an nucleoplasmic N-terminal region and eight membrane-spanning regions. LBR associates with B-type lamins and interacts with heterochromatin components, such as core histones, heterochromatin protein 1 (HP1), and MeCP1 histone deacetylase complex. These interactions aid in the organization of heterochromatin and regulate gene expression [46–48].

Overall, the INM is integral to maintaining nuclear structure and function, influencing gene expression and chromatin organization, and playing a significant role in cellular homeostasis and disease [43].

1.3.1.3. Nuclear Lamina

The nuclear lamina comprises a network of nuclear lamins, proteins positioned on the nuclear side of the INM. These lamins, a subclass of intermediate filament proteins, form a two-dimensional lattice that structurally supports the NE by connecting to NPCs and integral membrane proteins. This structure also interacts with chromatin, thereby linking DNA to the NE and influencing both nuclear architecture and function [43, 49].

In mammals, nuclear lamins are categorized into A- and B-type, originating from the *LMNA* and *LMNB* genes, respectively. A-type lamins, such as lamin A and lamin C, are produced through alternative splicing of the *LMNA* gene, whereas B-type lamins, including lamin B1 and B2, are encoded by the *LMNB1* and *LMNB2* genes [50]. Both A- and B-type lamins possess a C-terminal CaaX motif (C: cysteine, a: aliphatic amino acid, X: any amino acid) that undergoes farnesylation, facilitating hydrophobic interaction with the lipid bilayer. This interaction enhances membrane attachment in a thermodynamically favourable process [51, 52].

Structurally, lamins comprise a globular amino-terminal head, an α-helical central rod domain, and a carboxy-terminal tail. A nuclear localization signal (NLS), required for transport into the nucleus, is present in all lamins between the carboxyl-terminal of the central rod domain and the Ig-fold [49, 53–55]. Lamins A and C functional regions are depicted in Figure 1.5 as an example.

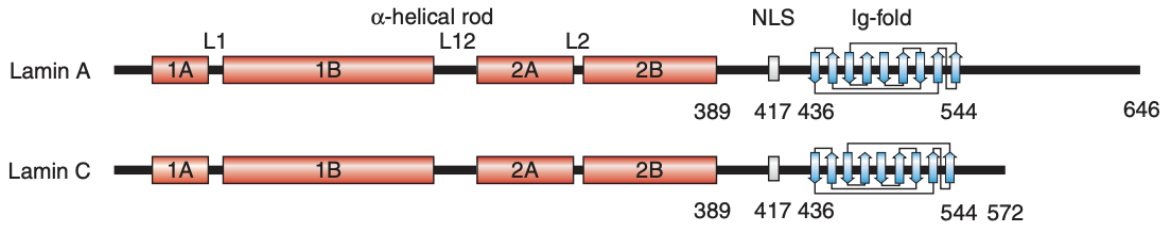

Figure 1.5 – Illustration of mature lamin A and C proteins. The architecture of these proteins includes a brief amino-terminal head domain, followed by a central α-helical rod region (red), and concludes with the carboxyl-terminal domain. This end domain hosts the Nuclear Localization Signal (NLS) and the immunoglobulin (Ig-fold), (blue) and consists of nine β-strands. Retrieved from [49].

Lamins form homodimers that assemble into higher-order structures through specific interactions, providing essential mechanical support and serving as scaffolds for chromatin and various nuclear proteins involved in cellular signalling, proliferation, and gene regulation [49].

Interestingly, lamins are considered ancestral to the superfamily of intermediate filament proteins, as evidenced by the presence of lamin-like proteins across organisms with intermediate filaments [23]. This underscores their fundamental role in nuclear structure and function. Studies using electron microscopy have further characterized the spatial organization of chromatin within the nucleus, revealing that lamin-associated domains (LADs) predominantly consist of heterochromatin, characterized by low gene density and transcriptional activity and enriched with repressive chromatin markers [55, 56]. These observations highlight the intricate relationship between lamins and the genomic architecture, emphasizing their critical role in nuclear organization and cellular functionality.

The maturation of lamins involves specific post-translational modifications, especially at the C-terminal (Figure 1.6). First, the prelamins undergo farnesylation, where a farnesyl group is added to the cysteine residue in the CaaX motif. Following farnesylation, the newly exposed carboxyl group is methylated by carboxyl methyltransferase. In the case of prelamin A, an additional step occurs. The ZMPSTE24 protease cleaves off the farnesylated and methylated C-terminal segment, yielding mature lamin A [57]. This final cleavage step does not occur in B-type lamins, which retain both their farnesyl and methyl groups [49]. Lamin C does not possess the CaaX motif and, therefore, does not undergo the farnesylation or methylation steps [43, 49].

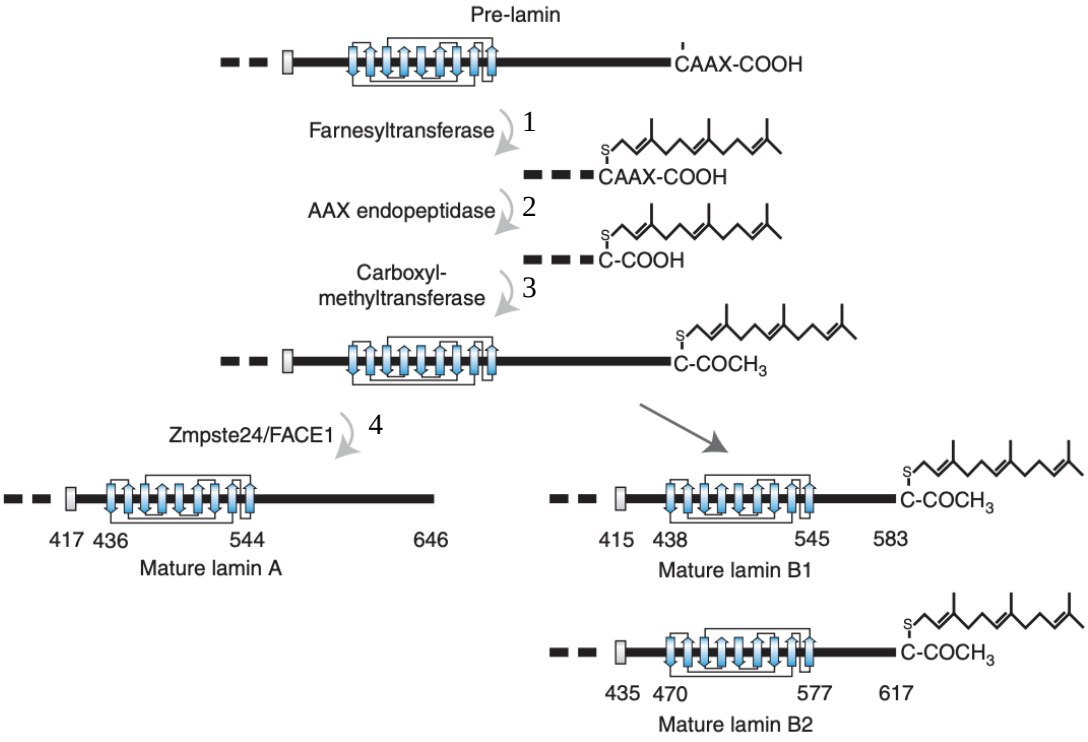

Figure 1.6 – C-terminal maturation processes of lamins A, B1 and B2. 1. Farnesylation of the cysteine within the CaaX sequence of prelamin A, B1 and B2 is facilitated by farnesyltransferase. **2.** An AAX endopeptidase enzyme removes the three terminal residues. **3.** Methylation of the now exposed carboxylic acid is performed by a carboxyl methyltransferase. **4.** Uniquely for lamin A, the metalloprotease Zmpste24/FACE1 removes the terminal 15 amino acids and the attached farnesyl group. B-type lamins do not undergo this last step and thus retain their farnesyl modifications. Adapted from [49].

Once processed, these proteins contribute to the mechanical properties of the nuclear envelope. Lamin A, with its fully mature structure, forms a thicker and more rigid meshwork that significantly enhances the mechanical rigidity of the NE due to its altered solubility. In contrast, B-type lamins form thinner layers closely linked to the INM, contributing to nuclear elasticity by remaining anchored to the membrane through their retained farnesyl group. A-type lamins are expressed in a tissue-specific and developmentally regulated manner, while the expression of B-type lamins is ubiquitous throughout tissues [33, 45, 53, 58].

1.3.1.4. Lipid composition of the nuclear membrane

Nuclear lipids are crucial for preserving essential structural characteristics of the nucleus, such as modulating the fluidity of the NE and matrix by adjusting the phosphatidylcholine/sphingomyelin/cholesterol (PC/SM/Chol) ratio and serving as anchor

points for chromatin [59]. Notably, phosphatidylserine (PS) assists in the reassembly of the nuclear envelope following cell division [60]. Furthermore, nuclear lipids regulate DNA replication, transcription, and gene expression and serve as platforms for signal transduction pathways associated with hormones and vitamins [61]. The nucleus contains specific enzymes necessary for autonomous lipid metabolism, including those involved in the metabolism of sphingolipids like sphingosine kinase, sphingomyelinase, and sphingomyelin synthase [59, 61, 62].

Research on the mammalian nuclear lipidome is sparse, with limited studies addressing these specific lipid pools, potentially due to challenges associated with nuclear isolation and purification needed for detailed lipid profiling [63]. Despite these challenges, certain aspects of the mammalian nuclear lipidome have been consistently observed, such as the dominance of glycerophospholipids in nuclear membranes. PC accounts for 30-50% of all nuclear lipids, with phosphatidylethanolamine (PE) comprising around 20%. Other notable glycerophospholipids include phosphatidylinositol, various phosphoinositides (such as phosphatidylinositol 4,5-biphosphate, $PI(4,5)P_2$), and PS [63]. The most abundant sphingolipid is SM, followed by ceramide, a-series gangliosides, and other minor sphingolipids [63]. The nuclear lipidome also comprises Chol and its derivatives, dolichol, and ether lipids [59]. Notably, triglycerides (TG) are more prevalent in the nuclear compartment than other organelles, possibly linked to recent discoveries of lipid metabolism in the INM and the formation of nuclear lipid droplets [64, 65]. The comprehensive characterization of the mammalian nuclear lipidome remains incomplete, with significant uncharted variations among nuclear lipid pools.

1.3.1.5. Role of lipids

Historically recognised for their roles in cellular structure and energy storage, the diverse functional, regulatory, and signalling roles of lipids in health and disease have become increasingly apparent over the last few decades [66].

The lipid composition of cellular membranes plays a crucial role in various cellular functions and the proper performance of organelles by influencing the membrane's biophysical properties, such as lateral organization, fluidity, and flexibility. These properties are essential for the recruitment and interaction of membrane proteins, thereby supporting proper membrane function. [63]. Additionally, they play an essential role in the propagation of signals and in membrane-related events, such as fusion and fission, which are necessary for organelle

development [67–69]. Membrane properties, such as curvature, head group size, and sterol content, influence lipid packing and can create packing defects that expose hydrophobic regions. These defects are recognized by proteins that interact with the membrane, contributing to cellular signalling and membrane-related functions [69]. Furthermore, the amount of sterols in a membrane affects its packing, overall order, and the creation of raft-like domains essential for the assembly of signalling protein complexes [70]. Lipids also play specialised roles in signalling, acting as triggers for enzymatic activities and securing proteins to specific subcellular sites. Some lipids are transformed into bioactive signalling molecules that influence extracellular communication [71, 72]. Moreover, alterations in lipid properties, such as through oxidation, can compromise membrane and organelle functions, eliciting cellular responses that help maintain the integrity of the cell [63].

1.3.2. How ageing impacts the nucleus, its lipids and NE proteins

As organisms age, there is a noticeable decline in nuclear function, accompanied by progressive deterioration of nuclear morphology. This functional decline is often accompanied by disruptions in NE protein functions and alterations in lipid composition, contributing to cellular dysfunction and the onset of age-related diseases. Emerging research underscores the crucial role of systemic lipid profiles as indicators of metabolic disorders and highlights the influence of lipids on the ageing process [66].

Lipids, particularly fatty acids (FAs), are essential components that determine cellular health and longevity. Fatty acids can be categorized as saturated (SFA), monounsaturated (MUFA), or polyunsaturated (PUFA). In eukaryotic cells, the ratio of saturated to unsaturated FAs typically stands at 40/60, affecting membrane fluidity, flexibility, and selective permeability and influencing the membrane's susceptibility to peroxidation [73]. Reactive oxygen species (ROS), natural byproducts of aerobic metabolism, accumulate with age and promote lipid peroxidation, damaging membranes and other biological macromolecules [63]. Membrane phospholipids, especially PUFAs, are particularly vulnerable to ROS, and longer-lived species often exhibit a lower PUFA/MUFA ratio in their membranes compared to shorter-lived ones [73].

Plasmalogens, a specific class of glycerophospholipids, are known for their role as sacrificial antioxidants. Rather than completely preventing lipid peroxidation, they are preferentially oxidized to protect other lipids from oxidative damage. This sacrificial oxidation helps reduce the overall oxidative stress in cells [74]. As organisms age, the decline in

plasmalogen levels makes cellular membranes more susceptible to lipid peroxidation, contributing to the ageing process and age-related diseases. Advances in lipidomics have revealed changes in plasmalogen levels in fibroblasts under various pathological conditions, including amyotrophic lateral sclerosis (ALS), further emphasising their importance in protecting cellular integrity as oxidative stress increases with age [75].

Additionally, recent findings have pointed to the harmful effects of age-related excessive cytosolic lipid droplet accumulation in both adipose and non-adipose tissues, though the impact of nuclear lipid droplets on cellular function and tissue homeostasis remains less understood [76].

Recent longitudinal multi-omics studies have shown that approximately 40% of age-correlated dysregulated molecules are lipids, supporting the concept of a 'LipidClock' to predict biological ageing [77]. The LipidClock model tracks changes in lipid composition over time, using specific patterns of lipid dysregulation as biomarkers to estimate an individual's biological age, which may differ from their chronological age [78]. Furthermore, current research discusses the modulation of ageing hallmarks such as cellular senescence, chronic inflammation, gut dysbiosis, telomere attrition, genome instability, proteostasis, autophagy, epigenetic changes, and stem cell dysfunction, focusing on intrinsic age-dependent deficiencies in lipid metabolism and external lipid alterations [66]. Additional details on how ageing influences lipid composition and how these changes correlate with each of the mentioned hallmarks of ageing can be found elsewhere [66].

In ageing tissues, cells often display nuclei with abnormal shapes, a phenomenon observed not only in human cells from aged tissues but also in model organisms and progeroid models [79]. This abnormality primarily results from compromised laminar integrity, as evidenced in several studies [80–82]. Such disruptions include reductions in concentration, mutations, or abnormal processing of laminar proteins, leading to nuclei with irregular shapes that consequently affect chromosome organization and gene expression profiles [79].

Nuclear blebs, which are protruding structures found in regions of sparse underlying lamin fibres and thus less dense lamina meshwork, are common in senescent cells [83]. These blebs alter the overall 3D shape of the nuclei, giving them a lobulated appearance, associated with aged, progeroid, and cancerous cells [84].

Further emphasizing the role of the NE in ageing, mutations in the *LMNA* gene cause premature ageing disorders such as HGPS, a rare condition in which affected individuals have an average lifespan of 14 years. They present symptoms such as subcutaneous fat loss, alopecia, and progressive heart failure (Figure 1.7A). This highlights the potential role of the nuclear

lamina and associated proteins as major regulators of the normal ageing process. Progeroid syndromes, representing severe premature ageing conditions, provide powerful models for studying potential mechanisms underlying physiological ageing [50]. In the case of HGPS, a deletion of 50 amino acid residues region that includes the sequence recognized by ZMPSTE24 occurs. Consequently, an abnormal form of lamin A, known as progerin, accumulates within the nucleus. Progerin remains permanently farnesylated, and this farnesyl group is hydrophobic, promoting its strong association with the INM. This persistent hydrophobic interaction causes progerin to aberrantly anchor to the membrane, disrupting normal lamin organization and contributing to the structural defects observed in the NE (Figure 1.7B) [85].

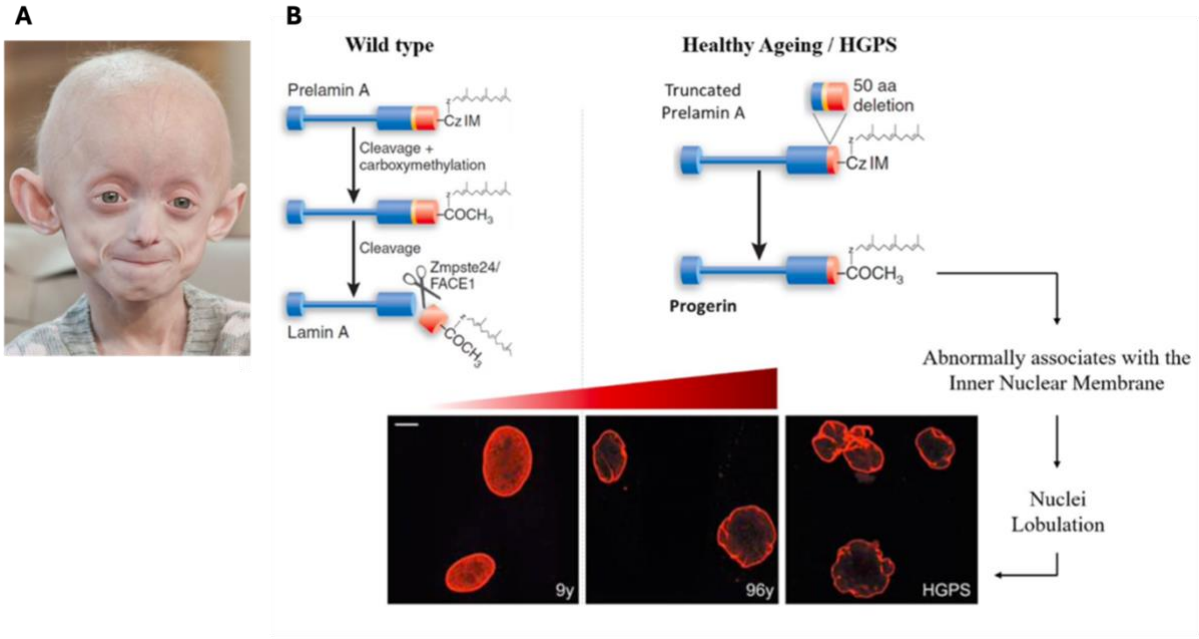

Figure 1.7 - Hutchinson-Gilford Progeria Syndrome characteristics and proteolytic processing of preLA. **A.** Children diagnosed with HGPS. HGPS is characterised by symptoms typical of premature ageing, including subcutaneous fat loss, alopecia, osteoporosis, joint stiffness, and progressive heart failure, among others [85]. **B.** Proteolytic processing of preLA in both wild-type (WT) and HGPS. Immunostaining images probed with anti-lamin A/C depicted human fibroblasts at different ages and HGPS. Adapted from [80, 86].

Remarkably, comparable alterations were noted in fibroblasts from healthy elderly individuals. These changes include an increase in preLA and progerin levels and the sequestration of LA in the periphery, leading to an imbalance in nucleoplasm-periphery LA distribution (Figure 1.7B) [80, 87]. The accumulation of these proteins in the membrane results in the development of NE invaginations, disturbing the nuclear basket within the NPC, compromising nuclear transport, and contributing to increased genome instability [88]. Moreover, lamina defects disrupt the SUN-nesprin bridges, impairing not only the stability of the genome, but also all the processes dependent on the cytoskeleton, such as mitosis, cell

adhesion, migration, proliferation, differentiation, and survival. Interestingly, progerin expression also impacts the synthesis of a healthy extracellular matrix, which is crucial for all processes mentioned. [89, 90]. Figure 1.8 summarizes some of these characteristics.

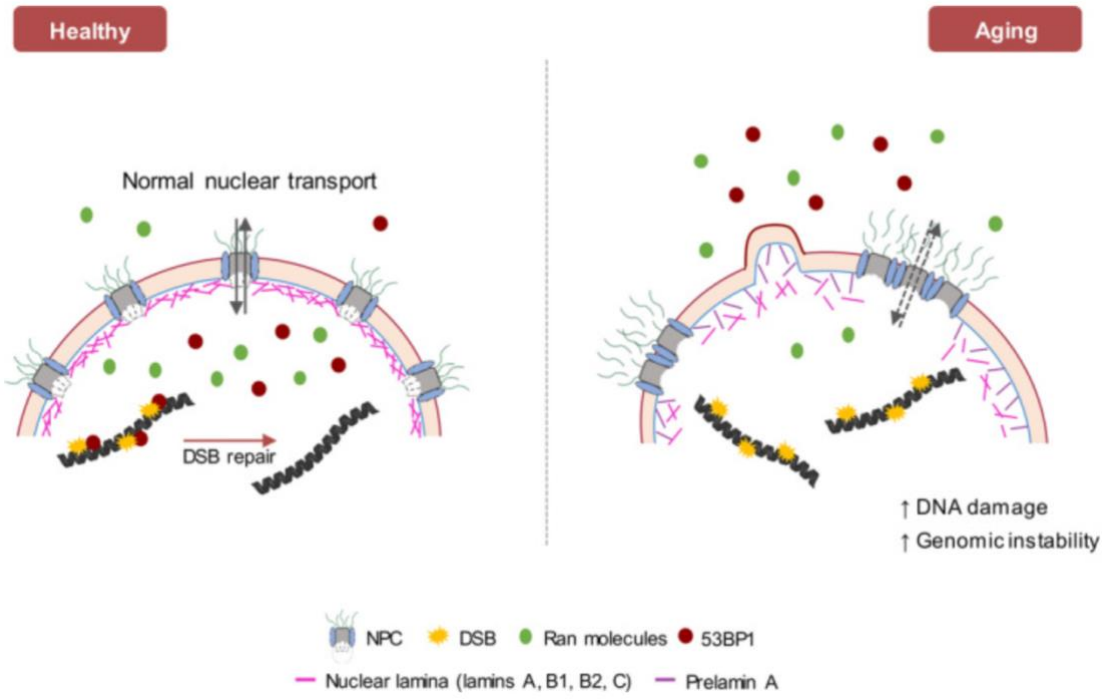

Figure 1.8 – Molecular-level comparison between a healthy and an aged nucleus. As people age, there is an increase in the accumulation of the protein preLA, which leads to deformations in the NE. These deformations capture the protein Nup153, thereby disrupting the structure of the nuclear basket within the NPC. This disruption leads to the clustering and degradation of NPCs, reducing the NE's ability to selectively permit molecular passage. The misplacement of Nup153 interferes with the Ran gradient, crucial for transporting molecules into the nucleus, notably affecting the nuclear import of the molecule 53BP1. 53BP1 plays a vital role in repairing DNA double-stranded breaks, and its impaired importation hinders DNA damage repair mechanisms, causing an increased prevalence of DNA damage in cells [91].

Studying cellular membrane ageing in natural models poses several challenges, including the complexity of *in vivo* systems, where multiple overlapping factors influence cellular processes, and the difficulty in isolating the specific contribution of membrane lipids. Additionally, natural models often show variability in lipid composition between tissues and individuals, making it hard to obtain consistent data. As a result, researchers increasingly turn to *in vitro* models, though their use is still in development and not yet fully standardised. Synthetic biology facilitates the creation of controlled systems, allowing for more detailed

investigations into how membrane lipids and their interactions with other molecules change with age. While these models provide valuable insights into lipid behaviour and composition changes within cellular structures, they are still evolving and require further refinement to fully replicate the complexity of natural ageing processes. Nevertheless, this approach offers potential for targeted research into lipid-driven ageing mechanisms and could foster the development of therapies to maintain or restore lipid function in ageing cells.

1.4. Emergence of Synthetic biology in the ageing puzzle

Synthetic biology is a field dedicated to the design and development of new metabolic and regulatory pathways, along with circuits and networks, that can be tightly regulated and controlled [92]. It facilitates the development of novel enzymes, pathways, and comprehensive cellular systems. This field opens up innovative avenues for disease treatment by engineering cells or bacterial communities for therapeutic and diagnostic uses [92]. Additionally, synthetic biology plays a role in biosensing and maintaining cellular balance, which can influence disease progression [93]. The significance of understanding cellular architecture, such as membrane biology, is paramount in these applications.

Despite extensive research over the past decades, the detailed structural organisation and molecular interactions within membranes remain partially understood. Membranes are intricate, tightly controlled systems whose functions rely on the variable and dynamic nature of the lipid bilayer structure [94]. The bilayer's dimensions, spanning nanometres in thickness and micrometres in length, have spurred considerable interest in the physics of its self-assembly, stability, and self-repair capabilities [95].

Artificial lipid membranes have been developed and studied since the early 1960s, providing insights into physiological processes [96]. They are crucial for studying changes in lipid composition through ageing, which impacts membrane fluidity and functionality [97]. Such changes are vital for understanding cellular signalling, nutrient transport, and overall cellular health, which are linked to ageing and related diseases [98]. Moreover, the advancement in artificial lipid membranes has led to their use in drug testing and biosensor development, showcasing their broad applicability in scientific and technological domains [99].

1.4.1. *In vitro* models for membrane studies

Exploring the challenges and questions related to membranes through *in vitro* models provides a structured approach for researchers to examine the complex roles and characteristics of cellular membranes in a controlled setting. Below are some principal models and their practical uses:

- *Lipid Bilayer Models (Artificial Membranes):*
    - Black Lipid Membranes: Formed by applying a lipid solution across a tiny aperture in a partition separating two aqueous spaces, this model is highly effective for exploring the activity of ion channels and the movement of various molecules across membranes [100].
    - Liposomes: Vesicles composed of lipid bilayers that can contain various substances, useful for research into how drugs are delivered, how membranes merge, and how substances are transported. Additionally, they are often used to gather information about the biophysical characteristics of membranes with various lipid compositions. Made in different sizes, they can be classified as small unilamellar vesicles (SUVs) (<100 nm), large unilamellar vesicles (LUVs) (100-1000 nm), and giant unilamellar vesicles (GUVs) (>1000 nm). When multilamellar, liposomes are referred to as multilamellar vesicles (MLVs) [101].
    - Supported Lipid Bilayers (SLBs): Lipid membranes are formed onto a solid support, making them ideal for studying how membrane proteins interact with each other and the movement of components within the membrane [101].
- *Cell-Derived Membranes:*
    - Giant Plasma Membrane Vesicles (GPMVs): These vesicles are derived from cellular membranes and preserve many properties of the plasma membrane, including the composition and functionality of proteins. They are utilised to observe changes in membrane organization and to study signalling pathways, among others [102].
- *Hybrid Systems:*
    - Proteoliposomes: These vesicles integrate specific proteins within a lipid bilayer, enabling detailed studies of protein functions within a regulated lipid

environment, critical for understanding the workings of membrane proteins like transporters and receptors [103].

- Biomimetic Systems: These systems combine synthetic and biological elements to form functional equivalents of cellular membranes, aiding in the study of complex interactions and pathways that are challenging to fully replicate with synthetic models alone [104].

These models are instrumental in dissecting the multifaceted functions of membranes within cells, offering insights into their interaction with pharmaceuticals, how their composition and organisation affect cellular behaviour, and in devising therapeutic strategies targeting membrane dynamics and other properties.

1.4.2. What is being done with *in vitro* models and their advantages

In vitro models of cellular membranes, such as lipid bilayers, liposomes, and proteoliposomes, represent pivotal tools in contemporary biomedical research, particularly in elucidating drug delivery mechanisms, studying ion channel function, and understanding protein-membrane interactions [96]. These models simulate the cellular environment under controlled conditions, enabling a deeper understanding of biological processes at the molecular level.

With the emergence of synthetic cell development, researchers are now exploring the possibility of creating *in vitro* organelles. In the context of this thesis, liposomes and other lipid bilayer models serve as critical tools for studying the properties of nuclear membranes in a controlled environment. These models represent a foundational step toward the long-term vision of developing a synthetic nucleus. These systems allow researchers to isolate the effects of lipids, helping to uncover how lipid composition, membrane tension, and flexibility influence nuclear function. Liposomes, for example, provide valuable insights into how lipids contribute to membrane organization and behavior, making them essential for advancing our understanding of nuclear membrane mechanics. Additionally, they are widely recognised for their role in enhancing the delivery and efficacy of pharmaceutical agents. Research by Allen and Cullis highlights the capacity of liposomal formulations to alter the distribution and toxicity profiles of drugs, particularly anticancer agents [105]. By encapsulating drugs within liposomes, researchers can improve solubility, stability, and targeted delivery, reducing adverse effects on non-target tissues [105]. This technique underscores the utility of liposomes

in optimising therapeutic outcomes and underscores their significance in drug delivery research.

Further extending the utility of *in vitro* models, black lipid bilayers provide an essential platform for studying ion channels. Work by Coronado, Latorre, and Vergara demonstrates how these bilayers facilitate the examination of ion transport mechanisms critical to neurological function [106]. The ability to measure ion flux in a controlled setting allows for a precise understanding of ion channel behaviour, including gating mechanisms and selectivity. This insight is crucial for developing treatments for disorders affected by ion channel functionality, such as epilepsy and cystic fibrosis [106].

Supported lipid bilayers, as discussed by Karlsson *et al*. offer another layer of analytical depth by enabling the study of protein dynamics within membranes [107]. These bilayers allow for the spatial organization of proteins and provide insights into their interactions and mobility [108]. Understanding these interactions is fundamental to deciphering cellular signalling pathways and trafficking processes, which are integral to the normal functioning and pathology of cells [108].

Collectively, these *in vitro* models serve as indispensable tools in biomedical research, offering insights for understanding fundamental biological processes and advancing therapeutic innovations. By mimicking the complex environment of cellular membranes under experimentally controlled conditions, these models provide a reproducible and ethically sound platform that enhances the precision of biomedical investigations, thereby paving the way for significant advances in both the understanding and treatment of human diseases.

1.5. Introduction to the Theme of the project

Understanding the fundamental mechanisms of ageing presents multiple challenges, including the task of linking physiological phenotypes with their primary molecular actors at the nanoscale.

Researchers studying cell senescence, as well as physiological and accelerated aging, have noted that many mechanisms recognized as contributors to progeroid disorders also play a role in natural aging. Disturbances in the nuclear lamina, for example, lead to abnormal nuclear architecture, which affects critical functions such as genomic stability and DNA repair (see section 1.3.2), ultimately impacting overall cell functioning.

In parallel, the lipid composition of the NE also appears to undergo significant changes with age. While the age-specific lipidome of the NE remains largely unexplored, preliminary lipidomics data from the host lab suggest substantial alterations in the NE lipid profile during

aging. Notably, a decrease in specific ether lipids has been observed in primary cells from older individuals, further underscoring the role of lipid metabolism in NE integrity during the aging process (Figure 1.9).

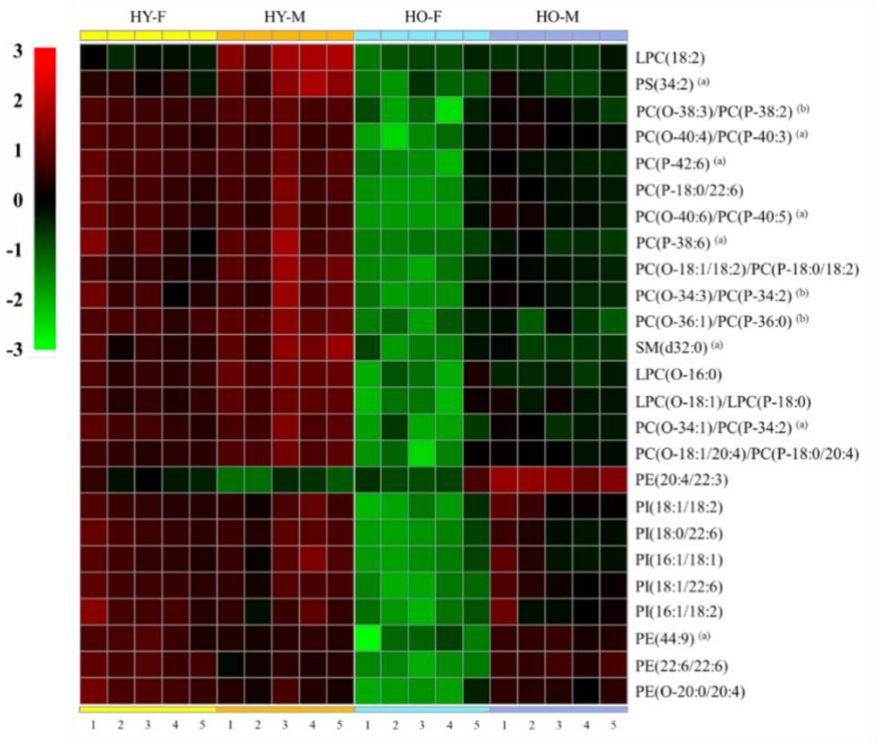

Figure 1.9 – Heatmap chart representing the TOP25 polar lipid species contributing to the variations observed in the healthy young-female (HY-F), healthy young-male (HY-M), healthy old-female (HO-F), and healthy old-male (HO-M) groups. The heatmap visually represents changes in lipid concentrations on a colour scale, where the numbers represent the fold increase in the concentration compared with the mean value. (a) The fatty acid (FA) profiles of these lipids were not distinguished using hydrophilic interaction liquid chromatography tandem mass spectrometry analysis; (b) The isomers O- and P- allow for multiple FA chain configurations within the same lipid type. For example, in the lipid species PC(O-38:3)/(P-38:2), the identified variants include PC(O-18:0/20:3), PC(P-20:1/18:1), PC(P-18:1/20:1), and PC(O-18:1/20:2).

Ether lipids are characterised by the replacement of the ester-bound acyl chain at the *sn*-1 position with an alkyl or alkenyl group via ether or vinyl-ether bonds, respectively [109]. Although biophysical studies on these molecules are sparse, and conclusions may vary depending on the specific lipid species, it seems evident that ether-linked lipids can significantly influence the biophysical properties of biomembranes [110–112].

Taking this into account, it is yet to be studied how lamins and lipid changes can influence quantitatively the biomechanical and biophysical characteristics of the nuclei during ageing. Furthermore, it is still unclear if age-related changes in the NE lipids have consequences similar to those linked to the presence of mutant forms of lamin A (see section 1.3.2 and Figure 1.7),

in terms of nuclear dynamics and overall nuclear function. In other words, the impact that variations in NE lipids might have on lipid-lamin interaction and the subsequent organisation of the nuclear lamina remains to be explored.

All this leads us to wonder "How the NE grows old"? We attempt to explore its biomechanical and biophysical characteristics during ageing, gathering more information on how this physiological process impacts these properties by examining the nuclear membrane and the behaviour of Lamin A.

However, traditional studies using live cells often encounter significant challenges due to the intricate and dynamic nature of cellular systems. As we deepen our understanding of the ageing process at the nuclear level, the evolving field of synthetic biology holds remarkable potential for further exploration. The scientific community is increasingly shifting towards a new research paradigm, where the development of *in vitro* organelle models, such as synthetic nuclei, is gaining prominence. Through the lens of synthetic biology, we can construct and analyse the nuclear membrane features in controlled environments, offering insights into the fundamental mechanisms that drive nuclear ageing. This approach not only paves the way for a deeper understanding of ageing but also sets the stage for future breakthroughs in this field, underscoring the transformative impact of synthetic biology in modern science.

1.6. Main Goals and Strategy

This project aims to investigate the biomechanical and biophysical characteristics of the nucleus during human ageing by focusing on key aspects such as membrane elasticity and order, as well as LA organization. Membrane order, as defined by lipid packing, is a fundamental property that significantly influences membrane protein function, lipid-protein signalling platforms, and membrane recycling [113]. Membrane elasticity plays a critical role in maintaining cellular integrity, allowing cells to adapt to deformations like stretching without damage [114]. Membrane tension, on the other hand, affects cellular morphology and mechanotransduction, impacting signalling cascades that respond to mechanical stimuli [115]. Nuclear ageing might be associated with alterations in these membrane properties, contributing to cellular dysfunction and increased susceptibility to stress, highlighting the crucial role of NE dynamics in ageing and cellular adaptation.

The second aim of this project is trying to develop *in vitro* models that mimic these characteristics of the nuclei, relying on a bottom-up strategy and using LUVs as a starting point.

To achieve these goals, primary human fibroblasts of healthy young and healthy aged donors (both male and female), as well a patient with HGPS, were cultured (see Section 3.1).

A detergent-free protocol for the isolation of nuclei based on nuclei sorting was then developed to assure high nuclei purity. Imaging flow cytometry, confocal microscopy, atomic force microscopy (AFM), and transmission electron microscopy (TEM) were employed to ensure precise isolation of nuclei from cellular debris. Following the optimisation of nuclei isolation, a multifaceted approach was used to characterise the isolated nuclei from donors of varying ages and the HGPS patient. AFM-based Force Spectroscopy (AFM-FS) was utilised to assess the biomechanical properties of the nuclei, specifically measuring their stiffness and elasticity. The biophysical features of the NE were examined using multiphoton microscopy following the incorporation of the Flipper-TR probe to provide insights into membrane tension, and confocal microscopy after introducing di-4-ANEPPDHQ to evaluate membrane order. The localisation of lamin A in the nucleoplasm and its association with the NE was also confirmed by confocal microscopy.

Lipids extracted from the nuclei of an aged donor were then used to form LUVs. Laurdan general polarization (GP) values were obtained to compare the membrane order of LUVs derived from extracted lipids from an old donor with those of controls (1-palmitoyl-2-oleoyl-glycero-3-phosphocholine (POPC) and 1,2-dipalmitoyl-sn-glycero-3-phosphocholine (DPPC) only).

In conclusion, the primary objective of this project is to investigate the biomechanical and biophysical properties of the nucleus during ageing, while also developing *in vitro* models, such as LUVs, to assess whether they replicate the characteristics observed in real nuclei. These models are intended to provide a platform for further research into nuclear membrane dynamics in a controlled environment, enabling further research into the fundamental properties of the NE.

2. PRINCIPAL METHODOLOGIES & EXPERIMENTAL APPROACHES

This section outlines the fundamental principles of this study's methodologies and experimental techniques.

2.1. Culture and usage of primary cells

Primary cells are cells taken directly from living tissues, such as a biopsy, and grown under controlled conditions in the lab. These cells closely mimic the natural characteristics and functions of the tissue from which they are derived because they have not been extensively multiplied. This makes them particularly valuable for research that aims to understand biological processes, disease mechanisms, and for testing new drugs [116]. Although these cells have a limited lifespan and cease to divide due to senescence, which poses challenges in their culture and maintenance, they are invaluable in research. By closely mimicking *in vivo* conditions, primary cells allow for the generation of data that is more predictive of real biological outcomes. This increases the efficiency of translating basic research into preclinical and clinical applications by reducing the need for extensive *in vivo* validation [117]. Table 2.1 summarises the advantages and disadvantages of working with primary human cells.

Successful cell culture depends heavily on maintaining precise conditions tailored to the specific requirements of the cell type being cultured. The culture media should be supplemented with specific growth factors and cytokines, and cells should be maintained at optimal temperatures, typically 37 °C with 5% CO_2, tailored to each cell type. Variations in pH, glucose, and nutrient content are adjusted based on the needs of different cells. Antibiotics are initially used to prevent contamination but should be used sparingly to avoid harming the cells. Maintaining these conditions, alongside skilled handling and aseptic techniques, is crucial for the viability and longevity of the cultures [118].

To achieve the objectives of this project and study the NE throughout human ageing, human skin fibroblasts were utilised from young donors (under 5 years old), older donors (over 55 years old), and a patient with HGPS who was 8 years old. All details regarding the cell culture conditions can be found in Section 3.1.

Table 2.1 – Advantages and disadvantages of studies with primary cell lines. Adapted from [118].

Advantages	Disadvantages
• Circumvents ethical concerns related to animal testing. • Yields more relevant results than immortalized cell lines. • Mimics *in vivo* signalling when pre-screened. • Reduces reliance on animal models, potentially cost-effective.	• Slow growth, limited capacity, and eventual senescence. • Variable responses to cytokines; pre-screening required. • Certain *in vivo* metabolic mechanisms absent in culture. • High costs for isolation and culture; characteristics change with passage.

2.2. Nuclei Isolation

This study aims to investigate the biomechanical and biophysical properties of the nuclear membrane during human ageing. The approach requires two main steps: isolating the nuclei from cells and ensuring that this isolation is conducted without the use of detergents to avoid altering the lipid composition of the NE. Therefore, it was necessary to develop a detergent-free method for nuclei isolation that meets these conditions and improves upon those found in the literature [119, 120]. This was achieved by lysing the cells and recovering the nuclei through a process known as nuclei sorting.

2.3. Flow cytometry

Within the scope of this project, flow cytometry was utilised as a powerful tool for the separation of nuclei from the lysate, effectively preserving their biological functions and original characteristics with minimal damage, primarily through the use of cell sorters. Additionally, it proved indispensable for validating the nuclei isolation protocol and refining procedural details. The specific flow cytometers capability for precise counting was crucial in determining the stages of the protocol at which nuclei were being lost. This detailed data facilitated targeted adjustments to the equipment settings, leading to specific modifications that significantly increased the number of nuclei recovered post-sorting. The capabilities of flow

cytometry were also extended through the implementation of cutting-edge protocols, enabling the detection of liposomes at the nanoscale.

2.3.1. Flow cytometry principles

In every cytometer, the particles or cells for analysis must be suspended and pressurized into a focused stream of fluid. To align the particles in a single, orderly sequence for precise analysis, the sample is introduced as a core stream into a broader sheath fluid that flows around it (Figure 2.1) [121]. Within this arrangement, under laminar flow conditions, the sample is hydrodynamically focused. Both streams are pressurised by air or another gas, with the differential pressure between them controlling the rate of sample injection. Particles are then channelled through a narrow nozzle (typically 70 μm wide) to create a thin jet of fluid (Figure 2.1) [121]. This jet crosses one or more orthogonally placed laser beams to illuminate only one particle at a time. If the particle bears a fluorescent marker that is excited by a laser, it will emit light of a specific wavelength. An array of photodetectors and optical filters collects these signals, which are then processed by advanced electronics and recorded on a computer. With consistent laser intensity, the brightness of the emitted light depends on the fluorophore concentration, rendering flow cytometry a tool for both qualitative and quantitative analysis. By employing multiple lasers at different wavelengths, the analysis can excite more fluorophores, enhancing the detection capabilities [121].

As cells flow, they also scatter the incident laser light. Fluorescent emissions always appear at a longer wavelength (lower energy) than laser light, whereas scattered light maintains the incident wavelength. Forward-scattered light indicates particle size and orthogonal-scattered light provides insights into cellular complexity [121]. This scattering data alone can reveal significant details about cell structure. The collected data on fluorescence and scattering are usually visualised through histograms or scatter plots using specialised software [121].

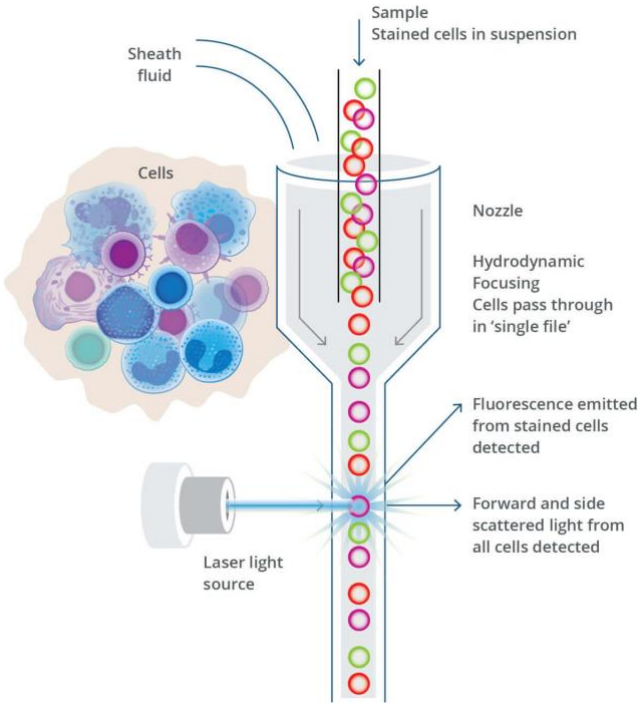

Figure 2.1 – Flow Cytometry process. This image depicts the working principle of flow cytometry, a technique used for analyzing the physical and chemical properties of cells or particles in suspension. The sample, consisting of stained cells in suspension, is introduced into the system and hydrodynamically focused into a single stream by sheath fluid, ensuring individual cells pass through the nozzle one at a time. As cells flow past a laser light source, both fluorescence emitted by stained cells and scattered light are detected. Forward-scattered light (FSC) provides information on cell size, while side-scattered light (SSC) gives insights into the cell's internal complexity. Fluorescence detection identifies the presence of specific markers on the stained cells. Created in BioRender.com.

Additionally, by setting specific thresholds, known as "gates," users can identify the percentage of cells exhibiting particular traits or combinations of characteristics (such as protein or gene expression). Depending on the cytometer used, operators can then isolate highly pure cell populations from a mixed sample [121].

2.3.2. Principles of cell sorting

Cell sorters, unlike pure analysers, offer the unique advantage of being able to identify and separate specific particles of interest from the main fluid stream into a collection container. This separation process is facilitated by inducing a gentle vibration on the nozzle, creating small ripples on the jet's surface as it exits the nozzle [121]. These ripples cause the stream to break into uniform droplets. When a particle meets predefined criteria based on its fluorescence and light scattering characteristics, it is encapsulated in a droplet that receives an electric charge. Charged droplets are then diverted by an electric field into a collection vessel, while negative droplets continue on and are discarded (Figure 2.2) [121]. The strength and polarity

of the charge influence how far droplets are deflected, allowing for the simultaneous separation of different cell populations based on varying charges [121].

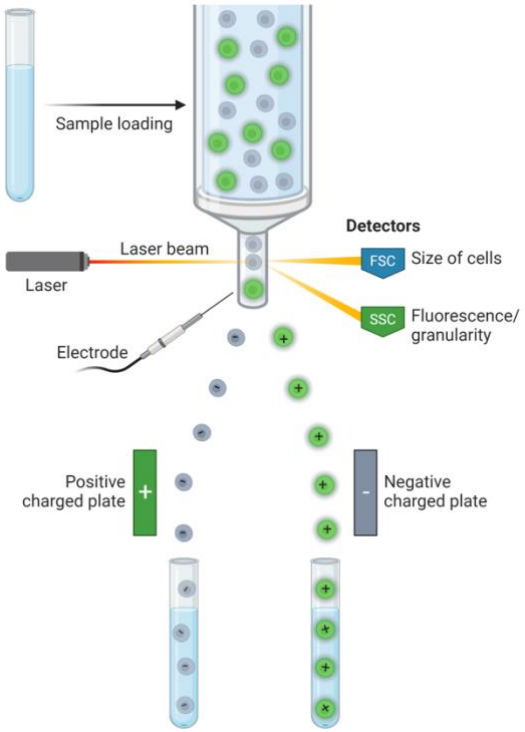

Figure 2.2 - Flow cytometry cell sorting. Cells in suspension are directed through a nozzle where they are intercepted by a laser beam. Detectors capture forward scatter (FSC) to assess cell size and side scatter (SSC) to measure fluorescence or granularity. Based on these properties, an electrode assigns a charge to the cells. Charged cells are then deflected by positive and negative plates into different collection tubes, enabling separation based on their characteristics. Created in BioRender.com.

2.3.3. Spectral flow cytometry

Flow cytometry is a widely used technology known for its ability to measure multiple parameters and handle high-throughput analysis, making it ideal for studying small particles. There is significant interest in using flow cytometry to analyse small entities like bacteria, extracellular vesicles, and viruses [122]. However, many existing flow cytometers struggle to detect biological particles smaller than 600 nm, with only a few able to identify those with a 300 nm size or smaller. This limitation has caused a research bias toward larger particles. Although no current flow cytometers can fully detect all submicron biological particles, the company Cytek has introduced an Enhanced Small Particle (ESP) detection option for their cytometer *Aurora* and *Northern Lights* models [122]. With this innovation, Cytek's Full Spectrum Profiling™ (FSP™) analysers can now examine particles as small as 70 nm without

labelling, allowing researchers to analyse the full range of autofluorescence and scattering properties of these tiny particles. Cytek's ESP Detection Option is propelling forward research in fields such as virology, studies with small bacteria, and nanoparticle research, particularly for therapeutic and biomedical applications [122].

2.4. Confocal microscopy

Fluorescence is characterized as the emission of light by a fluorophore after it absorbs light [123]. This sequence of events from excitation to emission is detailed in the Jabłoński diagram (Figure 2.3), which shows that a fluorophore absorbs a photon and transitions from its singlet ground state (S0) to an elevated excited state (S1 or S2), each populated with multiple vibrational energy levels that facilitate the vibrational relaxation of excited electrons within the same electronic state[123]. Fluorescence occurs during the transition from the zero vibrational state of the S1 back to one of the vibrational states of S0 [123]. Typically, the light emitted has a longer wavelength and consequently lower energy than the light initially absorbed.

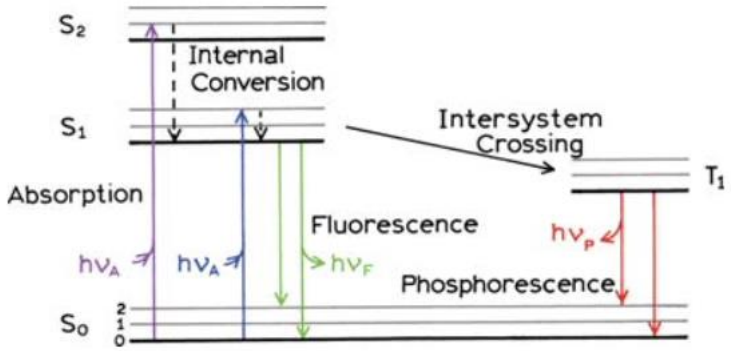

Figure 2.3 - Jabłoński diagram. Jabłoński diagram illustrating the processes of absorption, fluorescence, and phosphorescence in molecular systems. Upon absorbing a photon (hvA), a molecule is excited from the ground state (S_0) to a higher singlet excited state (S_1 or S_2). Internal conversion occurs between excited singlet states (S_2 to S_1), followed by relaxation to the ground state via fluorescence emission (hvF). Alternatively, intersystem crossing can occur, transferring the molecule to a triplet state (T_1), from which it relaxes via phosphorescence (hvP). This diagram represents the energy transitions and mechanisms involved in radiative and non-radiative decay processes [124].

Similar to a widefield microscope, the confocal microscope utilizes fluorescence optics but with enhanced imaging capabilities. It is distinguished by its ability to produce a point source of light and reject out-of-focus light, thus enabling deep tissue imaging with high resolution and optical sectioning for 3D reconstructions of samples [125]. The key to this enhanced performance lies in the pinhole (Figure 2.4), which blocks out-of-focus signals,

allowing only fluorescence from the illuminated spot to reach the detector, greatly improving image clarity and resolution [126].

The confocal microscope is equipped with a laser for excitation, filters for wavelength selection, fast-scanning mirrors, a pinhole, objective lenses, and a detector. Images are created by scanning a focused beam across a designated area, controlled by two high-speed oscillating mirrors powered by galvanometer motors. These mirrors direct the beam across the lateral X and Y axes (Figure 2.4). Three-dimensional objects are visualized by scanning multiple optical planes and compiling them using suitable microscopy deconvolution software for z-stacking [126].

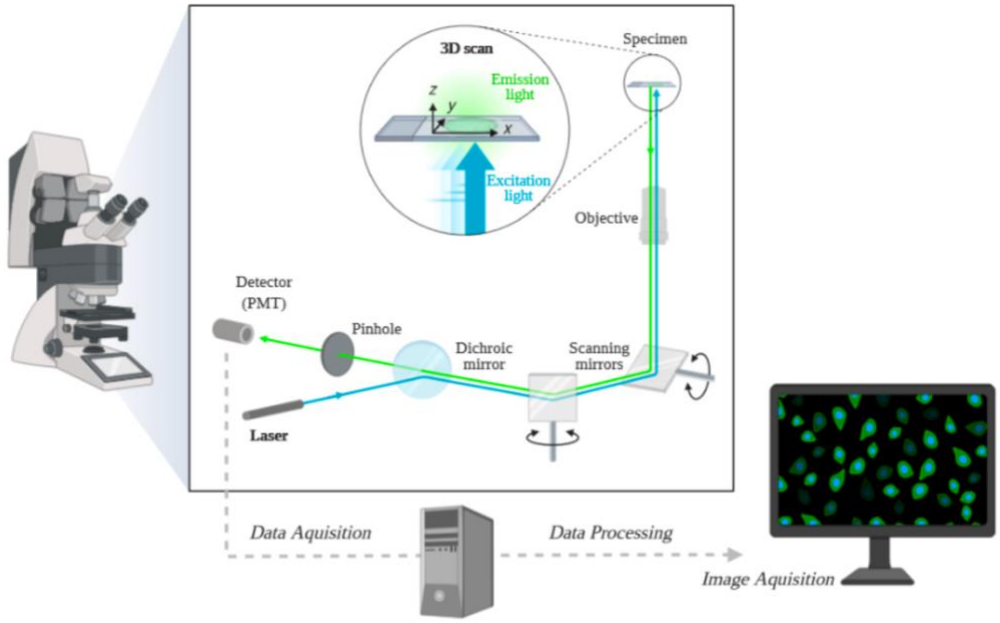

Figure 2.7 – Simplified view of a confocal microscope's functioning. Light from a laser source reaches the dichroic mirror and is reflected to the objective, which focuses the light beam in a spot in the sample. Only the fluorophores excitable by the selected wavelength within the illuminated area will be excited, while all the other molecules outside the focal point will remain in the ground state. Emitted fluorescence will pass through the objective lens, dichroic mirror, and reach the pinhole, which blocks light from the planes above and below the focal plane. Photomultiplier tubes (PMT) detect and multiply the signal to obtain high-quality unblurred images. Created by BioRender.com.

Confocal microscopy was employed in this study to observe samples at different stages of the nuclei isolation protocol and to examine the intranuclear location of lamin A.

2.5. Fluorescence Lifetime Imaging Microscopy (FLIM) & Multi-photon excitation

Fluorescence lifetime of a fluorophore is defined as the average time the molecule spends in the excited state before returning to the ground state [124].

FLIM leverages this property, making it a valuable technique when combined with probes with high sensitivity to the molecular environment or, for example, capable of sensing changes in molecular conformation. Exogenous fluorescent molecules that can monitor environmental parameters such as temperature, viscosity, pH, and ion concentration through changes in their lifetime are categorised as FLIM-based sensors. By using both endogenous and exogenous fluorophores, FLIM can monitor various processes in cells and tissues, including disease progression and drug efficacy [128].

In contrast to standard fluorescence microscopy, which relies on intensity to create images, FLIM uses the fluorescence lifetime of the fluorophore by analysing its exponential decay rate [129]. FLIM quantifies the fluorescence decay rate of a fluorophore, spanning a timescale from sub-nanoseconds to several hundred nanoseconds. In time-domain fluorescence lifetime measurements, a short light pulse excites the sample, which is shorter than the sample's lifetime, and the resulting exponential decay of fluorescence is captured (Figure 2.5) [128].

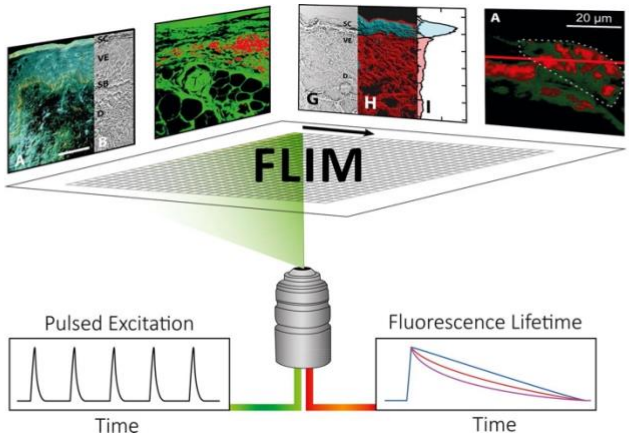

Figure 2.5 - Fluorescence Lifetime Imaging Microscopy (FLIM) setup and data representation. The sample is excited using a series of pulsed laser beams, leading to fluorescence emission. The fluorescence decay over time is recorded, and the fluorescence lifetime is analysed to generate lifetime-based contrast images. The top section shows FLIM images of different tissue regions, where variations in fluorescence lifetimes are color-coded. The graphs at the bottom illustrate the pulsed excitation pattern and corresponding fluorescence decay curves, demonstrating how FLIM distinguishes different molecular environments by their decay kinetics [130].

The most common implementation of FLIM is with a fast electronic method called time-correlated single-photon counting (TCSPC) [131]. In TCSPC, a fast stopwatch measures the time between an excitation photon and an emission photon. This time defines each emission

photon’s time of arrival. A time-amplitude converter circuit (TAC) is used to measure fast clock times experimentally by converting the time at which photons arrive into an analogue voltage, which can then be recorded. In conventional TCSPC, at high photon count rates, most incoming photons will not be measured due to the instrument's dead time, leading to a pile-up effect where only photons with shorter arrival times are recorded per excitation pulse [131]. When photons with longer arrival times are lost, it results in an inaccurate photon histogram, leading to an underestimation of the fluorescence lifetime. To avoid these effects, a low photon count at the detector is desirable, ideally less than 10% of the excitation repetition rate. Generally, time-domain methods detect one fluorescence photon across several excitation pulses, requiring many excitation pulses to build a histogram [131].

FLIM is typically used to capture fluorescence lifetime data across an entire field of view, generating a two- or three-dimensional map of lifetimes, where each pixel represents a fluorescence decay curve. This method allows for detailed spatial mapping of fluorescence lifetimes. However, due to insufficient emission in this study, we opted to combine all detected photons from a specific region into a single decay curve, rather than generating an image. This approach provided accurate lifetime data while simplifying data collection and reducing acquisition time, which was particularly beneficial for minimizing photobleaching . Importantly, multiphoton excitation was used in FLIM experiments to excite the probe Flipper-TR. Multiphoton excitation entails the coincidental absorption of two photons, each with half the energy needed for the same transition in the Jabłoński diagram as would be achieved with single-photon excitation (Figure 2.6) [134]. Despite the use of two photons, typically around 800 nm each, as opposed to a single photon at 400 nm, the excitation results in emission from the same singlet state [134].

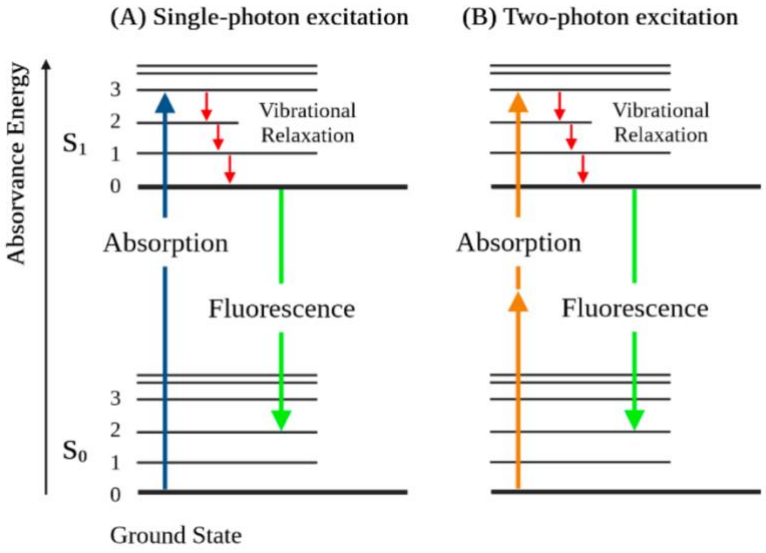

Figure 2.6 - Single-photon and multiphoton (two-photon) excitation diagrams. The diagrams differ on the number of photons absorbed by a molecule (one (**A**) and two (**B**)). In both representations, the absorption of light is depicted as vertical lines pointing upwards that represent transitions between S0 and S1 or S2 (not shown) that occur very fast (10-15 picoseconds). The transition responsible for fluorescence takes place from the zero vibrational state of the first excited state (S1) to one of the vibrational states of the ground state (S0) and is represented by an arrow pointing downwards. Created with BioRender.com.

In this project, by acquiring fluorescence decays of a membrane tension-sensitive probe, the membrane tension of the nuclei was evaluated across ageing.

2.6. Atomic Force Microscopy (AFM)

In this work, AFM is utilized for two distinct purposes, employing different modes for each. In the imaging mode, AFM serves as a valuable tool to validate the efficacy of nuclei isolation. With its atomic resolution, it can confirm if the isolation of nuclei was effective without damage to the nuclear membrane or contamination from other organelles, such as the ER. In the force spectroscopy mode, using highly sensitive tips, the stiffness of the nuclei is studied to determine how ageing influences this parameter.

2.6.1. Imaging mode

AFM is a type of scanning probe microscopy widely utilised in biological research. It measures the force between a sample and a flexible cantilever, which acts as a spring. The AFM detects local attractive or repulsive forces between the tip and the sample by converting these interactions into bending or deflection of the cantilever. This cantilever is attached to a

stable substrate, and depending on whether the force is attractive or repulsive, it bends toward or away from the surface (Figure 2.7) [135].

To produce images, the cantilever deflection is detected and converted into an electrical signal. A common detection method involves using a laser beam reflected from the back of the cantilever onto a detector (Figure 2.7). The optical lever principle amplifies small changes in the cantilever's angle into significant deflections of the reflected laser spot [135]. The forces between the tip and sample alter the angle of the laser beam, shifting the spot on the photodetector, and the signals from the four quadrants of the detector are used to calculate the deflection [135].

Most atomic force microscopes use a four-quadrant photodiode to determine the laser spot's position in two directions. Vertical deflection, representing the interaction force, is measured by comparing signals from the "top" and "bottom" halves of the detector. Lateral twisting is determined by comparing the "left" and "right" halves [135].

In contact mode imaging, the AFM tip remains in continuous contact with the sample surface as it scans (Figure 2.7). A feedback loop controls the deflection of the cantilever, continuously adjusting its height to maintain a constant force between the cantilever tip and the sample surface. This mode is effective for high-resolution topographical imaging of hard samples. For softer biological samples, the force must be carefully controlled to avoid damage [135].

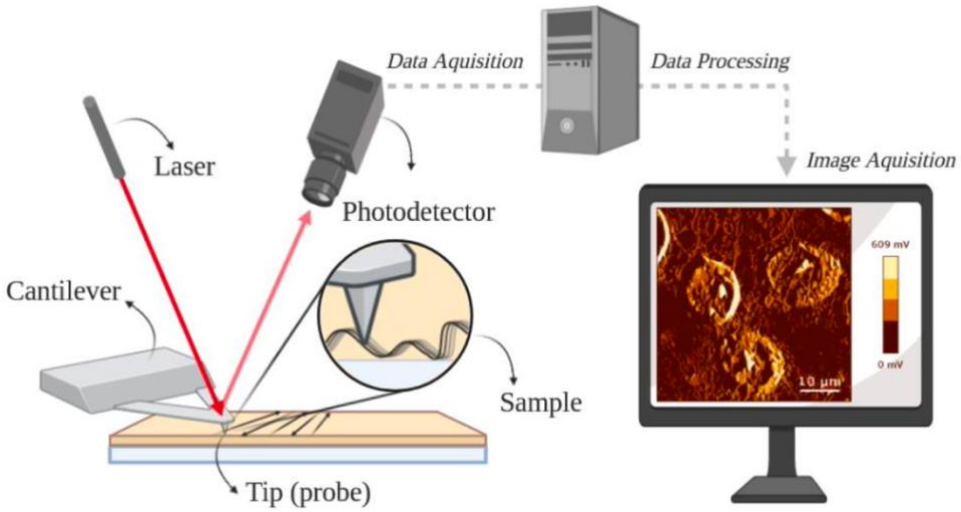

Figure 2.7 - Atomic force microscopy schematic representation. A tip at the end of a cantilever approaches and interacts with the specimen and screens its surface. The interaction between tip and surface topography induces the bending of the cantilever, deflecting the laser that reaches a position-sensitive photodetector. This alters the incidence point of the laser on the detector, providing the software with the information required for image acquisition and 2D reconstruction. Created with BioRender.com.

AFM is particularly advantageous for biological applications because samples can be imaged in their natural state without staining, coating, or electron conduction. This enables high-resolution imaging in physiological buffers or media across various temperatures. AFM can image living cells and single molecules like proteins or DNA, providing 3-dimensional topographical data and insights into mechanical properties and adhesion characteristics [135].

2.6.2. Force spectroscopy mode

Unlike imaging modes that involve scanning the tip across the sample, force measurements are obtained by varying the distance between the tip and the surface at a single point. This technique, known as force spectroscopy, involves moving the base of the cantilever vertically toward the surface using a piezoelectric element and then retracting it (Figure 2.8A)[135]. During this process, the deflection of the cantilever and other signals, such as amplitude or phase changes in dynamic AFM modes, are measured [135]..

Data from force spectroscopy experiments are often presented as simple x-y plots. The x-axis typically represents the height positions during the approach and retraction of the cantilever, while the y-axis shows the measured cantilever property, usually vertical deflection (Figure 2.8B and C). These "force-distance" plots, or force curves, provide a direct measure of interaction forces [135].

The basic principles of force spectroscopy can be illustrated by considering a cantilever in air approaching a material. As the cantilever nears the surface, initial forces are too weak to cause any measurable deflection, keeping the cantilever in its original position. However, the cantilever tip contacts the surface when attractive forces like Van der Waals and capillary forces exceed the cantilever's spring constant [135]. Once in contact, the viscoelastic response of cells (or other materials) can be studied by using the cantilever to indent the cell. During retraction, the tip often stays adhered to the surface due to adhesion, causing the cantilever to deflect downward. Eventually, the cantilever's force overcomes the adhesion, and the tip detaches from the surface (Figure 2.8A) [135].

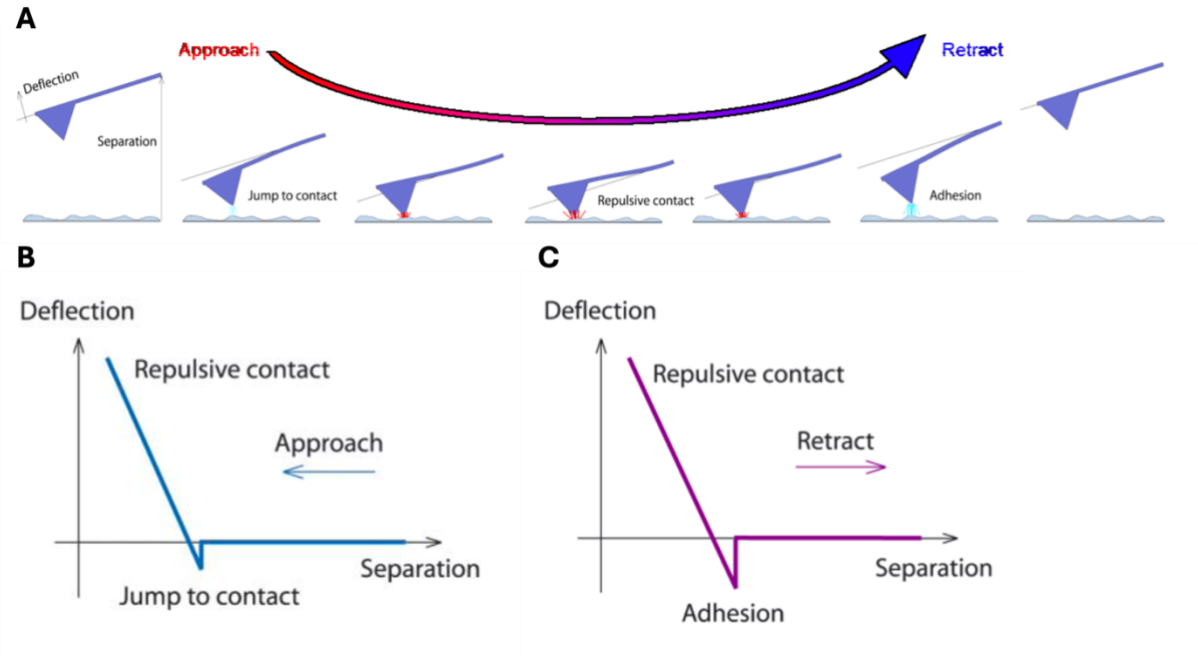

Figure 2.8 – Force Spectroscopy principles scheme. (**A**) The approach and retraction cycle of the AFM probe. During approach, the probe undergoes a jump-to-contact before entering repulsive contact with the sample. Upon retraction, adhesive forces between the probe and sample are overcome before the probe separates; (**B**) Force-distance curve during approach, showing the jump-to-contact followed by repulsive contact; (**C**) Force-distance curve during retraction, highlighting adhesion forces before probe separation from the sample [135].

Young's Modulus is an elastic property that defines a material's ability to withstand stress and is calculated as the ratio of stress to strain in the material. This is a normalised measure of compressibility – the higher the value the stiffer the sample. When a material is uniformly compressed, calculating the Young's modulus is straightforward because the compressed area is clearly defined [135]. However, in AFM measurements, the indentation geometry is more complex, as the surface is indented locally with a tip of a specific shape. This requires a contact model to determine the Young's modulus from AFM data. The Hertz model is the standard model used for this purpose, as it helps extract the Young's modulus from AFM force-distance curves [135]. The Hertz model relies on four key assumptions:

1. **Small Strains**: The material experiences small strains, without significant plastic deformation or fracturing.
2. **Continuous, Non-conforming Surfaces**: The surfaces in contact are continuous and non-conforming, meaning the contact area is much smaller than the object's radius.
3. **Half-space Bodies**: The materials involved can be considered half-spaces, indicating they are thicker than the strains' length.

4. **Frictionless Surfaces**: The surfaces do not experience friction, meaning there is no adhesion between the tip and the sample.

Assumptions 1-3 are often met in practice, and even if they are slightly violated, the effect on the Young's modulus value may be minor [135]. If a specific condition is clearly not met, alternative models should be considered to address the issue. However, assumption 4 is frequently violated, as many materials exhibit adhesion [135]. Despite this, because the focus is usually on comparing groups rather than determining precise Young's modulus values, the Hertz model is widely accepted within the AFM community. For this reason, it will be the model used in this work.

2.7. Transmission Electron Microscopy (TEM)

TEM was utilized to assess the degree of nuclei isolation, playing a key role in refining the nuclei extraction protocol. TEM will deliver high-resolution imaging at each stage of the protocol, from intact cells through to the final isolated nuclei. This method will be instrumental in providing a detailed visual analysis at every step, ensuring the effectiveness of the isolation process.

In the early 20th century, physicists discovered that particles like electrons have wave-like properties when accelerated. This discovery enabled the development of imaging techniques that surpass the spatial resolution of traditional optical microscopes due to the electrons' very short wavelengths [136]. Electrons can be focused because they are negatively charged particles and can be manipulated by electric and magnetic fields. This principle was first applied in early technologies like cathode-ray tubes, television displays, and computer screens [136].

A transmission electron microscope utilizes these properties by directing electrons through a thin specimen and focusing them with lenses. While similar in concept to a light microscope, TEM uses electrons to create images by converting them into photons. It generates images with a high-voltage electron beam produced by an electron gun, which directs electrons through a vacuum tube (Figure 2.9) [137]. As the beam passes through an ultra-thin specimen, an electromagnetic lens focuses the electrons. These electrons then hit a fluorescent screen, producing an image based on the specimen's density. Darker areas on the screen indicate regions that transmitted fewer electrons, while lighter areas show where more electrons passed through. The resulting image can be directly analysed or photographed for further examination [138].

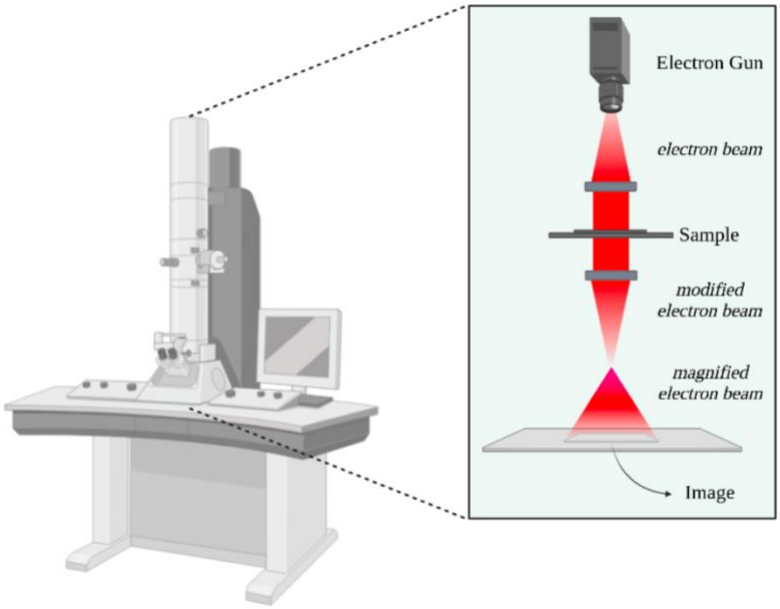

Figure 2.9 - Transmission electron microscope. A beam of electrons is shone on a slice of fixed sample, passing through it. The electrons interact with the different structures on the sample, are scattered by them, and the beam is changed according to the sample's characteristics. The alterations on the beam (scattered electrons) are transmitted, magnified, and detected to form a black and white pattern. This pattern represents the passage of the electrons through the sample, giving the user very detailed information regarding the sample. Created with BioRender.com.

2.8. Fluorescence spectroscopy

2.8.1. Generalized Polarization (GP)

GP is a parameter that reflects changes in the emission spectrum of environment-sensitive fluorescent dyes. These dyes respond to shifts in their surroundings, such as variations in membrane lipid phases, by altering their emission wavelength. The GP value provides a quantitative measure of the dye's response to changes in membrane fluidity, enabling researchers to assess the phase behaviour of lipid bilayers as they transition between solid (gel) and fluid (liquid-crystalline) states. This measurement has expanded its applications to studying how membranes move and interact with proteins [139].

A variety of environment-sensitive dyes can be used to calculate the GP of a membrane. Among the most commonly used is Laurdan, which is particularly sensitive to the packing and phase of lipid bilayers. [140]. When lipid membranes shift between phases, the interactions between the dye and surrounding water molecules are altered, leading to a shift in emission wavelengths. For example, in a solid (gel) phase, Laurdan typically emits at 440 nm, while in

a fluid (liquid-crystalline) phase, it mostly emits at 490 nm (Figure 2.10). These water molecules are situated near the glycerol backbone of the lipid, right where Laurdan's structure (its naphthalene part) is located. The presence and behaviour of these water molecules influences how they orient themselves around Laurdan when it is excited by light. This orientation is faster in the fluid phase, making it a critical indicator of the lipid state [140].

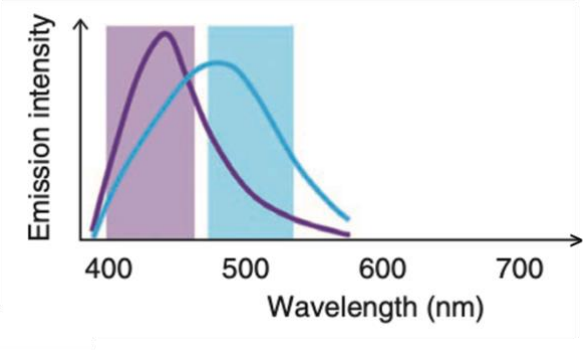

Figure 2.10 - Schematic representation of the fluorescence emission of Laurdan in different lipid phases. The dye fluoresces with a peak emission wavelength around 440 nm (violet) when residing in the gel phase and at 490 nm in the fluid-liquid crystalline phase (blue) [141].

In this thesis, Laurdan GPs were calculated to assess the membrane order of LUVs prepared using lipids extracted from nuclei. These were compared to control LUVs composed of commonly studied lipids such as POPC and DPPC.

2.8.1.1. GP from cuvette to microscope

In moving GP measurements from cuvette-based assays to microscopic techniques, researchers have achieved a significant leap in how lipid bilayers and other biological membranes are studied. This shift not only enhances the precision of measurements but also pinpoints specific locations within cellular structures, enabling submicron resolution analysis of membrane dynamics and composition [140].

Originally, cuvette-based GP measurements provided averaged fluorescence data over large volumes, which could obscure detailed interactions and localized phenomena. The integration of GP with microscopy methods, such as confocal and two-photon fluorescence microscopy, overcomes these limitations by allowing direct visualization of lipid domains and microenvironment interactions within cells [142]. This refined approach reveals how membranes behave under various conditions, such as changes in temperature, drug interactions, or protein binding, which are critical for understanding cellular processes [140, 142].

Furthermore, the development and improvement of fluorescent probes and optical systems have significantly expanded the capabilities of microscopic GP approaches by allowing for more precise detection of membrane changes and real-time imaging of dynamic processes in complex biological systems [141]. Researchers can now obtain detailed quantitative data that contributes to more accurate models of cellular behaviour and membrane dynamics.

For this project, microscopic GP measurements were conducted using a polarity-sensitive probe other than Laurdan, specifically Di-4-ANEPPDHQ, to assess the membrane order of the nucleus.

3. MATERIALS AND METHODS

3.1. Cell Culture

3.1.1. Primary Human Fibroblast Culture

Nine different cell lines of Human skin fibroblasts were cultured.

Five of these were purchased from the Coriell Institute for Medical Research (Camden, NJ, USA), specifically from the NIA Aging Cell Culture and NIGMS Human Genetic Cell Repositories. Fibroblasts were obtained from the skin of a healthy young 3-month-old female (HY-F) donor (GM00041G), a HY-F 2-year-old female donor (GM00969I), a HY-M 1-year-old male donor (GM05659M), a HY-M 3-year-old male donor (GM00498G), and an 8-year-old female HGPS patient (AG08466).

The fibroblasts from healthy older donors (HO) were obtained from skin biopsies performed at the Department of Dermatology of Hospital de Santa Maria, Centro Hospitalar Universitário Lisboa Norte: a HO-M 56-year-old male donor (273074), a HO-F 59-year-old female donor (284401), and a HO-F 79-year-old female donor (274516), sourced from Biobanco-IMM, Lisbon Academic Medical Centre, Lisbon, Portugal.

The ninth cell line was also acquired in Biobanco-IMM, Lisbon Academic Medical Centre, Lisbon, Portugal. It was from a 49-year-old female donor (271663) and was used for all optimisation steps.

These primary cells were cultured in T75 flasks using Dulbecco's Modified Eagle's Medium-high glucose (Sigma-Aldrich), supplemented with 15% fetal bovine serum (FBS) (Sigma-Aldrich), 1% Penicillin-Streptomycin, and MEM Non-essential Amino Acid solution (Sigma-Aldrich). Cell passages were performed every 3 days at a 1:2 or 1:3 ratio using TrypLE Express (Sigma-Aldrich), and the medium was changed between passages.

In brief, cells were washed with phosphate-buffered saline (PBS) (Sigma-Aldrich), followed by incubation with 2 mL of TrypLE for 5 min at 37 °C, with subsequent inactivation by adding 3 mL of medium. Afterwards, the cells underwent a centrifugation step for 5 min at 21 ºC and 1,200 rpm, the supernatant was discarded, and the pellet was resuspended in fresh medium and cultured in a new T75 flask.

3.2. Cell Nuclei Isolation

The nuclei isolation was conducted when cellular confluency reached 80% or higher of a T75 flask. Hoechst 33342 (Invitrogen) was utilised for nuclei staining (1:2000 in PBS, according to the manufacturer's instructions). The staining was conducted at 37 °C for 10 min.

Subsequently, the cells were washed with PBS and detached with TrypLE at 37 °C for 5 min. Two centrifugation steps were carried out. The first was at 21 °C, 1,200 rpm for 5 min, with a subsequent wash of the pellet using 3 mL of PBS. The second centrifugation step was performed at 4 °C, 4,000 rpm for 10 min. The supernatant was discarded. The subsequent steps of the protocol were executed on ice.

The resulting pellet was solubilized with 1 mL of hypotonic buffer (HB) (10 mM Tris-HCl (Sigma-Aldrich), 2 mM $MgCl_2$ (Sigma-Aldrich) and cOmplete protease inhibitor cocktail 1x (Roche)) and left incubating for 20 min on ice. To rupture the cellular membranes, three freeze/thaw cycles were conducted (40 °C/liquid nitrogen). The solution was then rendered isotonic by adding 110 µL of 10x PBS. The sample was passed through a 100 µm cell strainer (Corning) and subsequently transferred to a fluorescence-activated cell sorting (FACS) tube. Nuclei were sorted using a BD FACSAria Fusion (BD Biosciences) configured with a 405 nm laser, BP 450/40 filter, and a 100 µm nozzle (except otherwise stated). The gating strategy began by identifying cell populations through the side scatter area (SSC-A) and forward scatter area (FSC-A) to exclude debris. Doublets were discriminated by plotting forward scatter height (FSC-H) against forward scatter area (FSC-A), allowing for the selection of singlet nuclei. Subsequently, nuclei were identified by gating SSC-A against the Hoechst area (Hoechst-A) to select Hoechst-positive events. Sorted nuclei were collected in 1.5 mL Eppendorf tubes containing 150 µL of PBS supplemented with protease inhibitors 1x.

This protocol was performed with two other probes, NucRed (Invitrogen) and DRAQ5 (Invitrogen). For NucRed staining, 2 drops/mL were added to the culture flask containing 5 mL of PBS, and the flask was kept at 37 °C for 15 minutes. For staining with DRAQ5, 1 µL of the dye was added to 5 mL of PBS, and the flask was kept at 37 °C for 2 minutes.

3.3. Flow Cytometry

The BD Accuri C6 flow cytometer (BD Biosciences) was configured with a 640 nm laser and a BP 675/25 filter. Performance validation was done according to instructions (BD Accuri C6 Software User Guide). The gating strategy began by identifying cell populations through the side scatter area (SSC-A) and forward scatter area (FSC-A) to exclude debris. Doublets were discriminated by plotting forward scatter height (FSC-H) against forward scatter area (FSC-A), allowing for the selection of singlet nuclei. Subsequently, NucRed positive nuclei were identified by gating SSC-A against the NucRed area (NucRed-A). Threshold levels were set empirically to eliminate from detection the large amounts of irrelevant debris that are found in the sample after freeze/thaw cycles. The flow cytometer was operated at the medium flow

rate setting (35 µL/min), and data acquisition was done with 100 µL stopping criteria. The data was used to make counts before and after sorting to gather information about how many nuclei were being lost with different sorting configurations.

3.4. Staining protocols

3.4.1. For Nuclei isolation protocol validation

The nuclei and the cells before and after the HB were already labelled with Hoechst as they were sorted using that dye. Both were placed in an 8-well ibiTreat plate (ibidi) previously coated with poly-L-lysine (PLL; Sigma-Aldrich) for 1 h at room temperature. For adherent cells, Hoechst labelling was performed for 10 minutes at 37 °C in a 1:2,000 dilution in PBS. CellMask (Invitrogen) was added at the same dilution in PBS immediately before acquisition.

3.4.2. For Lamin A observation

For lamin A labelling, nuclei were fixed with 4% formaldehyde in PBS for 10 minutes, followed by three washes with PBS. Permeabilization was performed using 0.1% Triton X-100 in PBS for 5 minutes, followed by three additional PBS washes. Blocking was achieved with 5% bovine serum albumin (BSA; Sigma-Aldrich) in PBS for 1 hour and 45 minutes. Primary antibody staining was performed by incubating the samples with mouse monoclonal lamin A/C antibody (Abcam) overnight at 4 °C, followed by three washes with PBS. This was followed by incubation with an Alexa Fluor 488-conjugated goat anti-mouse IgG secondary antibody (Abcam) for 45 minutes at room temperature.

3.4.3. For Di-4-ANEPPDHQ staining

The staining was performed according to the method outlined in [141], with some modifications detailed below.

After allowing the nuclei to adhere to the ibidi plate, the buffer was removed, and 200 µL of a solution of 1:1,000 Di-4-ANEPPDHQ (Invitrogen) in PBS was added. The samples were then incubated at 37 °C for 15 minutes.

3.4.4. For Flipper-TR staining

This staining process was similar to the previous one with Di-4-ANEPPDHQ, except after removing the buffer, 2 µM Flipper-TR (SPIROCHROME) solution (in PBS) was added. After a 5-minute incubation at room temperature, the samples were incubated for an additional 5 min at 37 °C.

3.5. Confocal Microscopy

3.5.1. For nuclei protocol isolation validation

Confocal images were acquired using an inverted confocal point-scanning confocal microscope (Zeiss LSM 710 and 880). The microscope was equipped with two sensitive photomultiplier tubes (PMT) and a 63x Plan-Apochromat oil objective (Zeiss) with a numerical aperture of 1.40 and a working distance of 0.17 nm. Hoechst was excited using a 405 nm laser, and CellMask with a 561 nm laser. The detection ranges for the PMTs were as follows: Hoechst – 415-478 nm; CellMask – 571-750 nm. The images were acquired using ZEN 2.3 SP1 (black edition, Zeiss) software with the following parameters: 1024x1024 pixel images pixel dwell time of 5.68 µs, line averaging set to 2, and pinhole set to 1 airy unit (1.0 µm). Laser power and gains were adjusted according to the staining efficacy.

3.5.2. For Lamin A observation

The study included four young donors (HY-F GM00041G, HY-F GM00969I, HY-M GM05659M, HO-M GM00498G), three old donors (HO-M 273074, HO-F 274516, HO-F 284401), and an 8-year-old female HGPS patient (AG08466). The same equipment, acquisition software, and parameters used for the images in the nuclei isolation protocol validation were applied, with the addition of the following settings: Alexa Fluor 488 was excited using the Argon laser line at 488 nm. The detection range of the PMT was set to 498-550 nm. The images were analysed in Fiji/ImageJ (version 1.54f), and the aspect ratio (AR) of the nuclei was calculated according to equation (1) below.

$$AR = \frac{Major\ axis}{Minor\ axis} \quad \textbf{(1)}$$

Fifty confocal images of nuclei labelled with Lamin A were acquired per donor.

3.5.3. For Di-4-ANEPPDHQ GPs

For this step, the protocol defined by Dylan M. Owen *et al.* was followed [141]. Forty confocal images were acquired per donor, including one young donor (HY-M GM05659M), two old donors (HO-M 273074, HO-F 274516), and an HGPS patient (AG08466), using the same equipment, objective and acquisition software as described in section 3.5.1. The Argon ion laser line at 488 nm was employed to excite the dye. The PMT detection ranges were set to 500-580 nm and 620-750 nm. Images were acquired with the following parameters: 512x512 pixel images, pixel dwell time of 3.46 µs, line averaging set to 4, zoom at 3, and a pinhole set

to 1 airy unit (1.0 μm). Laser power and gains were adjusted according to the staining efficacy. The images were analysed in Fiji/ImageJ, and the Di-4-ANEPPDHQ GPs of the nuclei were calculated according to equation (2) below.

$$GP = \frac{I_{500-580} - GI_{620-750}}{I_{500-580} + GI_{620-750}} \quad \textbf{(2)}$$

The G factor (also known as the instrumental correction factor) accounts for differences in the detection efficiency of the two channels or detectors used to measure fluorescence. Since different wavelengths may be detected with varying sensitivity by the instrument, the G factor compensates for these discrepancies, ensuring the accurate calculation of GP by correcting the intensity measurements from different wavelength ranges. In other words, the G factor normalizes the fluorescence intensities, allowing for a fair comparison between the different emission ranges.

3.6. Lifetime Measurements

FLIM measurements were conducted on 40 nuclei per donor, involving samples from 2 young donors (HY-M GM00498G, HY-F GM00969I) and 2 old donors (HO-M 273074, HO-F 274516). These measurements were carried out using a Leica TCS SP5 inverted microscope (DMI6000, Leica) equipped with a 63x water immersion apochromatic objective with a numerical aperture of 1.2. The process employed TCSPC, utilizing a multiphoton Titanium laser (SpectraPhysics Mai Tai BB, 710–990 nm, 100 femtosecond pulses, 80 MHz) as the excitation source. Flipper-TR, the probe used to report on the membrane tension of the nucleus, was excited at 800 nm, and fluorescence emission was acquired at 500-680 nm. The PMT was connected to the X-port of the microscope, and the emitted photons were processed by an SPC board that simultaneously records the (x, y) coordinates of the collected photons (Becker and Hickl, GmbH, PMC-100-4 SPC-830). The laser power was adjusted to achieve an average photon count rate of over $5x10^4$ photons per second. Fluorescence lifetimes were determined by analysing the fluorescence single decays through a least squares iterative re-convolution of decay functions with the instrument response function (IRF) using the SPC Image software (Becker and Hickl, Berlin, Germany). The fluorescence emission decay curves were fitted with double exponentials according to the equation (3), from which two lifetimes (τ_1 and τ_2) and two intensities (I_1 and I_2) could be extracted.

$$I(t) = B_1 \times e^{\frac{-t}{\tau_1}} + B_2 \times e^{\frac{-t}{\tau_2}} \quad \textbf{(3)}$$

where I(t) is the fluorescence intensity as a function of time *t*, τ_i is the i^{th} component of the fluorescence lifetime and B_i is the fractional amplitude of each component.

In this assay, the first lifetime component, τ_1, contributes only a small portion of the signal, with a lower photon count (I_1). The lifetime data reported in the results and used for conclusions are based on the longer component, τ_2. This is justified because τ_1 values are more subject to errors, as they are smaller and account for fewer emission events.

3.7. Atomic Force Microscopy (AFM)

3.7.1. Imaging Mode

AFM images were obtained using adherent cells, cells before and after treatment with HB, and nuclei from donor 271663 using a NanoWizard II atomic force microscope (JPK Instruments) mounted on an Axiovert 200 inverted optical microscope (Zeiss). The AFM head was equipped with a 15 μm z-range linearized piezoelectric scanner and an infrared laser. Sample preparation involved placing a drop of the sample on a saline-coated coverslip and allowing it to settle under gravity for at least 30 minutes. In the case of adherent cells, these were cultured in tissue culture dishes 40x11mm (TPP). The medium was removed, and the cells were washed once with PBS. The samples were then fixed with a 2.5% glutaraldehyde solution in PBS for 10 minutes at room temperature, followed by three washes with PBS, and a final one with distilled water. After air-drying the coverslip, or the tissue culture dish, at room temperature and positioning it in the microscope, the cantilever was brought into contact with a single cell or nucleus with the assistance of a CCD camera (Zeiss). Images were recorded with 512x512 pixel image at a line rate of 0.3 Hz. Imaging parameters were adjusted to minimize the force applied on the scanning of the topography of the cells. Images were analysed using JPK image processing software v. 5.0.133.

3.7.2. Force Spectroscopy mode

AFM-FS measurements were performed on the same equipment as in section 3.7.1, using triangular cantilevers with a pyramidal tip with a radius of 15 nm and a resonance frequency of 15 kHz in air (MSNL-10 tip D, Bruker). The AFM head was equipped with a 15 μm z-range linearized piezoscanner and an infrared laser. The spring constant of the tips was calibrated using the thermal fluctuation method, yielding values of 0.03 ± 0.01 N/m. Experiments were conducted at room temperature. Measurements were conducted in liquid using PBS. Sample

preparation involved placing a drop of the sample on a silane-coated coverslip and allowing the nuclei to settle under gravity for at least 30 min. Each experiment was performed for 1h30, with a subsequent 1h30 break to allow the equipment to cool down and to change the sample between intervals. For each nucleus, five different points were chosen, and ten force curves per point were acquired. Fifty force curves per nucleus were analysed. In total, 40 nuclei were analysed for each donor, using 3 young donors (HY-M GM05659M, HY-M GM00498G, HY-F GM00041G), 3 elderly donors (HO-M 273074, HO-F 274516, HO-F 284401), and the patient (HGPS-F AG08466). Force curves were analysed using the JPK image processing software v. 5.0.133 (JPK Instruments) and the Hertz model. The Youn's Modulus (E) was calculated according to the equation (4) below.

$$E = \frac{F \times L}{\Delta L \times A} \quad \textbf{(4)}$$

In the equation, F represents the applied force, , and L is the original length of the material. ΔL, refers to the change in length (elongation or deformation) of the material under the applied force. Lastly, A is the cross-sectional area of the material.

3.8. Transmission Electron Microscopy (TEM)

Transmission electron microscopy (TEM) was used to examine intact cells, cells before and after exposure to the HB, and isolated nuclei from donor 271663. Samples were prepared as follows: 200 µL of the sample suspension was transferred to Poly-L-Lysine (PLL)-coated 8-well ibidiTreat plates (Ibidi), and the samples were allowed to settle by gravity for 30 minutes. An equal volume of double-concentration fixative in 0.1 M phosphate buffer ($Na_2HPO_4 \cdot 7H_2O$ 0.075 M, H_4NaO_5P 0.025 M, pH 7.4) containing 5% glutaraldehyde and 4% formaldehyde was gently added and incubated for 60 minutes on ice. After fixation, the fixative was removed, and the samples were washed twice in 0.1 M phosphate buffer.

Meanwhile, low melting point agarose was prepared by melting it in an Eppendorf tube placed in boiling water. Once liquified, the Eppendorf tube was kept in a 40 °C dry bath to ensure stabilization at this temperature, so it was not too hot for the samples and not solid when needed. 75 µL of 2% low melting point agarose were added to the samples and allowed to solidify on ice. Afterwards, phosphate buffer was added on top to prevent the samples from drying out until they arrived at the electron microscopy facility at the Instituto Gulbenkian de Ciência (IGC, Oeiras, Portugal).

The agarose pellets were cut from the ibidi plate, sectioned into small cubes of approximately 1 mm, post-fixed for 1 hour on ice in 1% osmium in 0.1 M phosphate buffer, and washed twice in 0.1 M phosphate buffer and twice in distilled water for 5 minutes each. After washing, samples were stained with 1% tannic acid for 20 minutes on ice, washed five times with distilled water, and stained with 0.5% uranyl acetate for 1 hour at room temperature. Dehydration was performed with a graded series of ethanol (30%, 50%, 75%, 90%, 100%), and samples were infiltrated with 25%, 50%, and 75% resin in ethanol for 90 minutes each, followed by 100% resin overnight.

Samples were embedded with Embed-812 epoxy resin, and the blocks were polymerized at 60 ºC for 24 hours. The sample blocks were sectioned into thin sections of 70 nm on slot palladium copper grids and post-stained with 2% uranyl acetate in 70% methanol and Reynolds lead citrate for 5 minutes each. Samples were observed using an FEI Tecnai G2 Spirit BioTWIN transmission electron microscope operating at 120 keV, and data was collected with an Olympus-SIS Veleta CCD camera. We acknowledge the Electron Microscopy Facility at the Instituto Gulbenkian de Ciência for supporting this work.

3.9. Nuclear lipid extraction

Nuclear lipid extraction was achieved using the Bligh and Dyer method, as previously described [143]. Briefly, nuclei samples were transferred to refrigerated glass PYREX tubes, added 3.75 mL of a 1:2 (V/V) $CHCl_3$:MeOH mixture and vortexed vigorously. The mixtures were left on ice for 30 minutes, after which 1.25 mL of chloroform and 1.25 mL of Milli-Q water were added, with vortexing in between steps. The tubes were then centrifuged for 5 minutes at 1,000 rpm, and the organic phase (bottom phase) was collected in another glass tube. An additional 1.88 mL of chloroform were added to the tube containing the aqueous phase, which were spun again. The organic phase was collected in the same tube as before.

3.10. Liposome preparation

LUVs were prepared using the thin-film hydration method followed by extrusion of multilamellar vesicles. Briefly, lipid mixtures, consisting of DPPC and POPC at 0.5 mM or lipid extracts, were dissolved in chloroform. POPC LUVs were done with and without 1,2-dioleoyl-sn-glycero-3-phosphoethanolamine-N-(lissamine rhodamine B sulfonyl) (ammonium salt) (Rhod-DOPE) at 1:250, 1:350, and 1:500 ratios, and with Laurdan at a 1:100 ratio. DPPC and lipid extract LUVs were prepared with Laurdan at a 1:100 ratio. The solvent was evaporated under a nitrogen stream, resulting in the formation of thin lipid films on the walls

of the Eppendorf tube. The samples were then placed under vacuum for 3 hours to ensure complete removal of the solvent. Afterward, the lipid film was re-suspended in filtered PBS (0.1 µm, Corning). To homogenize the vesicles, the suspension underwent six freeze-thaw cycles (liquid nitrogen/50 °C) with vortexing after every two cycles. Finally, the lipid suspension was extruded 21 times at 50 °C through a 200 nm polycarbonate membrane (Merck) using an Avanti Mini-Extruder. The resulting LUVs were transferred to a new Eppendorf tube.

3.11. Small Particles Detection

A 5-laser Cytek Aurora Flow Cytometer equipped with SPECTROFLO software (Cytek Biosciences Inc) and a 0.04 µm sheath filter assembly were used. The equipment was left overnight in a 30% Contrad 70 (VWR) solution, and before the acquisition, a 1h30-minute cleaning was performed with filtered Milli-Q water using a 0.1 µm filter to minimize background noise. ApogeeMix beads (Apogee Flow Systems) were used for calibration, and acquisition settings were optimized to visualize nanoparticles of varying sizes. Initial assay controls were performed using PBS and Milli-Q water filtered with a 0.1 µm PS filter, unstained POPC LUVs in PBS with a final lipid concentration of 0.5 mM, and a Rhod-DOPE 0.6 µM solution in PBS. Stained POPC LUVs (0.5 mM) were obtained by adding Rhod-DOPE at probe/lipid ratios of 1/500, 1/350, and 1/250. Seven serial dilutions of the unstained and stained LUVs were performed, starting at 1,000 times dilution and progressing to 3,000, 9,000, 27,000, 81,000, 243,000, and 729,000.

The data were collected on the Cytek Aurora flow cytometer with an SSC-600 threshold, SSC gain of 2500, gains over 200%, and a 2-minute stopping criterion for sample collection. Events were manually gated to exclude background noise, and only events in the LUVs size range (gated as “Rhodamine+”) were included. Flow data was analysed using FlowJo Software for Windows Version 10.8.1 (FlowJo LLC).

3.12. Generalized polarization

Fluorescence measurements were carried out with a Varian Cary 50 Scan UV-VIS Spectrophotometer (Santa Clara). The light source was a full spectrum Xe pulse lamp single source and a Czerny-Turner monochromator and the detector a PMT. Quartz cuvette (0.5×0.5 cm) from Hellma Analytics were used. The fluorescence intensity of the liposome buffer was always subtracted from the measured fluorescence signals. The acquisition settings were set as the following: λ_{exc} – 360 nm; emission wavelength (λ_{em}) – 380-650 nm; the gains and integration time were changed according to fluorescence intensity of the samples.

The Laurdan GPs were calculated according to equation (5) below.

$$GP = \frac{I_{440} - I_{490}}{I_{440} + I_{490}} \quad \textbf{(5)}$$

Where I_{440} and I_{490} are the fluorescence emission collected at 440 and 490 nm, respectively.

4. RESULTS AND DISCUSSION

4.1. Difficulties in working with primary cells

Working with human primary cells presents significant challenges. This process requires approval from an ethics committee, securing informed consent from donors, and establishing a protocol in collaboration with a hospital to procure biopsies. Additionally, the success of such studies relies on the willingness of individuals to participate. In this project, we initially planned to include four donors per condition (young, old, and patients with HGPS) with equal representation of both sexes. However, this proved to be highly challenging. Obtaining biological samples from minors, excluding blood, remains particularly difficult in Portugal. Furthermore, considering that HGPS affects only about 1 in 20 million people worldwide [144], acquiring these samples was particularly challenging, especially given the inexistence of Portuguese samples. This led us to acquire samples from biobanks abroad, in this case, from the USA. Nonetheless, the acquisition of biological samples requires thorough justification, and ultimately, we were able to obtain four samples from four different young donors, but only one sample from an HGPS patient. Regarding samples from older donors, these were acquired from patients at Hospital de Santa Maria. However, due to the project's exclusion criteria (no lipid metabolic diseases, such as diabetes, no skin diseases, and over 55 years old) and the limited availability of skin fibroblasts meeting these criteria at iMM-biobank, we were only able to obtain three samples from three different donors.

Due to the limitations in finding a sufficient number of donors, particularly for rare conditions like HGPS, we adapted our study design to ensure statistical robustness. Specifically, we conducted detailed analyses of 40 nuclei per donor across the available donors. This approach allowed us to achieve sufficient statistical power to make meaningful comparisons and draw conclusions or identify trends, despite the limited sample size. This methodology ensured that the study could still provide valuable insights, even with the constraints on donor availability.

4.2. Nuclei isolation protocol optimisation

The initial phase of this project was dedicated to optimising and establishing a protocol for nuclei isolation, prompted by observations that each confluent T-Flask of fibroblasts, containing approximately 700,000 cells, typically yielded only a few tens of thousands of nuclei. The protocol began by suspending the cells in a HB to induce swelling. This was followed by four freeze/thaw cycles (alternating between liquid nitrogen and a 40 °C water

bath) with 20 seconds of vortexing between each cycle. After these steps, the sample was processed through a sorter. Optimisation efforts entailed a comprehensive examination of each step, ranging from the detachment of cells from culture flasks to the final preparation of the collection tube for isolated nuclei.

First, we considered two methods for detaching cells: using cell scrapers and enzymatic trypsinization. Cell scrapers, a prevalent tool for mechanically removing cells from culture plates, are straightforward, cost-effective, and provide immediate results. However, this method is notably harsh, often resulting in plasma membrane damage, cell death, and potential damage to other intracellular organelles. The effectiveness of cell scrapers is also highly dependent on the operator technique, limiting detachment to only the areas the tool contacts. Conversely, the application of trypsin to cells, despite not yielding immediate results due to the required incubation period, proved to be more effective for comprehensive cell detachment. Trypsin enzymatically cleaves proteins that anchor cells to the culture surface, thus facilitating their complete detachment. A previous study has confirmed that trypsinization increases cellular susceptibility to osmotic stress by altering cell surface proteins and compromising membrane integrity [145]. For our nuclei isolation purposes, the induction of osmotic stress was both intentional and beneficial. The introduction of an HB induced an osmotic imbalance, leading to cell lysis. Consequently, the addition of the HB post-trypsinization significantly enhanced the efficiency of the process. Our findings demonstrated a slightly increase in recovery rate of nuclei when using TrypLE, a trypsine-like enzyme-based reagent, as compared to cell scraper methods, since the cellular pellets become bigger and *e.g.* we passed from 38,750 to 72, 985 nuclei.

Then, we attempted to add a centrifugation step before sorting after the cycles, aiming to concentrate the nuclei (in the pellet) and separate them from cellular debris (that remains in the supernatant). However, this approach proved ineffective, as it resulted in a significantly reduced number of recovered nuclei (*e.g.* 28,324 nuclei). This outcome can be explained by the fact that the centrifugal forces, combined with the pressure experienced within the sorter, can be detrimental to the nuclei. They may not withstand the process and can end up rupturing.

Therefore, in an attempt to increase the yield of recovered nuclei at the conclusion of the sorting process, we initially hypothesised that starting with a higher number of cells would be beneficial. Normally, each sample tube contains cells derived from two T-flasks to increase the number of cells per tube. We attempted to increase the cell yield further by using cells from three T-flasks per sample tube. Contrary to our expectations, this adjustment did not enhance the recovery of nuclei, continuing to not exceed the mark of tens of thousands of recovered

nuclei. The ineffectiveness of this approach can be attributed to several factors. Primarily, the HB is designed to facilitate the influx of water into cells by creating an osmotic gradient. When the cell concentration is excessively high, this gradient may not be steep enough to induce the intended osmotic effects, thus diminishing the buffer's efficacy. Additionally, increased cell density raises the likelihood of cellular aggregation, which can interfere with uniform buffer-induced swelling across all cells. The sorting process itself also complicates matters by introducing variables related to the increased volume of objects (such as nuclei, cellular debris, swelled cells, and intact cells) in the sample. Even when the acquisition times are kept constant (being the time of sorting the same), higher cell densities can lead to aggregation, causing nuclei to exceed the size threshold for "normal" nuclei sorting gates. Prolonged waiting times can also be detrimental, potentially leading to the rupture of nuclei due to osmotic pressure changes over time, thereby further compromising the overall recovery of viable nuclei.

Subsequently, we shifted our focus from attempting to increase the number of recovered nuclei to investigating the reasons behind the consistently low yield. To do this, we sorted samples in three different steps of the protocol: cells in suspension (before the HB), after the HB , and finally, after the freeze/thaw cycles. The number of events recovered is presented in Table 4.2 and the plots obtained in Figure 4.1.

Table 4.2 – Number of events recovered after sorting of cells in suspension, cells after hypotonic buffer (HB) and isolated nuclei. The number of events is obtained by the equipment.

Sample name	Counts
Cells in suspension	298,852
Cells after HB	397,408
Isolated nuclei	12,442

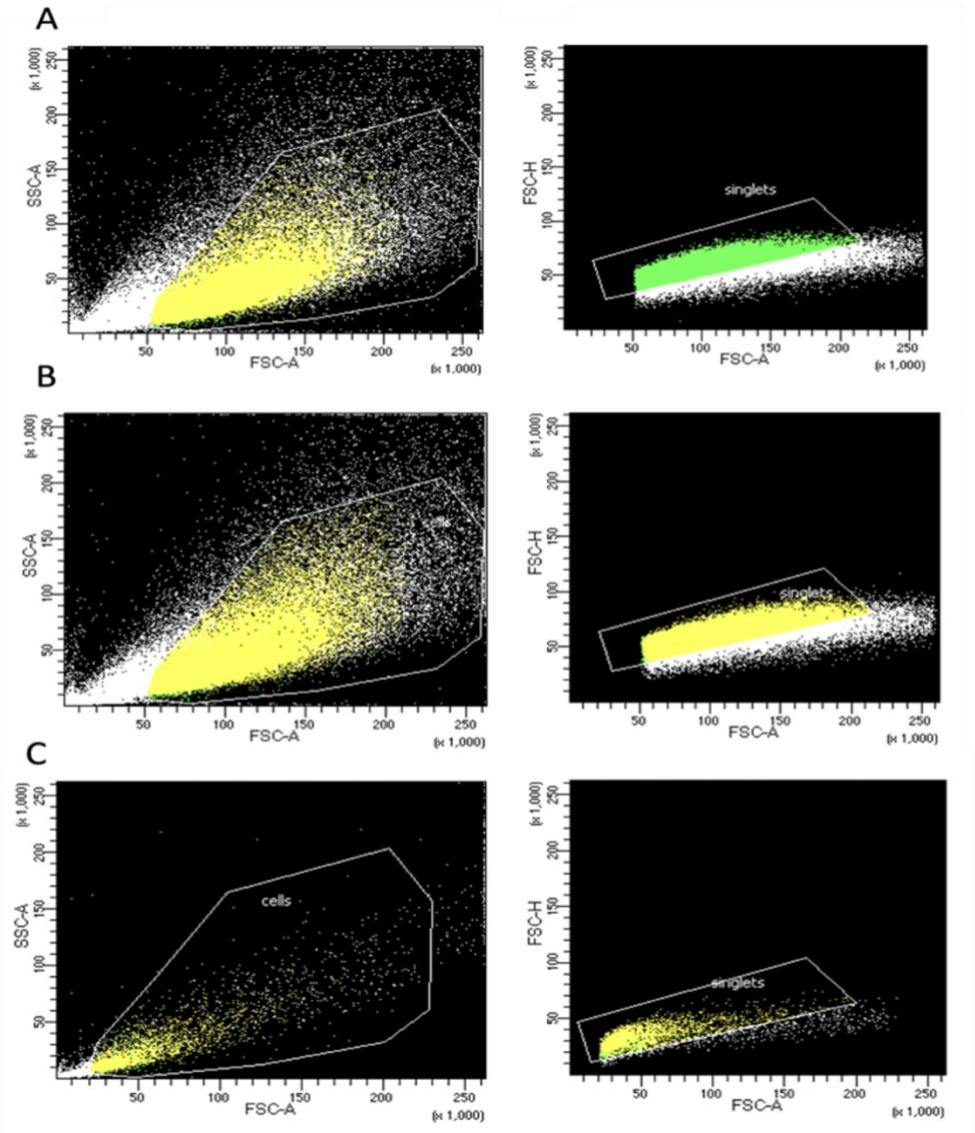

Figure 4.1 – Dot plots showing the sorting data from samples in three different conditions: cells in suspension (A), cells after hypotonic buffer (HB) (B) and the isolated nuclei (C). The first gate (left) excludes the debris and possible aggregates by displaying the data according to their complexity (side scatter-area in the y-axis) against their size (forward scatter-area in the x-axis). The second gate (right) excludes doublets by putting the forward scatter-height against forward scatter-area parameters. Results obtained from samples from donor HO-F 271663.

Upon analysis of Figure 4.1, the apparent increase in cell numbers following HB treatment can be attributed to the fact that the experiment was conducted using three independent tubes, each tube representing a different condition and originating from distinct T-flasks, thereby containing varying cell numbers. However, these samples are comparable as all external variables were controlled: preparations were made on the same day, under the same conditions, and by the same operator. Notably, a significant difference is observed in the number of events after HB compared to the number of isolated nuclei, with counts dropping from hundreds of

thousands to tens of thousands. This stark reduction leads to the conclusion that the freeze/vortex/thaw cycles were the cause of achieving the small recovery of isolated nuclei.

With that in mind, the first modification to the protocol involved the elimination of the vortexing step, which was initially included to potentially dislodge organelles and membrane remnants from the nuclei. However, evidence suggests that vortexing is not suitable for this process. Concurrently, further optimization was achieved by reducing the number of freeze/thaw cycles from four to three, which significantly influenced the outcomes. With these adjustments, there was a substantial increase in the recovery of isolated nuclei, improving from 12,442 to 149,862. This marked improvement underscores the effectiveness of these protocol refinements.

The next optimisation step involved equipment preparation, specifically focusing on the sorter's nozzle, which is responsible for breaking the fluid stream (see section 2.2.1.2 for a detailed explanation). Each nozzle is designed to apply specific pressures based on its diameter. Larger nozzles create larger drops and exhibit lower sheath pressure and lower velocity. One hypothesis tested was that applying higher pressure might detach residual material from the nuclei, thereby purifying them. To test this, two nozzles with diameters of 70 and 100 µm were evaluated. The nuclei present in the sample were counted before and after sorting using the different nozzles, and later the integrity of the nuclei and the accuracy of the counts provided by the sorter were verified using an analyser cytometer. Since this equipment does not have the laser to excite Hoechst, NucRed was used instead, which is excitable at 640 nm. Figure 4.2 displays the dot plots acquired for samples containing 10,000 nuclei (counts obtained from the sorter) that were processed through the 70 and 100 µm nozzles.

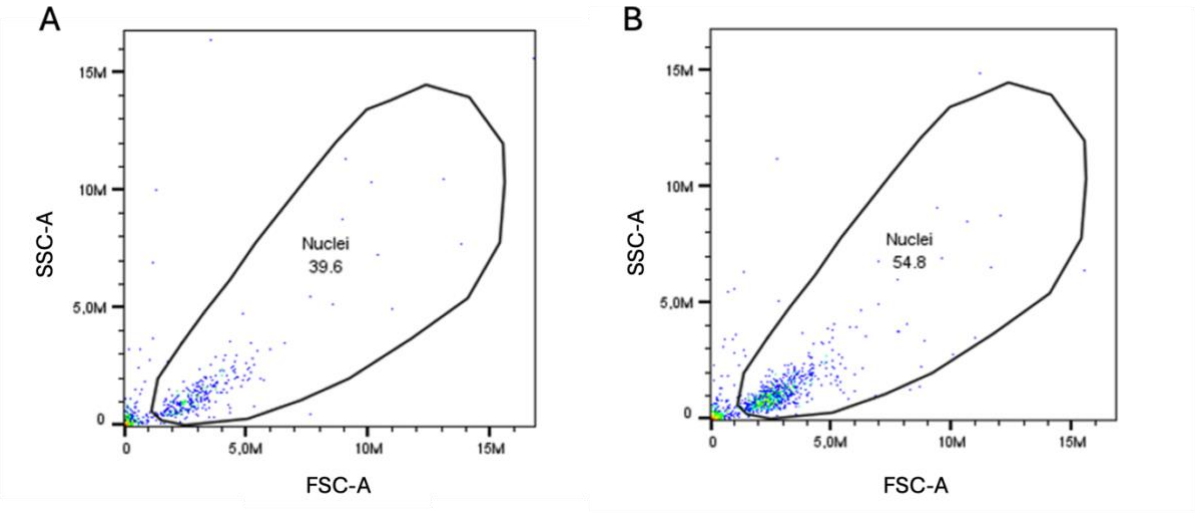

Figure 4.2 – Dot plots obtained using an Accuri cytometer, representing the number of viable nuclei after sorting. The distribution of events is shown according to their size and complexity for samples processed through two different nozzle sizes: **A**) 70 µm nozzle and **B**) 100 µm nozzle. **A**) Only 39.6% of the events in the sample that passed through the 70 µm nozzle are viable nuclei. **B**) In the sample that passed through the 100 µm nozzle, 54.8% of the events are viable nuclei. Results obtained from samples from donor HO-F 271663.

As illustrated in Figure 4.2, only 39.6% of the 10,000 events from the sample processed through the 70 µm nozzle are intact nuclei, with the remainder being debris. In contrast, for the sample processed through the 100 µm nozzle, 54.8% of the events are viable nuclei. Although these results are not optimal, the 100 µm nozzle appears to be the better option for recovering more nuclei. This difference can be attributed to the fact that the 70 µm nozzle applies higher pressure, which can be excessively harsh on the nuclei. Additionally, because it is smaller, the sorting process is faster, causing the nuclei to reach the collection tube and buffer at a higher velocity, which likely contributes to greater nuclei damage and an increase in debris.

Given these findings, a question arises: why not use an even larger nozzle? Using a larger nozzle would result in slower sorting, which is significant because running a sample tube requires 1 h and 30 min of sorting when using a 100 µm nozzle. Balancing the time demands, we have determined that the 100 µm nozzle is the most suitable compromise and will be the standard nozzle used moving forward.

The establishment of the nuclei isolation protocol using red fluorescent probes, such as NucRed or DRAQ5, provides greater spectral versatility compared to the traditional use of the blue Hoechst dye. This flexibility allows researchers to combine the protocol with other nuclear or non-nuclear probes across a broader range of wavelengths. Additionally, it offers the possibility of incorporating subsequent probes, particularly in the green or red spectrum, for experiments requiring multiple fluorescent markers. For instance, this adaptability is particularly beneficial when using probes like Laurdan, which shares the same excitation wavelength as Hoechst, making simultaneous use impractical due to signal overlap. By adopting a red probe in the protocol, Laurdan staining can be performed without interference, ensuring clear signal differentiation in complex multi-label experiments. Overall, this protocol's adaptability makes it more versatile and suitable for a wide range of research needs.

In conclusion, the optimal nuclei extraction protocol for isolating nuclei from primary human fibroblasts involves culturing cells until they reach over 80% confluency, detaching them using TrypLE, limiting the setup to only 2 T-flasks per sample tube, and adding a HB. Following the incubation period, the protocol includes performing three freeze/thaw cycles and restoring isotonic conditions by adding a concentrated saline solution. Subsequently, sorting is

performed using a nozzle with a 100 μm diameter. For certain applications, it is advisable to include protease inhibitors in the solutions, such as the HB and the collection tube used during sorting. This is crucial to control protease activity post-lysis, maintain protein concentration, and balance and preserve the biological integrity of the nuclei. In this project, protease inhibitors were added to these solutions to enhance the protocol's effectiveness and versatility.

4.3. Nuclei isolation protocol validation

The efficacy of the optimized method and the quality of the nuclei were assessed using various techniques, including confocal microscopy, AFM, and TEM, as well as by analysing the sorter data looking at different settings.

During the validation process, images were collected at every stage of the protocol, including from adherent cells, cells in suspension, cells after HB, and isolated nuclei. In the case of confocal microscopy, an additional image was acquired after the freeze-thaw cycles but before sorting. Figure 4.3 presents these findings.

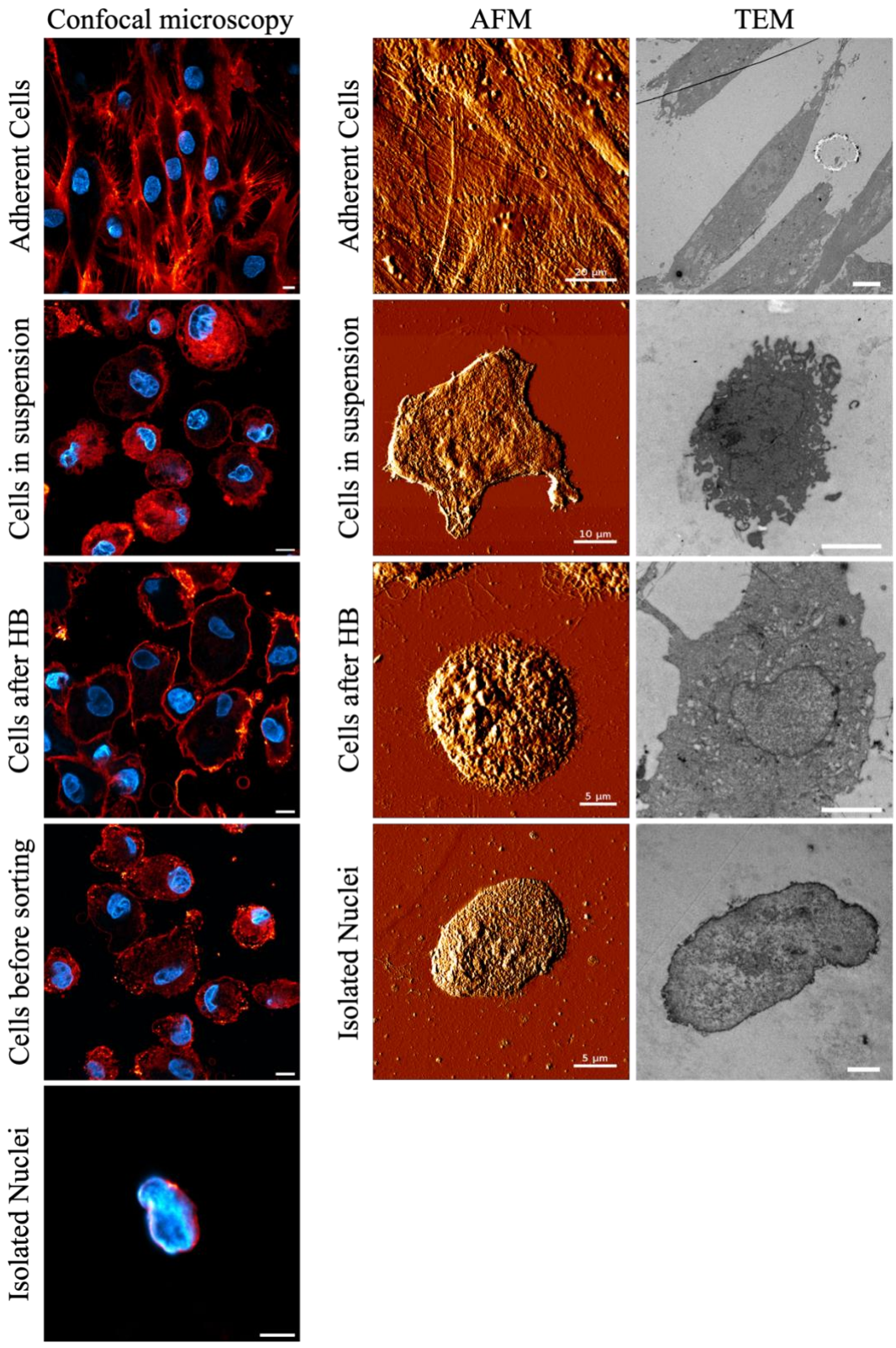

Figure 4.3 – Validation images of various steps of the isolation protocol using confocal microscopy, AFM, and TEM. In the confocal images, CellMask (red) labels membranes (excited at 561 nm and emission detected between 571-750 nm), while Hoechst (blue) stains DNA (excited at 405 nm and emission detected between 415-478 nm). These images illustrate different cellular stages throughout the isolation protocol, beginning with an

intact plasma membrane, progressing to a compromised membrane, and finally showing completely isolated nuclei, free from membrane remnants or ER contamination. Regarding the confocal images the scale bar is 10 μm, except for the isolated nuclei, where it is 5 μm. Additionally, error signal images obtained using AFM in contact mode confirm successful nuclei isolation, accompanied by TEM images. The scale bars in the TEM images are as follows: 10 μm for adherent cells, 5 μm for cells in suspension and after treatment with HB, and 2 μm for isolated nuclei. Results obtained from samples from donor HO-F 271663

As shown in Figure 4.3, the protocol effectively isolates nuclei from cultured primary fibroblasts. Typically, fibroblasts in culture exhibit a striated morphology. When adhered to a surface, these cells undergo elongation, a characteristic behaviour as they seek contact with neighbouring cells, reflecting their inherent tendency to grow close and form a monolayer (Figure 4.3). In contrast, when fibroblasts are placed in suspension, they lose this elongated phenotype and adopt a more rounded morphology.

Upon treatment with a HB is perceptible in Figure 4.3 that the osmotic imbalance drives water into the cells, resulting in noticeable swelling and an increase in cell size. This phenomenon is crucial, as it facilitates subsequent steps in the isolation process. The confocal microscopy images in Figure 4.3 further illustrate the impact of the freeze-thaw cycles, which lead to the rupture of the cell membrane. This rupture is a critical step in ensuring the release of intact nuclei from the cells.

The final stage of the protocol, involving cell sorting, proves to be highly effective in purifying the nuclei. As observed, the isolated nuclei exhibit minimal contamination from other cellular organelles with the red probe exclusively labelling the nuclear membrane, confirming the efficiency of the sorting process in removing residual membrane fragments (Figure 4.3). This step is essential to ensure that the nuclei are free from extraneous materials, which is critical for downstream applications. AFM and TEM, with their higher resolution, confirmed that the nuclei were successfully isolated.

Other analyses were conducted specifically with the sorting data. To see if it would be possible to effectively isolate the nuclei taking into account their size (forward scatter) or their complexity (side scatter), excluding the fluorescence (Hoechst), we concatenated the data of cells in suspension, cells after HB and the nuclei in different plots. Figure 4.4 represents 3 dot plot graphs of the sorter data organised by forward scatter, side scatter and fluorescence of the three states of the samples.

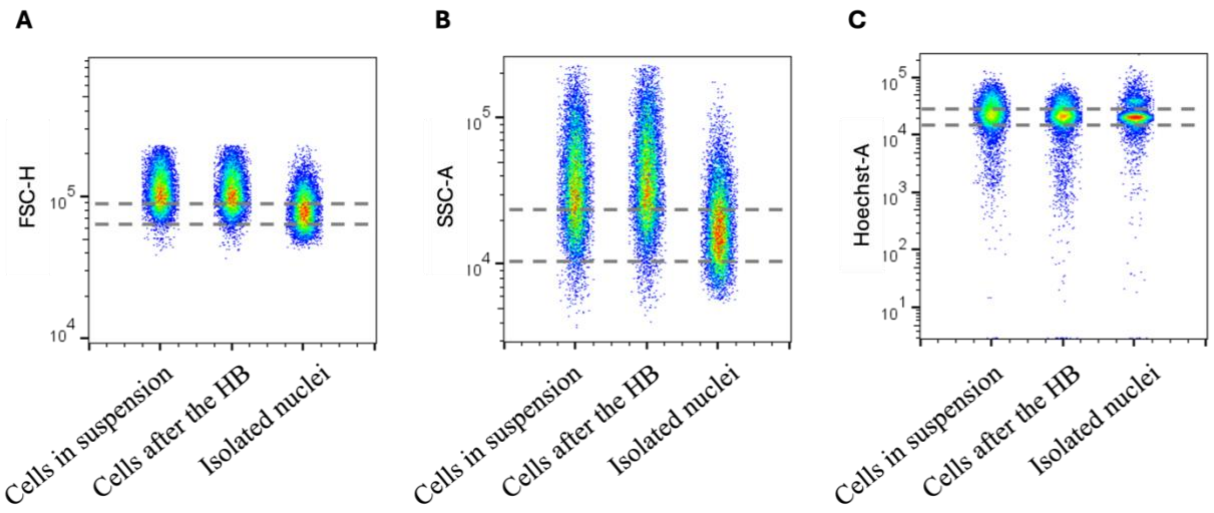

Figure 4.4 – Concatenated dot plot graphs of cells in suspension, after treatment with hypotonic buffer (HB), and isolated nuclei, illustrating differences in size (A), complexity (B), and fluorescence (C). The dot plot graphs show the sample at three different stages of the nuclei isolation protocol, demonstrating that: **A**) the nuclei are smaller than the events in other stages; **B**) they are less complex; and **C**) they maintain fluorescence throughout the isolation protocol. This data indicates that nuclei can be sorted based on characteristics other than fluorescence alone. Results obtained from samples from donor HO-F 271663

From Figure 4.4, it can be concluded that the nuclei are indeed distinguishable from the cells in suspension, and post-HB treatment based on their size and complexity. The high-density area (in red) in the column of the isolated nuclei separated from the others, *i.e.* at a smaller FSC and SSC range of cells in suspension, and post-HB-treated cells, further confirms this distinction (Figure 4.4A and B). This separation allows for the effective combination of forward and side scatter parameters to select the population of interest without the need for staining.

Regarding the plot displaying the three states of the sample grouped by fluorescence (Figure 4.4C), it is expected that all of them exhibit similar intensity values. Although the samples differ in their treatment stages, the staining process was performed uniformly across all samples when the cells were still in culture. Since the staining specifically targets the nuclei, the consistent fluorescence intensity values across the three samples confirm uniform staining with minimal nonspecific labelling. Nevertheless, staining provides an extra layer of validation, confirming that what is being sorted are indeed nuclei. For downstream applications, it can be advantageous to have the nuclei already labelled, thus saving additional staining steps.

After confirming the efficacy of nuclei isolation with minimal contamination from other organelles, the next step was to evaluate whether the process, while effective in removing other membranes and organelles, affected nuclear membrane integrity. To assess this, TEM images

at higher magnification were examined to determine if the NE was compromised (Figure 4.5). These images were then compared to the nuclear membrane in intact cells to identify any potential changes, even if the membrane remained uncompromised.

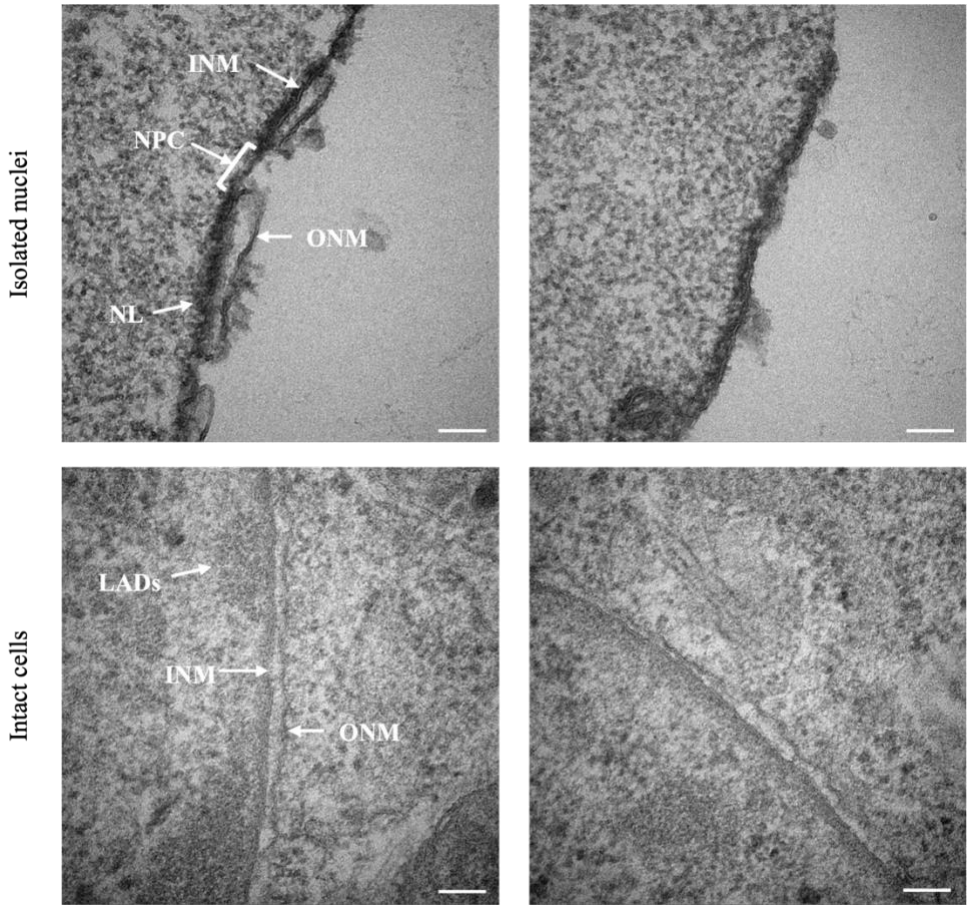

Figure 4.5 – TEM images of the NE in intact cells and isolated nuclei. The NE remains intact, with clear definition of the nuclear pore complex (NPC), nuclear lamina (NL), inner nuclear membrane (INM), and outer nuclear membrane (ONM). When compared to the NE in intact cells, no major differences are observed. Scale bar: 100 nm. Results obtained from samples from donor HO-F 271663

Figure 4.5 demonstrates that the developed nuclei isolation protocol successfully preserves the integrity of the nuclear membrane. Throughout the entire isolation process, key structural components, including the INM, ONM, nuclear lamina, and NPC, remain intact and clearly identifiable. This indicates that the protocol is effective in isolating nuclei without compromising the NE's structural integrity. When isolated nuclei are compared with the nuclei of intact cells, it is evident that the nuclear membrane does not undergo any significant conformational changes. In both cases, the nuclear membranes appear remarkably similar, despite pertaining to completely different sample conditions. This consistency in nuclear

membrane structure suggests that the isolation process is gentle enough to maintain the native architecture of the nucleus while effectively removing other cellular components.

Furthermore, the preservation of key nuclear features, such as the NPC and nuclear lamina, is crucial for subsequent analyses that require intact nuclear structures. The ability to maintain these structures intact through the isolation protocol validates its use for experiments that depend on the accurate representation of nuclear components. Overall, the results depicted in Figure 4.5 confirm that the protocol is effective and non-disruptive to the nuclear membrane, reinforcing the reliability of the method for further downstream applications.

However, this nuclei isolation method has its limitations. One significant drawback is the lack of reproducibility across samples, meaning that the sample in terms of nuclei purity and number is not always uniform. Similar to other detergent-free nuclei isolation protocols [119, 120], this method does not completely eliminate the ER from all nuclei. Since the ER is continuous with the nuclear membrane, obtaining quasi-pure nuclei with minimal ER contamination, especially in the perinuclear region, is common in this and other protocols. Achieving total ER removal typically requires the use of detergents [120]. Nevertheless, as discussed in Section 1.6, the primary objective of this project is to ensure that nuclear lipids remain undisturbed. The use of detergents in nuclei isolation can lead to misinterpretations, as even at low concentrations, detergents can remove lipids from the NE in a non-homogeneous manner, altering its composition and compromising the integrity of the membrane. Therefore, it is crucial that the isolation process remains detergent-free to avoid altering the nuclear lipid composition.

Despite this challenge, striking results were observed during the optimisation of freeze/thaw cycles. Confocal images were taken from samples that underwent three and four cycles, revealing some differences (Figure 4.6).

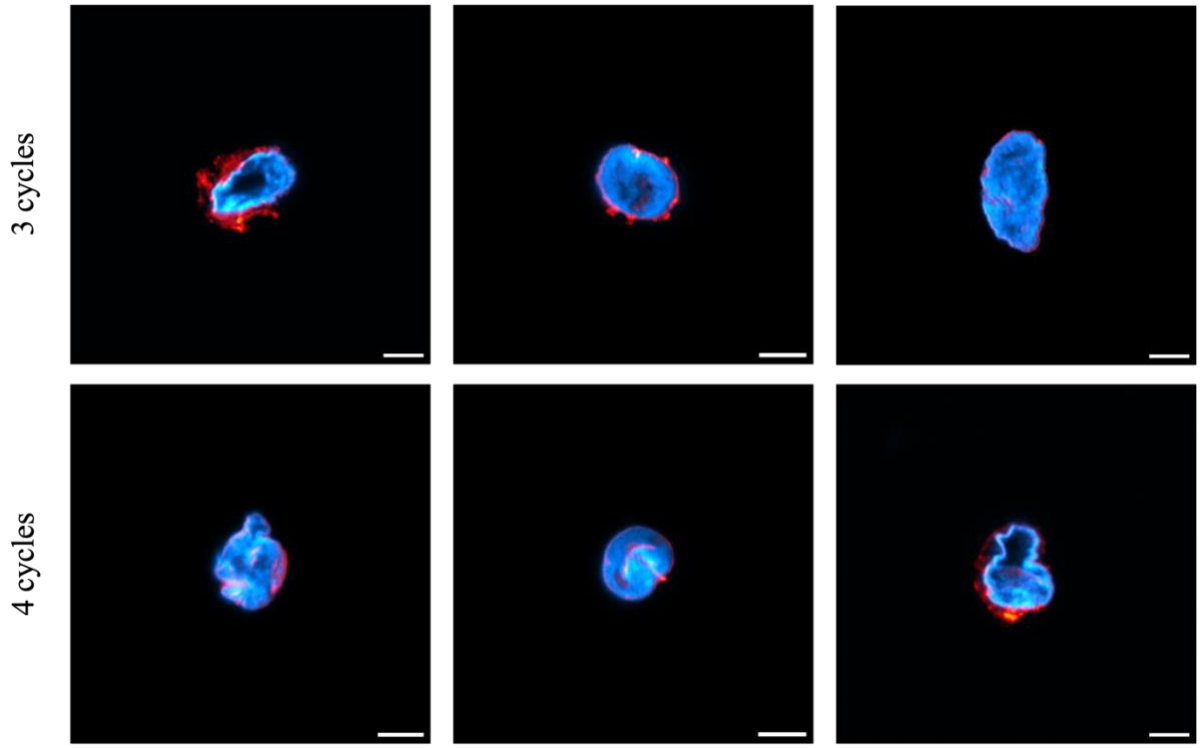

Figure 4.6 – Isolated nuclei after undergoing 3 and 4 freeze/thaw cycles. CellMask (red) labels membranes (excited at 561 nm laser and emission collected between 571-750 nm), while Hoechst (blue) stains DNA (excited at 405 nm laser and emission detected between 415-478 nm). These representative images show that nuclei subjected to 3 freeze/thaw cycles are nearly pure, with some remaining ER attached, while nuclei that underwent 4 cycles show less ER contamination. Scale bar: 10 μm. Results obtained from samples from donor HO-F 271663

The findings from our experiments, as illustrated by the representative images in Figure 4.6, reveal a trade-off between the number of freeze/thaw cycles and the purity of isolated nuclei. Specifically, performing four cycles resulted in a lower recovery of nuclei after sorting (*e.g.*, 123,603 nuclei), but produced nuclei with higher purity. In contrast, performing only three cycles yielded a larger quantity of nuclei (*e.g.*, 833,171 nuclei), but the ratio of pure to quasi-pure nuclei was lower.

This flexibility adds versatility to the protocol, allowing it to be tailored to the specific needs of the study. For example, if the goal is to obtain highly pure nuclei - such as for lipidomics of the NE, where ER contamination must be minimized, or for sequencing analyses focused on nuclear proteins or structures - it would be prudent to perform four cycles to ensure maximum purity. On the other hand, if the study requires techniques like microscopy that allow single-nuclei imaging, where the purest nuclei can be selected to avoid biases from

contamination, it may be more advantageous to prioritize quantity. In this case, performing three cycles would provide a higher number of nuclei, offering more opportunities for detailed analysis.

Ultimately, this trade-off must be carefully considered during project planning, as the choice between purity and quantity will depend on the specific objectives of the study. Balancing these factors is key to optimizing the protocol for different experimental needs.

Although alternative detergent-free protocols for nuclei isolation exist, the protocol described herein represents a significant advancement by employing cell sorting principles to facilitate nuclei isolation. When compared to other methods, especially those without detergents, this protocol offers improved nuclei quality, preserving membrane integrity and yielding quasi-pure nuclei. In a laboratory where a sorter is available, this approach enhances affordability and simplifies the procedure, as the majority of the labour-intensive processes are performed by the equipment.

In conclusion, the developed nuclei isolation protocol demonstrates significant efficacy in producing high-quality nuclei with minimal contamination from other cellular components. The combination of confocal microscopy, AFM, TEM, and nuclei sorting data analysis provided a comprehensive validation of the protocol across different steps, from cultured cells to isolated nuclei. While the protocol effectively preserves the structural integrity of the nuclear membrane and maintains essential nuclear features, it also presents some limitations, particularly regarding sample reproducibility and the presence of residual ER contamination. However, the adaptability of the protocol, especially in terms of adjusting freeze/thaw cycles to balance purity and yield, offers flexibility to tailor the procedure to specific experimental needs. Ultimately, the choice of parameters should be guided by the goals of the study, whether it prioritizes nuclear purity or a high number of recovered nuclei. The findings underscore the protocol's reliability and versatility, making it a valuable tool for various downstream applications in nuclear research.

4.4. Lamin A distribution in isolated nuclei

Following the establishment of a nuclei isolation protocol, the subsequent phase involved investigating the properties of nuclei in relation to ageing. As previously noted, LA is intimately associated with diseases termed laminopathies, which are characterised by symptoms of premature ageing. This thesis delineates in section 1.3.2 that LA is dysregulated

during normal ageing as well, impacting nuclear integrity and gene stability through increased sequestration of this protein or its precursor form (preLA) to the nuclear periphery.

To explore this phenomenon further, nuclei isolated from four young donors, three elderly donors, and one patient diagnosed with HGPS were subjected to an immunocytochemistry protocol to label LA (Figure 4.7). The objective was to ascertain whether a quantifiable relationship, expressed as the periphery/nucleoplasm ratio of LA concentration, exists and to determine the extent to which ageing influences this ratio. In the case of nuclei from HGPS patients, since every cell carries the mutation in the *LMNA* gene, the nuclei do not express LA but rather progerin (as discussed in section 1.3.2). However, the antibody used to label LA shares the same epitope with Lamin C, thus marking both LA and Lamin C. This explains why the nuclei from HGPS patients still show staining, despite the absence of LA.

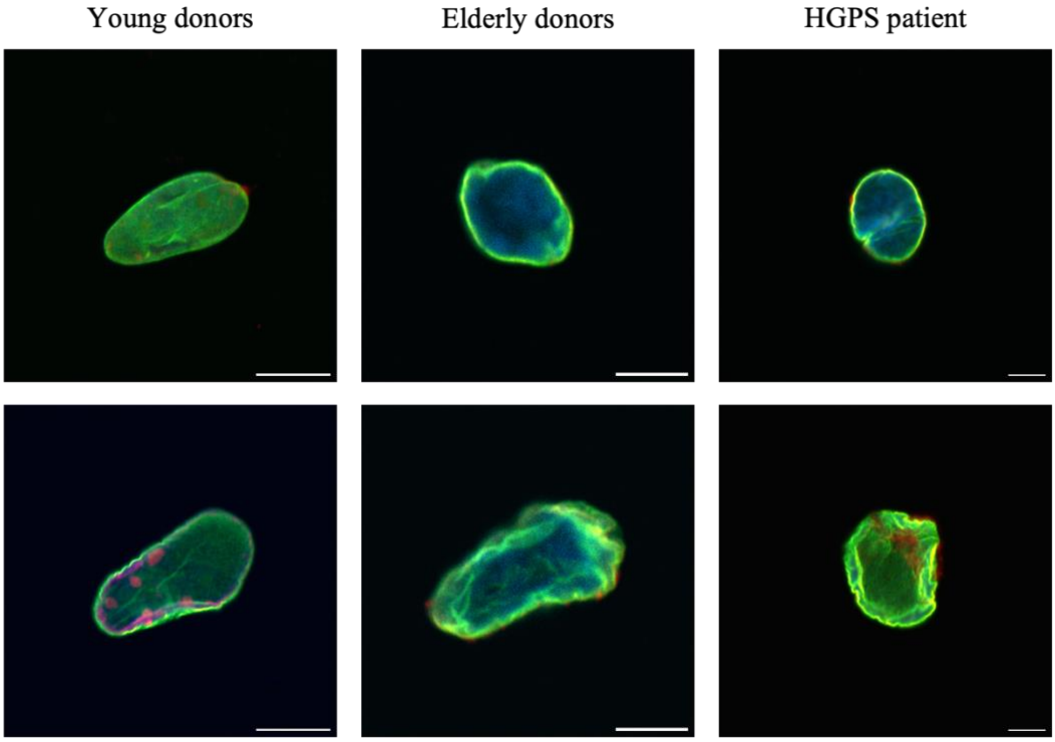

Figure 4.7 – Confocal microscopy of isolated nuclei with labelled Lamin A. CellMask (red) labels membranes (excited with a 561 nm laser and detected between 571-750 nm), Hoechst (blue) stains DNA (excited with a 405 nm laser and detected between 415-478 nm), and mouse monoclonal lamin A/C antibody coupled with Alexa Fluor 488-conjugated goat anti-mouse IgG (green) labels Lamin A/C (excited with a 488 nm Argon laser and detected between 498-550 nm). These representative images show the distribution of Lamin A across the nucleus in samples from young donors, elderly donors, and in the case of the patient with HGPS Lamin C. Young donor nuclei: top - HY-M GM05659M; bottom - HY-F GM00969I. Elderly donor nuclei: top - HO-M 273074; bottom - HO-F 274516. HGPS-F patient AG08466 nuclei. Scale bar: 10 μm.

However, the results obtained did not align with expectations. For nuclei such as those depicted in the lower panel of Figure 4.7, defining the nuclear periphery was challenging. The initial strategy to use Fiji software to obtain intensity values of the nuclear periphery and nucleoplasm, and subsequently calculate their ratio was quickly deemed impractical. This approach was intended to identify regions of LA accumulation, as higher intensity values correlate with greater protein concentration. As an example, Figure 4.8 displays the nuclei and their corresponding histograms of intensity values for elderly donors.

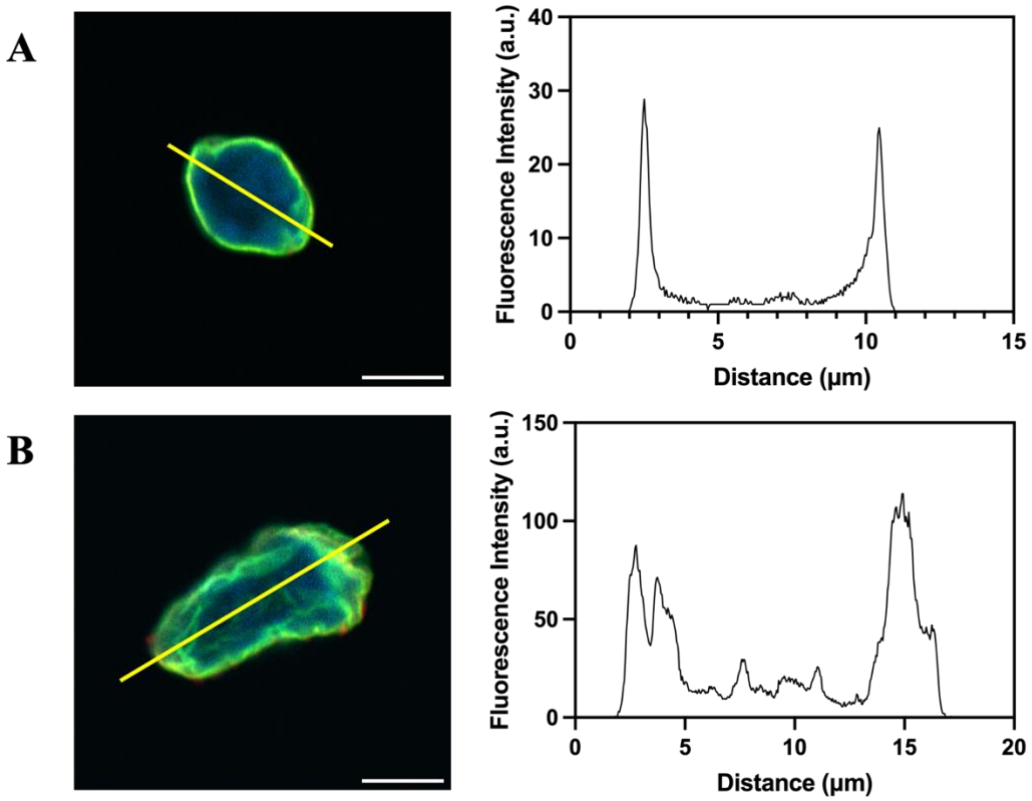

Figure 4.8 – Challenges in defining the nuclear periphery in confocal images. CellMask (red) labels membranes, Hoechst (blue) stains DNA, and mouse monoclonal lamin A/C antibody coupled with Alexa Fluor 488-conjugated goat anti-mouse IgG (green) labels Lamin A/C. **A:** representative confocal image where the periphery/nucleoplasm Lamin A (green) ratio can be assessed, showing well-defined peaks and a distinguishable nuclear periphery as can be seen by the histogram corresponding to LA signal. **B:** representative confocal image of a nucleus where the nuclear periphery is not clearly perceptible due to background noise or insufficient resolution, as confirmed by the corresponding fluorescence intensity histogram of LA signal obtained by the cross section present in the confocal images. Nuclei from Elderly donor: top - HO-M 273074; bottom - HO-F 274516. Scale bar: 10 μm.

According to Figure 4.8A, drawing a line through the depicted nuclei to generate a histogram of intensity values facilitates the calculation of the aforementioned periphery/nucleoplasm ratio, owing to the presence of two distinct and well-defined peaks.

Consequently, it is possible to calculate the mean intensity of these peaks to determine the intensity of the signal at the periphery, and similarly for the nucleoplasm by averaging the values between the two peaks. Conversely, as shown in Figure 4.8B, distinguishing between the periphery and other regions becomes problematic, as evidenced by the histogram's lack of distinct peaks. This ambiguity may be attributed to the formation of invaginations caused by LA accumulation at the periphery or possibly to the limitations of confocal microscopy, which may not offer sufficient resolution to clearly delineate the nuclear membrane, potentially confusing actual signals with background noise. Calculating the ratio using histograms like those in Figure 4.8B would likely introduce significant bias, as it is indiscernible which peak should be considered, and averaging could inadvertently mix nucleoplasmic and peripheral signals.

Given these considerations, the approach to quantify LA distribution between the periphery and the nucleoplasm was ultimately abandoned. To accurately assess and define these regions, advanced imaging techniques such as stimulated emission depletion (STED) and expansion microscopy, or novel analytical approaches such as super-resolution radial fluctuations (SRRF), would be necessary. By employing these techniques to obtain higher-resolution images, future research could more precisely delineate and quantify LA distribution, providing clearer insights into its alteration with ageing.

However, the images acquired allowed us to conduct alternative analyses. In this case, we utilized the confocal images to calculate the aspect ratio of the nuclei using Fiji, aiming to gather morphological information about nuclei at various stages of ageing and disease (Figure 4.9).

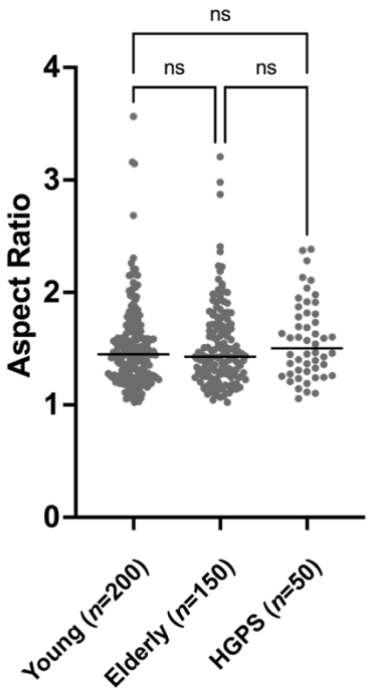

Figure 4.9 – Aspect Ratio values of nuclei from young donors, elderly donors, and a patient with HGPS. The distribution of aspect ratio values shows a mean of 1.516 for young donors, 1.525 for elderly donors, and 1.573 for the patient. Since these values are not close to 1, the nuclei are classified as less round. The p-value from Tukey's multiple comparisons test indicates no statistically significant difference ($p > 0.05$). *n* represents the number of nuclei studied at each condition. In young condition, nuclei from HY-F GM00041G and GM00969I and HY-M GM05659M and GM00498G were used. For the elderly were used nuclei from HO-M 273074 and HO-F 274516 and 284401. The patient used was the HGPS-F AG08466. The analysis was conducted using Fiji.

Figure 4.9 indicates no significant differences in the morphology of nuclei across the three conditions studied, suggesting that using the aspect ratio may not effectively capture morphological variations. An alternative analysis, such as counting the blebs or invaginations in each nucleus, could be conducted. However, without a clear definition of the nuclear periphery, this approach risks introducing significant biases into the results.

In conclusion, despite the faced methodological challenges, particularly with defining nuclear peripheries, the data collected provide a foundational understanding that underscores the need for enhanced imaging resolution and more advanced analytical techniques. Future studies should integrate advanced methodologies such as STED microscopy, SRRF, and expansion microscopy to overcome these obstacles. Employing these techniques will be crucial for accurately characterizing nuclear architecture and potentially unveiling new insights into the distribution of LA across the nucleus, which may help explain age-related nuclear alterations.

4.1. Nuclear stiffness assessment by Force Spectroscopy

The exploration of biomechanical and biophysical characteristics of the nucleus during human aging began by assessing nuclear stiffness under different conditions (Figure 4.10).

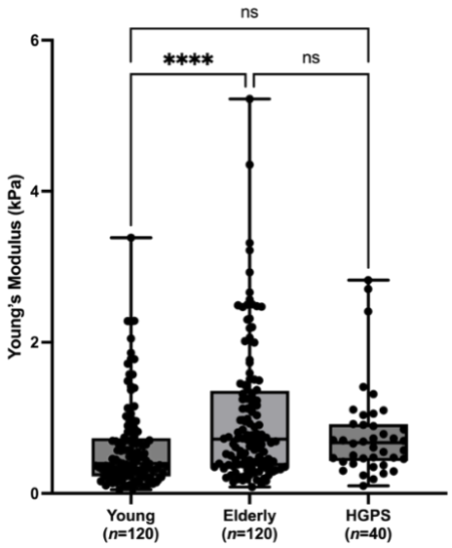

Figure 4.10 – Young's Modulus values of nuclei from young donors, elderly donors, and a patient with HGPS. The statistical test used for the analysis was Tukey's multiple comparisons test. Nuclei from elderly donors were found to be stiffer compared to those from young donors (****p-value < 0.0001). However, no statistically significant difference was observed between young donors and the patient, or between the patient and elderly donors (p-values > 0.05), likely due to the low number of patient nuclei analysed. The increased stiffness of nuclei from elderly donors supports the hypothesis that the sequestration of LA to the nuclear periphery during ageing alters nuclear biomechanical properties. These results were obtained using AFM-based force spectroscopy in liquid, with an MSLN-10 D tip. Force curves were analysed using JPK analysis software. *n* represents the number of nuclei studied in each condition. In young condition, nuclei from HY-F GM00041G and HY-M GM05659M and GM00498G were used. For the elderly were used nuclei from HO-M 273074 and HO-F 274516 and 284401. The patient used was the HGPS-F AG08466.

Figure 4.10 highlights the substantial biological variability typically observed in studies using biological specimens. Notably, within each donor group, variability is significant, with measurements ranging from 0.500 kPa to over 5 kPa among older donors. Nevertheless, these values fall within the reported range of 1-5 kPa, as these measurements are highly influenced by factors such as the stage of the cell cycle, the position of the AFM tip, and the surroundings of the point where the force curve is being acquired [146, 147]. Furthermore, a statistical analysis of the data confirms a significant difference between the younger and older groups, lending robust support to our hypothesis. Despite the inability to directly quantify the nuclear distribution of Lamin A, the findings convincingly demonstrate that nuclei from older donors exhibit greater stiffness (higher Young's Modulus values) compared to those from younger donors. Considering that LA significantly contributes to nuclear rigidity (see section 1.3.2), and that force spectroscopy is used for measuring membrane elasticity, it is reasonable to infer that the observed increase in nuclear stiffness with age may be attributed to the redistribution of LA to the periphery. Unfortunately, limitations in sample diversity, as previously discussed, with only one patient donor available for study, constrain these conclusions. The similarity in mean stiffness values between this patient and the older donors suggests that expanding the patient sample might differentiate the patient group from the young donors while showing alignment with the older group. Such data would not only validate our initial hypothesis that LA is sequestered to the nuclear periphery during ageing but also highlight the established connection between the mutant form of LA and increased nuclear stiffness.

4.2. Membrane tension study using Fluorescence Lifetime Imaging Microscopy

In order to quantify the changes in nuclear membrane tension with ageing, we utilised FLIM with the membrane tension-sensitive probe Flipper-TR. The fluorescence lifetime (τ) of Flipper-TR, which varies in response to membrane tension, was measured in the nuclei of both young and elderly donors. In this study, the fluorescence decay data were fitted using a double-exponential model, yielding two lifetime components, τ_1 and τ_2. Due to the low photon count associated with the shorter lifetime component (τ_1), which contributes only a small fraction of the total signal, this value is more susceptible to error. Therefore, Figure 4.11 is based on the longer lifetime component, τ_2, which provides a more reliable representation of membrane tension. Figure 4.11 presents a comparison of τ_2 values between the two groups.

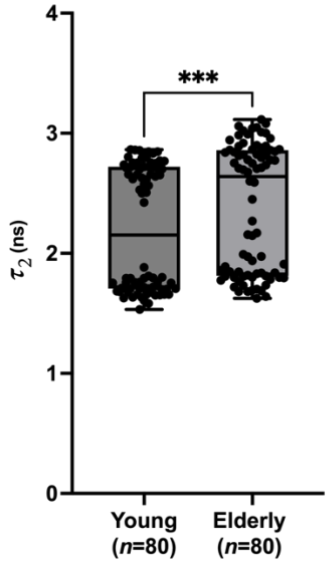

Figure 4.11 – Fluorescence lifetime (τ_2) values of nuclei from young and elderly donors. The box plot illustrates the distribution $\boldsymbol{\tau_2}$ measured using the membrane tension-sensitive probe Flipper-TR. The probe was excited with a multiphoton Titanium laser set at 800 nm, with emission collected in the 500–680 nm range. The statistical test used was the Mann-Whitney test, which shows that nuclei from elderly donors exhibit significantly higher $\boldsymbol{\tau_2}$ values compared to those from young donors (***$p < 0.05$), suggesting increased membrane tension in the nuclear envelope. *n* represents the number of nuclei analysed for each condition. In young condition, nuclei from HY-F GM00969I and HY-M GM00498G were used. For the elderly were used nuclei from HO-M 273074 and HO-F 274516.

Moreover, Figure 4.11 displays a clear variation in fluorescence lifetime values among different donors within the same study group, showing up as distinct populations within each age group. This variation suggests that the measurement is highly donor-dependent, indicating the influence of individual biological factors on membrane properties. Consequently, further

research is needed to determine the broader trends in lifetime values across a larger cohort to establish more definitive group tendencies.

Despite this inter-donor variability, a consistent pattern emerges: elderly donors exhibit significantly higher fluorescence lifetimes compared to young donors. The Flipper-TR probe, a mechanosensitive fluorophore, detects this difference by responding to changes in membrane tension. Under conditions of higher membrane tension, the lipid bilayer becomes more tightly packed, forcing the probe's aromatic rings (flippers) into alignment. This alignment results in a planar, conjugated structure, thereby increasing the fluorescence lifetime. Conversely, under lower membrane tension, where lipid packing is less dense, the probe's flippers remain twisted out of conjugation due to steric repulsion, leading to a reduced fluorescence lifetime [148].

Lipid packing, which reflects the density and organization of lipid acyl chains, plays a key role in determining membrane dynamics. Tighter, more ordered acyl chains correspond to higher lipid packing, typically seen in liquid-ordered membrane phases. In contrast, lower lipid packing is associated with more disordered acyl chains, characteristic of liquid-disordered phases. The Flipper-TR probe effectively distinguishes between these phases, as the increased pressure from more ordered lipid packing leads to greater planarization of the probe, resulting in higher fluorescence lifetimes [148].

The significantly higher lifetimes observed in elderly donors suggest an increase in membrane tension and lipid order in their nuclear membranes compared to young donors. The results highlight the importance of membrane tension as a biomarker for ageing-related changes in nuclear membrane properties.

4.3. Nuclear membrane order analysis by Di-4-ANEPPDHQ GP measurements

The degree of lipid packing offers a way to visualise membrane order, as efficient packing of lipids leads to the exclusion of water molecules from the typically nonpolar bilayer. This exclusion alters the local environmental polarity, which can be detected using polarity-sensitive fluorescent probes like Di-4-ANEPPDHQ. These probes allow for the calculation of GP, providing a quantitative measure of changes in membrane polarity. Consequently, higher GP values indicate a more ordered membrane structure, as they reflect lower polarity in the membrane environment. This reduced polarity corresponds to lipid heads being more tightly packed, leading to decreased mobility [141].

In this study, we examined the membrane order of nuclei from 1 young donor, 2 elderly donors, and the patient with HGPS using GP imaging of Di-4-ANEPPDHQ-labelled nuclei.

We initially attempted to use Laurdan, given its established use in assessing membrane order. However, several challenges arose during the staining process, particularly when targeting the nuclear membrane. Laurdan staining worked effectively in the plasma membrane but failed to produce consistent results in the nuclear membrane. One potential cause is that the nuclear membrane has a significantly higher protein-to-lipid ratio compared to the plasma membrane. This abundance of proteins may block Laurdan from embedding within the nuclear lipid bilayer. The changes in the membrane environment around the nucleus, particularly its interactions with the nuclear lamina and chromatin, could make the staining process more challenging.

The challenges with Laurdan staining, combined with additional issues related to equipment limitations and spectral overlap, led us to seek alternatives. Specifically, while Laurdan staining posed its own difficulties, the need for multi-photon excitation microscopy would have further complicated the process since the desired equipment is not available at the home institute, making confocal microscopy a more practical option. Moreover, the overlap between Laurdan's excitation and emission spectra with Hoechst added another layer of complexity, as it necessitated the use of red nuclear stains to avoid signal interference. These combined factors prompted us to switch to Di-4-ANEPPDHQ, a dye that offered a more straightforward staining protocol and was compatible with standard microscopy using an Argon laser at 488 nm. This transition improved staining reproducibility and simplified the experimental workflow, allowing for nuclear isolation using only Hoechst, which reduced both the complexity and labour of the process. Figure 4.12 presents the GP values obtained to assess membrane order.

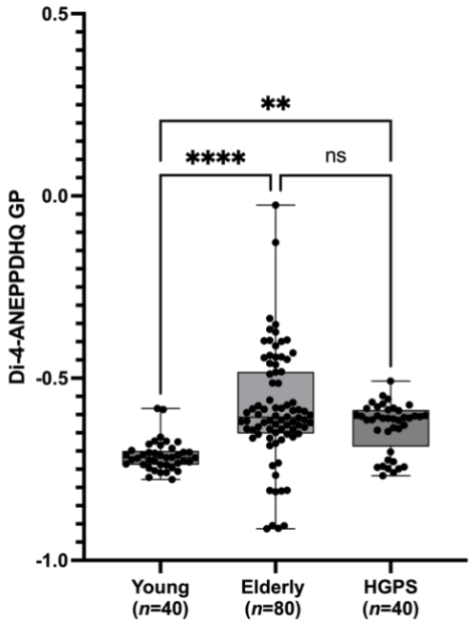

Figure 4.12 - Generalized Polarization values for nuclei from young donors, elderly donors, and a patient with HGPS. The statistical test used for the analysis was Tukey's multiple comparisons test. The plot shows that nuclei from elderly donors have significantly different GP values compared to those from young donors (****p < 0.0001). Additionally, there is a significant difference between GP values of young donors and HGPS patient nuclei (**p < 0.01). No significant difference (ns) is observed between the HGPS patient and old donor nuclei. These results suggest that membranes from elderly nuclei are more ordered, with increased lipid packing, compared to nuclei from young donors. GP values were calculated according to Equation 2 (section 3.5.3), and the images were analysed using Fiji. *n* represents the number of nuclei studied in each condition. In young condition, nuclei from HY-M GM05659M were used. For the elderly were used nuclei from HO-M 273074 and HO-F 274516. The patient used was the HGPS-F AG08466.

The results shown in Figure 4.12 revealed a statistically significant difference in membrane order between the young donor and both the elderly donors and the HGPS patient. However, no significant difference was observed between the elderly donors and the HGPS patient, suggesting that membrane order in old donors closely resembles that of HGPS patients. Specifically, the GP values for the young donors ranged from approximately -0.586 to -0.778, indicating relatively lower membrane order and thus higher membrane fluidity. This finding is consistent with the notion that younger cells typically exhibit more fluid and dynamic membranes, which could be attributed to a lower concentration of membrane-stabilizing components such as cholesterol and saturated lipids [149, 150]. In contrast, the GP values for the elderly donors spanned a broader range, from -0.025 to -0.912, with higher average values compared to the young donor group. This suggests an increase in membrane order with age, something anticipated with the results obtained with the lifetime data. Such a trend may be associated with the accumulation of raft-like domains or other ordered lipid nanodomains in the nuclear membrane, which contribute to the observed decrease in membrane fluidity in aged cells [150, 151]. Similarly, the GP values for the HGPS patient fell within a range of -0.442 to -0.768, closely mirroring the values observed in the elderly donors. The observed similarity in membrane order between HGPS patients and elderly donors, alongside consistent findings in other membrane properties (membrane elasticity), suggests that HGPS shares significant characteristics with the normal ageing process, particularly in relation to nuclear membrane properties.

These changes in membrane order could have significant functional implications, potentially reducing the flexibility of the NE and affecting the cell's ability to respond to mechanical stress, thereby altering key functions within the cell. While these findings provide valuable insights into the membrane order of nuclei across different age groups and disease states, the study is limited by the sample size, particularly with only one HGPS patient and one

young donor. Future research should aim to expand the sample size, to further refine these observations and clarify the relationship between accelerated ageing syndromes and natural ageing at the membrane level. Additionally, further studies should explore the biochemical changes underlying the observed differences in membrane order, such as lipidomic analyses and detailed mapping of nuclear membrane-associated proteins, to better understand the mechanisms driving these alterations and to identify potential therapeutic targets for mitigating the effects of ageing and age-related diseases.

4.4. Development of *in vitro* aged-tuned models – Ongoing work

In vitro models are extensively utilized to investigate membrane properties due to their simplicity, homogeneity, and scalability compared to biological samples. These models can be produced on a larger scale by adjusting lipid concentration. The field of synthetic biology has advanced rapidly, particularly in membrane studies, which are crucial for various applications, including drug development, artificial cell creation, and the ultimate goal of developing *in vitro* organs.

In the later stages of this project, the focus shifted to the development of vesicles using lipids extracted from isolated nuclei, employing a bottom-up approach. The initial step involved the creation of liposomes, with the aim of developing age-tuned vesicles and studying specific membrane properties. However, this approach faced several challenges. A major limitation was the timing of the experiments, as only lipids from an older donor were available for analysis.

The objective of this experiment was to examine the membrane properties of these vesicles to determine if they replicated the characteristics observed in the nuclei. By using vesicles, we aimed to isolate the specific effects of lipids from those of other biomolecules present in the NE, such as proteins. This approach allows us to better understand how lipids alone contribute to membrane dynamics and properties, without the confounding influence of other nuclear components. The plan was to begin by assessing the membrane order of vesicles formed from extracted lipids using Laurdan fluorescence spectroscopy. Accurate lipid concentration measurements were critical to ensure the appropriate amount of Laurdan probe was added, as excess probe could interfere with membrane properties and skew the results. However, determining lipid concentration would have required using a portion of the sample for quantification, leaving insufficient material for vesicle formation.

To address this issue, an alternative strategy using flow cytometry was explored. Flow cytometry has evolved significantly in recent years, enabling the examination of previously inaccessible structures, such as extracellular vesicles. In this project, a cytometer capable of detecting vesicles as small as 70 nm was used, resorting to Enhanced Small Particle Detection (see section 2.2.1.3). This approach not only allows for the visualization of vesicles but also enables the correlation between the number of vesicles and the initial lipid concentration.

To evaluate the detection of LUVs, vesicles were formed from synthetic lipids with a known concentration. Initially, unstained and Rhod-DOPE-stained POPC vesicles at a final lipid concentration of 0.5 mM were used, with a probe-to-lipid ratio of 1:500, with seven different dilutions prepared according to the recommendations provided by the manufacturer of the equipment used for sample analysis. The first attempt was unsuccessful due to insufficient dilution, resulting in a swarm effect, where multiple particles pass through the laser simultaneously, impending single-particle detection.

In a subsequent attempt, the sample was diluted 1,000-fold, followed by serial dilutions at a 1:3 ratio, ultimately reaching a 72,900-fold dilution (Figure 4.13).

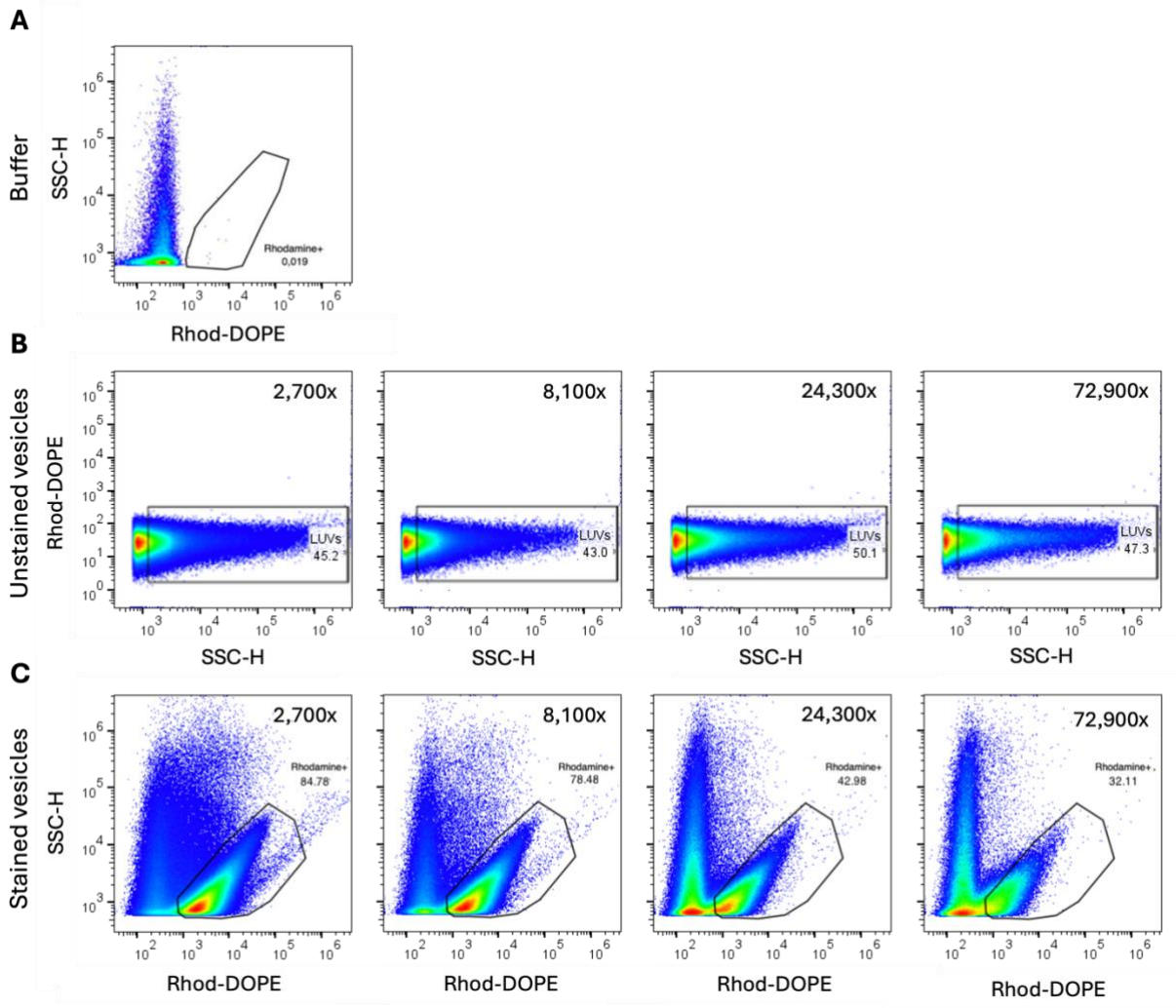

Figure 4.13 – Enhanced Small Particles Detection of (A) the buffer used for LUVs formation; (B) POPC LUVs unstained and (C) stained with Rhod-DOPE. The dot plots show: **A)** The buffer alone, highlighting the noise it adds to the measurements; **B)** Unstained vesicles at the four best dilutions, showing no discernible vesicle presence. Since no clear separation of unstained vesicles was observed, their location in the plot was only estimated; and **C)** Stained vesicles (Rhodamine positive (Rhodamine+) vesicles) at the four best dilutions, with clear separation between vesicles and buffer or residues. This demonstrates the improved detection capability when staining is applied.

Figure 4.13 illustrates the difference between unstained and stained vesicles, with the stained vesicles being clearly distinguishable from the background and buffer due to their fluorescence. In contrast, Figure 4.13B shows that it is difficult to differentiate vesicles from other components when using unstained samples. This observation led to the conclusion that LUV detection in this assay requires the use of fluorescent dyes, as unstained vesicles are not easily identifiable.

A critical consideration in this method is determining the appropriate dilution for accurate vesicle counting. To achieve this, the dot plots must be examined to identify the dilution at which there is some presence of buffer, indicating that the sample is diluted enough to avoid the swarm effect but not so diluted that the buffer dominates over the vesicles. The goal is to find a dilution where there is a good correlation between the counts within the selected gate and the expected counts, calculated by dividing the initial event count by the dilution factor.

For example, in Figure 4.13C, the 2,700-fold dilution shows minimal buffer presence (buffer appears near the y-axis, as in Figure 4.13A). At the 8,100-fold dilution, there is more buffer present, and by the 24,300-fold dilution, the buffer presence increases significantly, leading to a drop in vesicle percentage from 78.48% at the 8,100-fold dilution to 42.98%. Furthermore, when comparing expected *versus* actual counts, the results depicted in Figure 4.14 provide crucial insights.

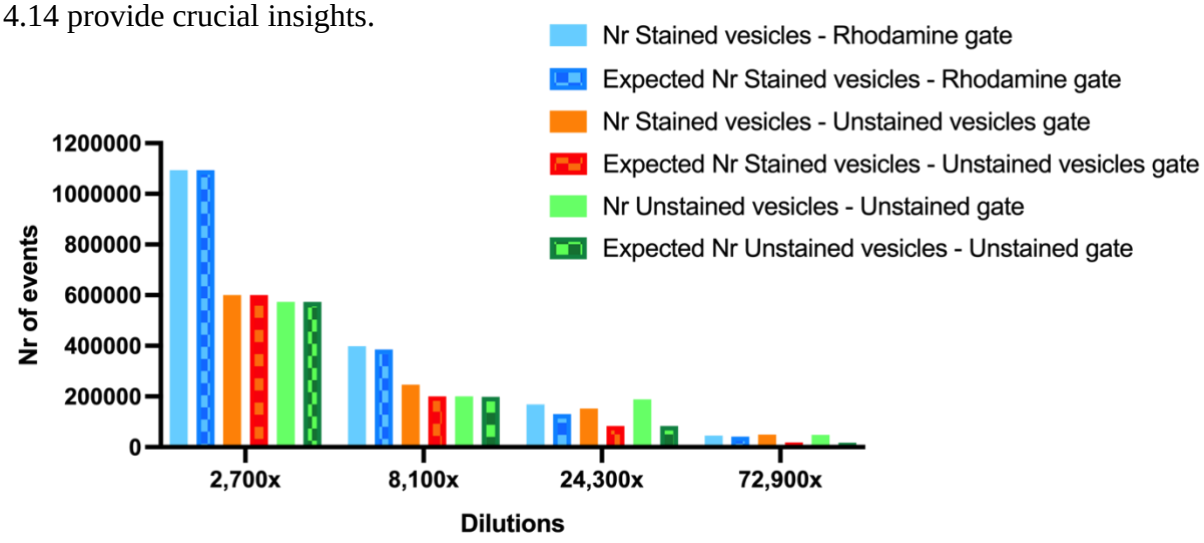

Figure 4.14 – Graphical representation of the number of events detected at different dilutions, using different gating strategies. The filled columns represent the actual event counts at each dilution, while the dashed columns represent the expected values, calculated by dividing the number of events at the initial dilution by the dilution factor. Gating was performed either based on fluorescence signals or by identifying the region where unstained vesicles were expected to appear. The graph shows that the fluorescence-based gating strategy not only detects more vesicles but also aligns more closely with the expected theoretical values (height between the blue filled and dashed columns is much more similar across the dilutions than in the other colours), compared to the gating strategy based on unstained vesicles.

Figure 4.14 demonstrates that gating vesicles based on their fluorescence not only improves their distinction from the buffer, resulting in a higher vesicle count, but also aligns closely with the expected results. This is evidenced by the strong correspondence between the blue filled columns and the patterned blue columns in the graph. The analysis also indicates that the optimal dilution is 8,100-fold, as it offers the best compromise between accuracy and practicality. Although the 2,700-fold dilution shows a nearly equal prediction-to-actual ratio, the 8,100-fold dilution provides a more reliable balance between minimizing background noise and maintaining a high vesicle count.

Following this, a sample of isolated nuclei from the HO-M 273074 was used for lipid extraction, as described in section 3.9. The objective was to establish a correlation between the number of nuclei in the sample and the number of vesicles that could be produced from a given quantity of nuclei. This correlation, along with the previous results, would allow for an estimation of the lipid concentration in the extraction solution. However, a challenge arose: since the vesicles needed to be stained for detection, the lipid concentration of the solution had to be known in order to add the appropriate amount of dye without affecting membrane properties.

To address this, a titration of Rhod-DOPE was performed, and the samples were analysed using cytometry to assess whether properties such as complexity were altered. Given the uncertainty regarding the initial concentration of the sample, fewer dilutions were performed compared to the previous study to avoid the risk of starting with an overly diluted or overly concentrated suspension. The sample was diluted in steps of 10, 25, 50, 75, and 100 times after the initial LUV formation. The results for LUVs formed with the extracted lipids and Rhod-DOPE at the final concentration of 2 μM are presented in Figure 4.15.

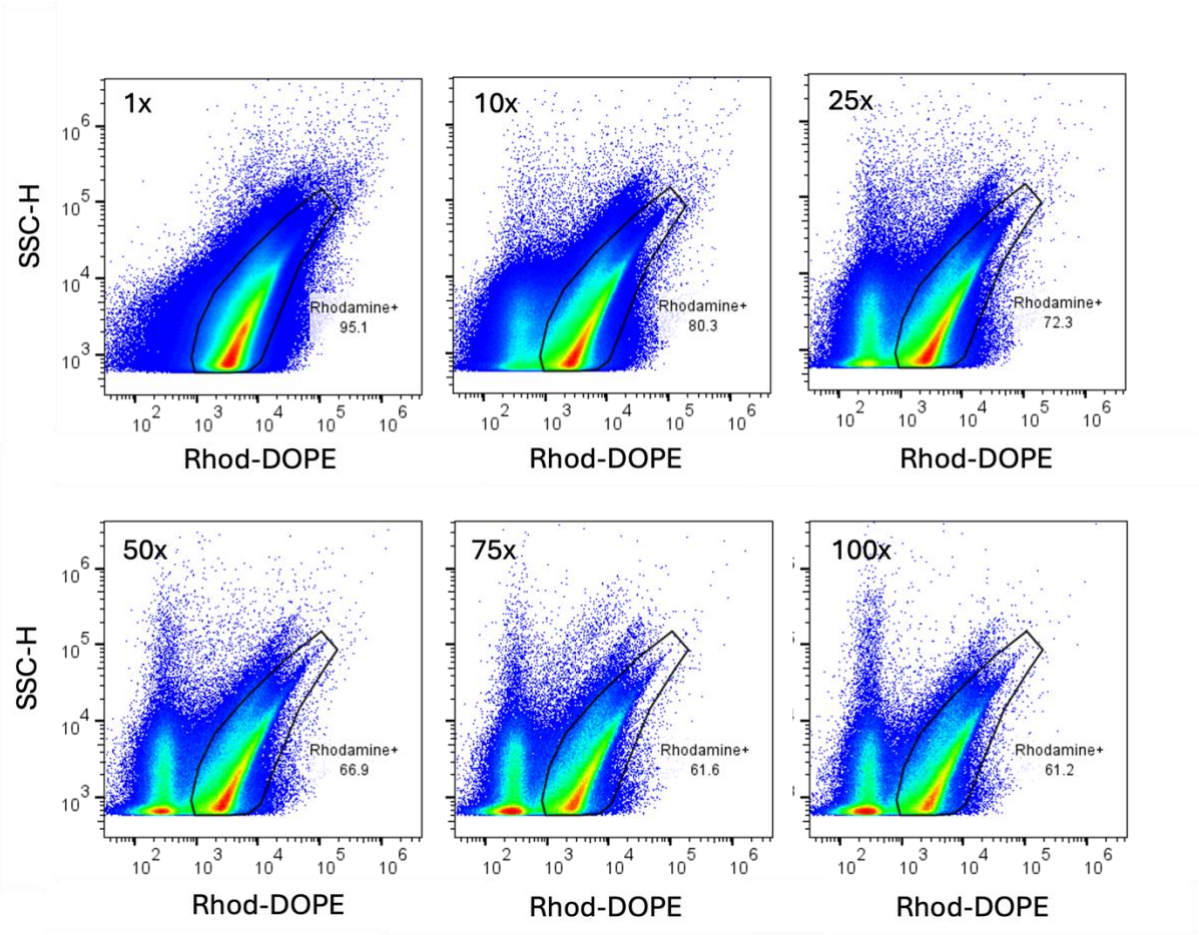

Figure 4.15 - Enhanced detection of LUVs made from lipids extracted from the nuclei of donor HO-M 273074. These dot plots demonstrate a striking similarity in distribution and appearance between the LUVs made from extracted lipids and those made from POPC. The samples were analysed at six different dilutions, with the first dot plot representing the original suspension, *i.e.*, the suspension immediately after extrusion, without any dilution.

By examining Figure 4.15, it is evident that the profile of the vesicles formed from extracted lipids closely mirrors that of the POPC vesicles. Despite the fact that these vesicles contain a variety of lipid species, the similarity in profiles suggests that the amount of dye added did not significantly affect the vesicles. Based on the considerations previously discussed, the 25-fold dilution was identified as the optimal choice for accurate vesicle counting. However, to ensure robustness, additional vesicles with varying dye concentrations were also examined to check for any potential changes (Figure 4.16).

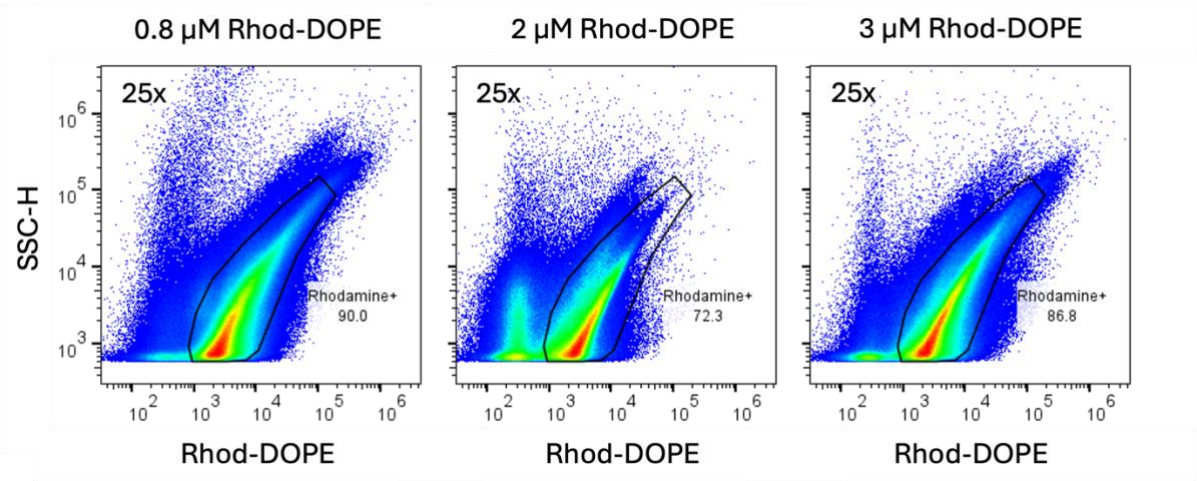

Figure 4.16 - Enhanced detection of LUVs made from lipids extracted from nuclei of donor HO-M 273074, with varying concentrations of Rhod-DOPE at the optimal dilution. The dot plots show that samples with Rhod-DOPE at concentration of 0.8, 2, and 3 µM exhibit very similar distributions. However, the dot plot for vesicles with Rhod-DOPE at 3 µM shows vesicles with higher complexity and increased fluorescence, which may be due to the excessive amount of the probe in the sample.

By observing Figure 4.16, no significant differences were detected in the side scatter of vesicles prepared with varying amounts of dye, except for the sample with Rhod-DOPE at 3 µM. In this case, a slight increase in side scatter, possibly due to aggregation, was observed, along with the expected increase in fluorescence from the higher dye concentration, leading to the exclusion of this sample due to the visible changes. Since no substantial differences were observed in the samples containing 0.8 and 2 µM Rhod-DOPE, it became necessary to rely on other characteristics to determine which sample would be optimal for vesicle counting. Therefore, the focus shifted to analysing the fluorescence data to identify which graph most accurately distinguishes the vesicles from other components (Figure 4.17).

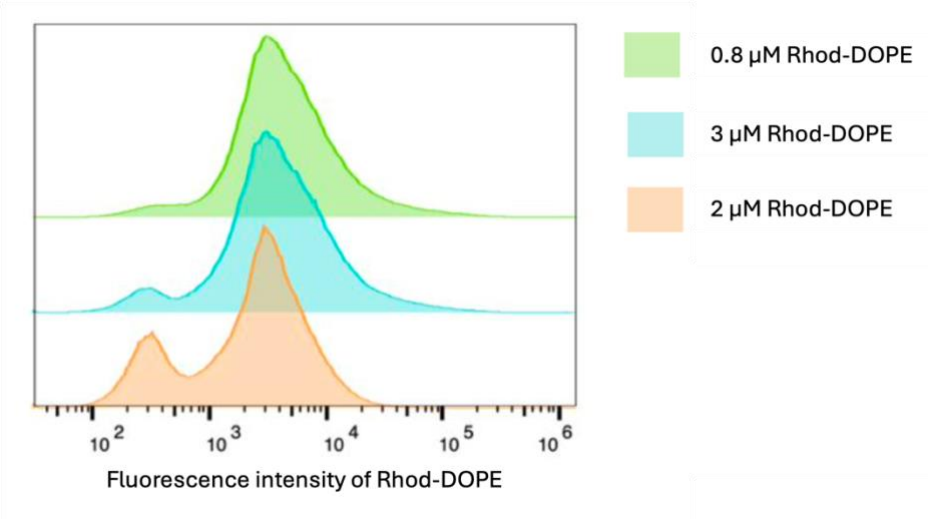

Figure 4.17 – Fluorescence histograms of LUVs made from extracted lipids with different concentrations of Rhod-DOPE. The histograms show that samples with the concentrations 2 and 3 μM of the probe produce two distinct peaks, whereas the sample with only 0.8 μM does not achieve this separation between the vesicles and the buffer and debris. Among the tested concentration, the sample with Rhod-DOPE at 2 μM demonstrates the best peak separation.

The histograms in Figure 4.17 indicate that the sample containing Rhod-DOPE at 2 μM concentration provided the clearest definition of two distinct peaks, allowing for the selection of the peak corresponding to the vesicles (the higher peak). This clear separation made the 2 μM sample the most suitable for vesicle counting.

Following this optimization, the protocol revealed a key correlation. In experiments with POPC vesicles, it was determined that a sample with a lipid concentration of 0.5 mM could form approximately 31,203,521 vesicles. In the subsequent experiment, using 259,141 nuclei, 26,900,000 vesicles were produced. Based on this data, the sample used to calculate Laurdan GP values and assess membrane order, which contained 196,682 nuclei, was estimated to have a lipid concentration of 0.16 mM in the lipid extract. This estimate allowed for the addition of an appropriate amount of Laurdan (1:100 lipid to probe ratio), ensuring that the probe did not influence the membrane properties of the vesicles.

Additionally, the protocol was tested with DiO, a fluorescent molecule that, unlike Rhod-DOPE, can be added externally after the formation of the lipid film. Although the method worked, further optimization is still necessary, as the concentration used was higher than required, leading to altered vesicle properties and unexpected complexities (data not shown).

After forming LUVs with the extracted lipids, Laurdan GP values were also determined for LUVs made from POPC and DPPC, which served as controls (Figure 4.18). POPC vesicles are known for having lower membrane order, corresponding to a fluid (liquid) phase, while DPPC vesicles are characterized by higher membrane order, which corresponds to a solid (gel) phase. These controls acted as beacons to understand in which region the vesicles made with extracted lipids were located.

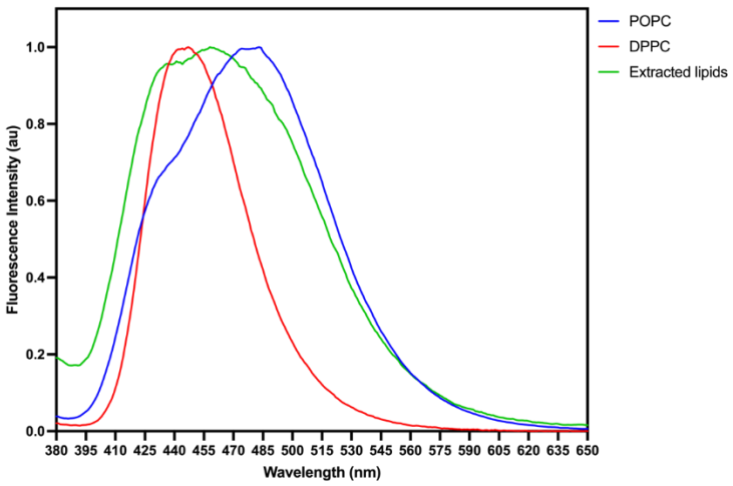

Figure 4.18 - Fluorescence emission spectra of Laurdan incorporated in POPC, DPPC, and nuclear lipid LUVs. DPPC LUVs show a reduced intensity at the higher wavelength shoulder of the spectrum, indicating higher membrane order. In contrast, the spectra for POPC and extracted lipid LUVs suggest greater membrane fluidity compared to DPPC LUVs, as indicated by the higher intensity at these wavelengths. The lipids were extracted from nuclei of donor HO-M 273074

The emission spectra reveal clear distinctions between the three lipid compositions. The calculated Laurdan GP values obtained according to equation (5) were -0.148 for POPC, 0.061 for vesicles made with the extracted lipids, and 0.481 for DPPC. These values for DPPC and POPC are consistent with those reported in the literature (~0.45 and -0.177 respectively), validating the results [152, 153]. The Laurdan GP value for the vesicles made from lipids of an older donor was found to be higher than that of the POPC vesicles. While this data suggests a difference in membrane order between these vesicles, it is crucial to avoid direct comparisons with the GP values of the nuclei, as different probes were used in these measurements. Since GP values are probe-specific and depend on each probe's sensitivity to the microenvironment, comparing the GP values of Laurdan-stained vesicles with those from nuclei labelled with Di-4-ANEPPDHQ would be inappropriate.

It is possible that the lipid composition of the NE tends toward a less ordered, more fluid-like state, closer to the liquid phase since the GP value is closer to the GP value of POPC LUVs. This lower membrane order could be crucial for nuclear functions, as increased fluidity might facilitate processes such as nuclear transport, chromatin organization, and interactions with the nuclear lamina, all of which require dynamic membrane properties. Further studies are needed to investigate this hypothesis, including conducting these assays with LUVs made from lipids extracted from young donors to assess the impact of ageing and to draw more definitive conclusions.

5. CONCLUSIONS AND PERSPECTIVES

This work offers a significant contribution to the field of cellular ageing by providing an in-depth analysis of the biomechanical and biophysical properties of the NE during human ageing. The development of a detergent-free nuclei isolation protocol represents a critical methodological advancement, enabling the precise study of NE structure and function without compromising lipid composition. The findings presented in this work reveal that ageing is associated with increased nuclear stiffness, increased membrane tension, and increased lipid order. These alterations are likely to impair the NE's role in maintaining nuclear-cytoplasmic communication, genome stability, and overall cellular homeostasis, thereby contributing to the onset of age-related diseases.

This research also pioneers the use of *in vitro* models, such as LUVs derived from aged nuclear lipids, to study the impact of lipid alterations on NE mechanics. These models provide a valuable tool for dissecting the molecular mechanisms underlying age-related changes in NE properties, offering new insights into the interplay between lipid composition, protein dynamics, and nuclear mechanics.

The implications of this research extend beyond the basic understanding of nuclear ageing. By identifying specific alterations in NE properties, this thesis highlights potential targets for therapeutic interventions. Furthermore, the methodologies developed in this study can be applied to other cellular models and pathological conditions, broadening the scope of future research.

Nevertheless, the complexity of nuclear ageing necessitates further investigation. Ongoing work is focused on extracting lipids from nuclei of both young donors and patients with HGPS, which will allow for a deeper understanding of lipid contributions to nuclear membrane properties. At the same time, the development of *in vitro* models continues, aiming to replicate the behaviour of the nuclear membrane in controlled environments. Additionally, efforts are being made to increase the sample size across all experiments conducted in this thesis to strengthen the robustness of the findings.

Future research should also prioritise replicating these experiments in intact cells to assess whether the nuclear membrane behaviour and measured parameters are consistent within a more physiological context. These ongoing steps, together with multi-omics approaches, will further illuminate the molecular drivers of nuclear ageing and help clarify whether targeted interventions could reverse these changes.

Overall, this thesis not only advances our understanding of NE changes during ageing but also establishes groundwork for developing new strategies to explore nuclear properties that were previously difficult to examine due to challenges in obtaining pure nuclei. Through this work, we underscore the importance of investigating the nucleus to better elucidate the mechanisms underlying ageing.

6. REFERENCES

1. Comfort, A. (1979). *The Biology of Senescence*. Elsevier.
2. Harman, D. (1981). The aging process. *Proceedings of the National Academy of Sciences of the United States of America*, *78*(11), 7124–7128. https://doi.org/10.1073/pnas.78.11.7124
3. Rose, M. R. (1994). *Evolutionary Biology of Aging*. Oxford, New York: Oxford University Press.
4. Gilbert, S. F., & Gilbert, S. F. (2000). *Developmental Biology* (6th ed.). Sinauer Associates.
5. The Hallmarks of Aging: Cell. (n.d.). Retrieved August 19, 2024, from https://www.cell.com/cell/fulltext/S0092-8674(13)00645-4?source=post_page----------
6. Behr, L. C., Simm, A., Kluttig, A., & Grosskopf Großkopf, A. (2023). 60 years of healthy aging: On definitions, biomarkers, scores and challenges. *Ageing Research Reviews*, *88*, 101934. https://doi.org/10.1016/j.arr.2023.101934
7. Kirkwood, T. B. L. (2005). Understanding the odd science of aging. *Cell*, *120*(4), 437–447. https://doi.org/10.1016/j.cell.2005.01.027
8. Kirkwood, T. B., & Austad, S. N. (2000). Why do we age? *Nature*, *408*(6809), 233–238. https://doi.org/10.1038/35041682
9. Hayflick, L. (1998). How and why we age. *Experimental Gerontology*, *33*(7–8), 639–653. https://doi.org/10.1016/s0531-5565(98)00023-0
10. Degenerative Disc Disease (DDD) Causes, Symptoms & Treatments. (n.d.). Retrieved August 19, 2024, from https://spineconnection.org/back-pain-conditions/degenerative-disc-disease/

11. St-Onge, M.-P., & Gallagher, D. (2010). Body composition changes with aging: The cause or the result of alterations in metabolic rate and macronutrient oxidation? *Nutrition (Burbank, Los Angeles County, Calif.)*, *26*(2), 152–155. https://doi.org/10.1016/j.nut.2009.07.004
12. Changes in the Body With Aging - Older People's Health Issues. (n.d.). *MSD Manual Consumer Version*. Retrieved August 19, 2024, from https://www.msdmanuals.com/en-jp/home/older-people's-health-issues/the-aging-body/changes-in-the-body-with-aging
13. Hou, Y., Dan, X., Babbar, M., Wei, Y., Hasselbalch, S. G., Croteau, D. L., & Bohr, V. A. (2019). Ageing as a risk factor for neurodegenerative disease. *Nature Reviews. Neurology*, *15*(10), 565–581. https://doi.org/10.1038/s41582-019-0244-7
14. Partridge, L., Deelen, J., & Slagboom, P. E. (2018). Facing up to the global challenges of ageing. *Nature*, *561*(7721), 45–56. https://doi.org/10.1038/s41586-018-0457-8
15. Healthy ageing and functional ability. (n.d.). Retrieved August 19, 2024, from https://www.who.int/news-room/questions-and-answers/item/healthy-ageing-and-functional-ability
16. Peel, N., Bartlett, H., & McClure, R. (2004). Healthy ageing: how is it defined and measured? *Australasian Journal on Ageing*, *23*(3), 115–119. https://doi.org/10.1111/j.1741-6612.2004.00035.x
17. Michel, jean-pierre, & Sadana, R. (2017). "Healthy Aging" Concepts and Measures. *Journal of the American Medical Directors Association*, *18*. https://doi.org/10.1016/j.jamda.2017.03.008
18. UN Decade of Healthy Ageing – The Platform. (n.d.). Retrieved August 19, 2024, from https://www.decadeofhealthyageing.org

19. Peel, N., Bartlett, H., & McClure, R. (2004). Healthy ageing: how is it defined and measured? *Australasian Journal on Ageing*, *23*(3), 115–119. https://doi.org/10.1111/j.1741-6612.2004.00035.x

20. Healthy ageing: A priority for delivering universal health coverage. (n.d.). Retrieved August 19, 2024, from https://www.who.int/publications/m/item/healthy-ageing--a-priority-for-delivering-universal-health-coverage

21. European Commission. Directorate General for Economic and Financial Affairs. (2024). *2024 ageing report: economic & budgetary projections for the EU Member States (2022 2070).* LU: Publications Office. Retrieved from https://data.europa.eu/doi/10.2765/022983

22. Guo, J., Huang, X., Dou, L., Yan, M., Shen, T., Tang, W., & Li, J. (2022). Aging and aging-related diseases: from molecular mechanisms to interventions and treatments. *Signal Transduction and Targeted Therapy*, *7*(1), 1–40. https://doi.org/10.1038/s41392-022-01251-0

23. Alberts, & Hunt, T. (2008). *Molecular biology of the cell* (Fifth ed.). New York: Garland Publishing.

24. Cell theory | Definition, History, Importance, Scientists, First Proposed, & Facts | Britannica. (n.d.). Retrieved August 19, 2024, from https://www.britannica.com/science/cell-theory

25. Ellinger, I., & Ellinger, A. (2014). Smallest Unit of Life: Cell Biology. In E. Jensen-Jarolim (Ed.), *Comparative Medicine* (pp. 19–33). Vienna: Springer Vienna. https://doi.org/10.1007/978-3-7091-1559-6_2

26. Schmauck-Medina, T., Molière, A., Lautrup, S., Zhang, J., Chlopicki, S., Madsen, H. B., … Fang, E. F. (2022). New hallmarks of ageing: a 2022 Copenhagen ageing meeting summary. *Aging*, *14*(16), 6829–6839. https://doi.org/10.18632/aging.204248

27. Gilbert, H. T. J., & Swift, J. (2019). The consequences of ageing, progeroid syndromes and cellular senescence on mechanotransduction and the nucleus. *Experimental Cell Research*, *378*(1), 98–103. https://doi.org/10.1016/j.yexcr.2019.03.002

28. Schmauck-Medina, T., Molière, A., Lautrup, S., Zhang, J., Chlopicki, S., Madsen, H. B., … Fang, E. F. (2022). New hallmarks of ageing: a 2022 Copenhagen ageing meeting summary. *Aging (Albany NY)*, *14*(16), 6829–6839. https://doi.org/10.18632/aging.204248

29. DUNDR, M., & MISTELI, T. (2001). Functional architecture in the cell nucleus. *Biochemical Journal*, *356*(2), 297–310. https://doi.org/10.1042/bj3560297

30. Holy, J., & Perkins, E. (2009). Structure and Function of the Nucleus and Cell Organelles. In S. Krawetz (Ed.), *Bioinformatics for Systems Biology* (pp. 3–31). Totowa, NJ: Humana Press. https://doi.org/10.1007/978-1-59745-440-7_1

31. Ungricht, R., & Kutay, U. (2017). Mechanisms and functions of nuclear envelope remodelling. *Nature Reviews Molecular Cell Biology*, *18*(4), 229–245. https://doi.org/10.1038/nrm.2016.153

32. Hetzer, M. W. (2010). The Nuclear Envelope. *Cold Spring Harbor Perspectives in Biology*, *2*(3), a000539. https://doi.org/10.1101/cshperspect.a000539

33. Dobrzynska, A., Gonzalo, S., Shanahan, C., & Askjaer, P. (2016). The nuclear lamina in health and disease. *Nucleus*, *7*(3), 233–248. https://doi.org/10.1080/19491034.2016.1183848

34. Kutay, U., & Hetzer, M. W. (2008). Reorganization of the Nuclear Envelope during Open Mitosis. *Current opinion in cell biology*, *20*(6), 669–677. https://doi.org/10.1016/j.ceb.2008.09.010

35. Systematic kinetic analysis of mitotic dis- and reassembly of the nuclear pore in living cells | Journal of Cell Biology | Rockefeller University Press. (n.d.). Retrieved August 6,

2024, from https://rupress.org/jcb/article/180/5/857/45209/Systematic-kinetic-analysis-of-mitotic-dis-and

36. Nuclear Pores Form de Novo from Both Sides of the Nuclear Envelope | Science. (n.d.). Retrieved August 6, 2024, from https://www.science.org/doi/abs/10.1126/science.1124196

37. Wilhelmsen, K., Litjens, S. H. M., Kuikman, I., Tshimbalanga, N., Janssen, H., van den Bout, I., … Sonnenberg, A. (2005). Nesprin-3, a novel outer nuclear membrane protein, associates with the cytoskeletal linker protein plectin. *Journal of Cell Biology*, *171*(5), 799–810. https://doi.org/10.1083/jcb.200506083

38. Blurring the Boundary: The Nuclear Envelope Extends Its Reach | Science. (n.d.). Retrieved August 6, 2024, from https://www.science.org/doi/abs/10.1126/science.1142034

39. Tzur, Y. B., Wilson, K. L., & Gruenbaum, Y. (2006). SUN-domain proteins: "Velcro" that links the nucleoskeleton to the cytoskeleton. *Nature Reviews Molecular Cell Biology*, *7*(10), 782–788. https://doi.org/10.1038/nrm2003

40. Razafsky, D., & Hodzic, D. (2009). Bringing KASH under the SUN: the many faces of nucleo-cytoskeletal connections. *The Journal of Cell Biology*, *186*(4), 461–472. https://doi.org/10.1083/jcb.200906068

41. Crisp, M., Liu, Q., Roux, K., Rattner, J. B., Shanahan, C., Burke, B., … Hodzic, D. (2006). Coupling of the nucleus and cytoplasm: role of the LINC complex. *The Journal of Cell Biology*, *172*(1), 41–53. https://doi.org/10.1083/jcb.200509124

42. Buchwalter, A., Kaneshiro, J. M., & Hetzer, M. W. (2019). Coaching from the sidelines: the nuclear periphery in genome regulation. *Nature Reviews Genetics*, *20*(1), 39–50. https://doi.org/10.1038/s41576-018-0063-5

43. Mimura, Y., & Imamoto, N. (2016). Nuclear Organization (Nuclear Structure and Dynamics). In *Encyclopedia of Cell Biology* (pp. 311–318). Elsevier. https://doi.org/10.1016/B978-0-12-394447-4.20027-8

44. Dauer, W. T., & Worman, H. J. (2009). The nuclear envelope as a signaling node in development and disease. *Developmental Cell*, *17*(5), 626–638. https://doi.org/10.1016/j.devcel.2009.10.016

45. Schirmer, E. C., & Gerace, L. (2005). The nuclear membrane proteome: extending the envelope. *Trends in Biochemical Sciences*, *30*(10), 551–558. https://doi.org/10.1016/j.tibs.2005.08.003

46. Olins, A. L., Hoang, T. V., Zwerger, M., Herrmann, H., Zentgraf, H., Noegel, A. A., … Olins, D. E. (2009). The LINC-less granulocyte nucleus. *European Journal of Cell Biology*, *88*(4), 203–214. https://doi.org/10.1016/j.ejcb.2008.10.001

47. Makatsori, D., Kourmouli, N., Polioudaki, H., Shultz, L. D., Mclean, K., Theodoropoulos, P. A., … Georgatos, S. D. (2004). The Inner Nuclear Membrane Protein Lamin B Receptor Forms Distinct Microdomains and Links Epigenetically Marked Chromatin to the Nuclear Envelope *. *Journal of Biological Chemistry*, *279*(24), 25567–25573. https://doi.org/10.1074/jbc.M313606200

48. Worman, H. J., & Schirmer, E. C. (2015). Nuclear membrane diversity: underlying tissue-specific pathologies in disease? *Current opinion in cell biology*, *34*, 101–112. https://doi.org/10.1016/j.ceb.2015.06.003

49. Dechat, T., Adam, S. A., Taimen, P., Shimi, T., & Goldman, R. D. (2010). Nuclear lamins. *Cold Spring Harbor Perspectives in Biology*, *2*(11), a000547. https://doi.org/10.1101/cshperspect.a000547

50. Nuclear envelope dysfunction and its contribution to the aging process - Martins - 2020 - Aging Cell - Wiley Online Library. (n.d.). Retrieved August 7, 2024, from https://onlinelibrary.wiley.com/doi/full/10.1111/acel.13143

51. Jiang, H., Zhang, X., Chen, X., Aramsangtienchai, P., Tong, Z., & Lin, H. (2018). Protein Lipidation: Occurrence, Mechanisms, Biological Functions, and Enabling Technologies. *Chemical Reviews*, *118*(3), 919–988. https://doi.org/10.1021/acs.chemrev.6b00750

52. Ray, A., Jatana, N., & Thukral, L. (2017). Lipidated proteins: Spotlight on protein-membrane binding interfaces. *Progress in Biophysics and Molecular Biology*, *128*, 74–84. https://doi.org/10.1016/j.pbiomolbio.2017.01.002

53. Gruenbaum, Y., Margalit, A., Goldman, R. D., Shumaker, D. K., & Wilson, K. L. (2005). The nuclear lamina comes of age. *Nature Reviews Molecular Cell Biology*, *6*(1), 21–31. https://doi.org/10.1038/nrm1550

54. Dittmer, T. A., & Misteli, T. (2011). The lamin protein family. *Genome Biology*, *12*(5), 222. https://doi.org/10.1186/gb-2011-12-5-222

55. Dechat, T., Adam, S. A., & Goldman, R. D. (2009). Nuclear Lamins and Chromatin: When Structure Meets Function. *Advances in Enzyme Regulation*, *49*(1), 157–166. https://doi.org/10.1016/j.advenzreg.2008.12.003

56. van Steensel, B., & Belmont, A. S. (2017). Lamina-associated domains: links with chromosome architecture, heterochromatin and gene repression. *Cell*, *169*(5), 780–791. https://doi.org/10.1016/j.cell.2017.04.022

57. Nmezi, B., Xu, J., Fu, R., Armiger, T. J., Rodriguez-Bey, G., Powell, J. S., … Padiath, Q. S. (2019). Concentric organization of A- and B-type lamins predicts their distinct roles in the spatial organization and stability of the nuclear lamina. *Proceedings of the*

National Academy of Sciences of the United States of America, *116*(10), 4307–4315. https://doi.org/10.1073/pnas.1810070116

58. Dickinson, R. B., & Lele, T. P. (2023). A new function for nuclear lamins: Providing surface tension to the nuclear drop. *Current Opinion in Biomedical Engineering*, *28*, 100483. https://doi.org/10.1016/j.cobme.2023.100483
59. Casares, D., Escribá, P. V., & Rosselló, C. A. (2019). Membrane Lipid Composition: Effect on Membrane and Organelle Structure, Function and Compartmentalization and Therapeutic Avenues. *International Journal of Molecular Sciences*, *20*(9), 2167. https://doi.org/10.3390/ijms20092167
60. Prudovsky, I., Vary, C. P. H., Markaki, Y., Olins, A. L., & Olins, D. E. (2012). Phosphatidylserine colocalizes with epichromatin in interphase nuclei and mitotic chromosomes. *Nucleus*, *3*(2), 200–210. https://doi.org/10.4161/nucl.19662
61. Ledeen, R. W., & Wu, G. (2008). Nuclear sphingolipids: metabolism and signaling. *Journal of Lipid Research*, *49*(6), 1176–1186. https://doi.org/10.1194/jlr.R800009-JLR200
62. Farooqui, A. A., Ong, W.-Y., & Farooqui, T. (2010). Lipid mediators in the nucleus: Their potential contribution to Alzheimer's disease. *Biochimica Et Biophysica Acta*, *1801*(8), 906–916. https://doi.org/10.1016/j.bbalip.2010.02.002
63. Sarmento, M. J., Llorente, A., Petan, T., Khnykin, D., Popa, I., Nikolac Perkovic, M., … Jaganjac, M. (2023). The expanding organelle lipidomes: current knowledge and challenges. *Cellular and Molecular Life Sciences*, *80*(8), 237. https://doi.org/10.1007/s00018-023-04889-3
64. Ramírez-Nuñez, O., Jové, M., Torres, P., Sol, J., Fontdevila, L., Romero-Guevara, R., … Portero-Otin, M. (2021). Nuclear lipidome is altered in amyotrophic lateral sclerosis:

A pilot study. *Journal of Neurochemistry*, *158*(2), 482–499. https://doi.org/10.1111/jnc.15373

65. The Inner Nuclear Membrane Is a Metabolically Active Territory that Generates Nuclear Lipid Droplets - PubMed. (n.d.). Retrieved August 7, 2024, from https://pubmed.ncbi.nlm.nih.gov/29937227/
66. Sharma, R., & Diwan, B. (2023). Lipids and the hallmarks of ageing: From pathology to interventions. *Mechanisms of Ageing and Development*, *215*, 111858. https://doi.org/10.1016/j.mad.2023.111858
67. Antonny, B., Vanni, S., Shindou, H., & Ferreira, T. (2015). From zero to six double bonds: phospholipid unsaturation and organelle function. *Trends in Cell Biology*, *25*(7), 427–436. https://doi.org/10.1016/j.tcb.2015.03.004
68. Casares, D., Escribá, P. V., & Rosselló, C. A. (2019). Membrane Lipid Composition: Effect on Membrane and Organelle Structure, Function and Compartmentalization and Therapeutic Avenues. *International Journal of Molecular Sciences*, *20*(9), 2167. https://doi.org/10.3390/ijms20092167
69. Understanding the diversity of membrane lipid composition | Nature Reviews Molecular Cell Biology. (n.d.). Retrieved August 7, 2024, from https://www.nature.com/articles/nrm.2017.138
70. Functional rafts in cell membranes | Nature. (n.d.). Retrieved August 7, 2024, from https://www.nature.com/articles/42408
71. Chorlay, A., & Thiam, A. R. (2020). Neutral lipids regulate amphipathic helix affinity for model lipid droplets. *Journal of Cell Biology*, *219*(4), e201907099. https://doi.org/10.1083/jcb.201907099
72. Hsieh, K., Lee, Y. K., Londos, C., Raaka, B. M., Dalen, K. T., & Kimmel, A. R. (2012). Perilipin family members preferentially sequester to either triacylglycerol-specific or

cholesteryl-ester-specific intracellular lipid storage droplets. *Journal of Cell Science*, *125*(Pt 17), 4067–4076. https://doi.org/10.1242/jcs.104943

73. Mutlu, A. S., Duffy, J., & Wang, M. C. (2021). Lipid metabolism and lipid signals in aging and longevity. *Developmental cell*, *56*(10), 1394–1407. https://doi.org/10.1016/j.devcel.2021.03.034

74. Sindelar, P. J., Guan, Z., Dallner, G., & Ernster, L. (1999). The protective role of plasmalogens in iron-induced lipid peroxidation. *Free Radical Biology & Medicine*, *26*(3–4), 318–324. https://doi.org/10.1016/s0891-5849(98)00221-4

75. Veyrat-Durebex, C., Bris, C., Codron, P., Bocca, C., Chupin, S., Corcia, P., … Blasco, H. (2019). Metabo-lipidomics of Fibroblasts and Mitochondrial-Endoplasmic Reticulum Extracts from ALS Patients Shows Alterations in Purine, Pyrimidine, Energetic, and Phospholipid Metabolisms. *Molecular Neurobiology*, *56*(8), 5780–5791. https://doi.org/10.1007/s12035-019-1484-7

76. Palikaras, K., Mari, M., Ploumi, C., Princz, A., Filippidis, G., & Tavernarakis, N. (2023). Age-dependent nuclear lipid droplet deposition is a cellular hallmark of aging in Caenorhabditis elegans. *Aging Cell*, *22*(4), e13788. https://doi.org/10.1111/acel.13788

77. Ahadi, S., Zhou, W., Schüssler-Fiorenza Rose, S. M., Sailani, M. R., Contrepois, K., Avina, M., … Snyder, M. (2020). Personal aging markers and ageotypes revealed by deep longitudinal profiling. *Nature Medicine*, *26*(1), 83–90. https://doi.org/10.1038/s41591-019-0719-5

78. Unfried, M., Ng, L. F., Cazenave-Gassiot, A., Batchu, K. C., Kennedy, B. K., Wenk, M. R., … Gruber, J. (2022). LipidClock: A Lipid-Based Predictor of Biological Age. *Frontiers in Aging*, *3*, 828239. https://doi.org/10.3389/fragi.2022.828239

79. Pathak, R. U., Soujanya, M., & Mishra, R. K. (2021). Deterioration of nuclear morphology and architecture: A hallmark of senescence and aging. *Ageing Research Reviews*, *67*, 101264. https://doi.org/10.1016/j.arr.2021.101264

80. Scaffidi, P., & Misteli, T. (2006). Lamin A-dependent nuclear defects in human aging. *Science (New York, N.Y.)*, *312*(5776), 1059–1063. https://doi.org/10.1126/science.1127168

81. Haithcock, E., Dayani, Y., Neufeld, E., Zahand, A. J., Feinstein, N., Mattout, A., … Liu, J. (2005). Age-related changes of nuclear architecture in Caenorhabditis elegans. *Proceedings of the National Academy of Sciences of the United States of America*, *102*(46), 16690–16695. https://doi.org/10.1073/pnas.0506955102

82. Brandt, A., Krohne, G., & Großhans, J. (2008). The farnesylated nuclear proteins KUGELKERN and LAMIN B promote aging-like phenotypes in Drosophila flies. *Aging Cell*, *7*(4), 541–551. https://doi.org/10.1111/j.1474-9726.2008.00406.x

83. Mechanical model of blebbing in nuclear lamin meshworks | PNAS. (n.d.). Retrieved August 19, 2024, from https://www.pnas.org/doi/full/10.1073/pnas.1300215110

84. Goldman, R. D., Shumaker, D. K., Erdos, M. R., Eriksson, M., Goldman, A. E., Gordon, L. B., … Collins, F. S. (2004). Accumulation of mutant lamin A causes progressive changes in nuclear architecture in Hutchinson-Gilford progeria syndrome. *Proceedings of the National Academy of Sciences of the United States of America*, *101*(24), 8963–8968. https://doi.org/10.1073/pnas.0402943101

85. Gordon, L. B., Rothman, F. G., López-Otín, C., & Misteli, T. (2014). Progeria: a paradigm for translational medicine. *Cell*, *156*(3), 400–407. https://doi.org/10.1016/j.cell.2013.12.028

86. Misteli, T., & Scaffidi, P. (2005). Genome instability in progeria: when repair gets old. *Nature Medicine*, *11*(7), 718–719. https://doi.org/10.1038/nm0705-718

87. Serebryannyy, L., & Misteli, T. (2018). Protein sequestration at the nuclear periphery as a potential regulatory mechanism in premature aging. *The Journal of Cell Biology*, *217*(1), 21–37. https://doi.org/10.1083/jcb.201706061

88. Rempel, I. L., Crane, M. M., Thaller, D. J., Mishra, A., Jansen, D. P., Janssens, G., … Veenhoff, L. M. (2019). Age-dependent deterioration of nuclear pore assembly in mitotic cells decreases transport dynamics. *eLife*, *8*, e48186. https://doi.org/10.7554/eLife.48186

89. Alterations in mitosis and cell cycle progression caused by a mutant lamin A known to accelerate human aging - PMC. (n.d.). Retrieved August 19, 2024, from https://www.ncbi.nlm.nih.gov/pmc/articles/PMC1829246/

90. Gonzalo, S., & Kreienkamp, R. (2015). DNA repair defects and genome instability in Hutchinson-Gilford Progeria Syndrome. *Current Opinion in Cell Biology*, *34*, 75–83. https://doi.org/10.1016/j.ceb.2015.05.007

91. Martins, F., Sousa, J., Pereira, C. D., da Cruz e Silva, O. A. B., & Rebelo, S. (2020). Nuclear envelope dysfunction and its contribution to the aging process. *Aging Cell*, *19*(5), e13143. https://doi.org/10.1111/acel.13143

92. Cameron, D. E., Bashor, C. J., & Collins, J. J. (2014). A brief history of synthetic biology. *Nature Reviews Microbiology*, *12*(5), 381–390. https://doi.org/10.1038/nrmicro3239

93. Wang, C., Zeng, H.-S., Liu, K.-X., Lin, Y.-N., Yang, H., Xie, X.-Y., … Ye, J.-W. (2023). Biosensor-based therapy powered by synthetic biology. *Smart Materials in Medicine*, *4*, 212–224. https://doi.org/10.1016/j.smaim.2022.10.003

94. Lee, T.-H., Charchar, P., Separovic, F., Reid, G. E., Yarovsky, I., & Aguilar, M.-I. (n.d.). The intricate link between membrane lipid structure and composition and

membrane structural properties in bacterial membranes. *Chemical Science*, *15*(10), 3408–3427. https://doi.org/10.1039/d3sc04523d

95. Punnamaraju, S., You, H., & Steckl, A. (2012). Triggered Release of Molecules across Droplet Interface Bilayer Lipid Membranes Using Photopolymerizable Lipids. *Langmuir : the ACS journal of surfaces and colloids*, *28*, 7657–64. https://doi.org/10.1021/la3011663
96. Siontorou, C. G., Nikoleli, G.-P., Nikolelis, D. P., & Karapetis, S. K. (2017). Artificial Lipid Membranes: Past, Present, and Future. *Membranes*, *7*(3), 38. https://doi.org/10.3390/membranes7030038
97. Skowronska-Krawczyk, D., & Budin, I. (2020). Aging membranes: unexplored functions for lipids in the lifespan of the central nervous system. *Experimental gerontology*, *131*, 110817. https://doi.org/10.1016/j.exger.2019.110817
98. Cassia-Moura, R. (2003). Chapter 19 - The quest for ion channel memory using a planar BLM. In H. T. Tien & A. Ottova-Leitmannova (Eds.), *Membrane Science and Technology* (Vol. 7, pp. 539–568). Elsevier. https://doi.org/10.1016/S0927-5193(03)80043-8
99. Giorno, L., Mazzei, R., & Drioli, E. (2010). 1.01 - Biological Membranes and Biomimetic Artificial Membranes. In E. Drioli & L. Giorno (Eds.), *Comprehensive Membrane Science and Engineering* (pp. 1–12). Oxford: Elsevier. https://doi.org/10.1016/B978-0-08-093250-7.00055-4
100. Montal, M., & Mueller, P. (1972). Formation of bimolecular membranes from lipid monolayers and a study of their electrical properties. *Proceedings of the National Academy of Sciences of the United States of America*, *69*(12), 3561–3566. https://doi.org/10.1073/pnas.69.12.3561

101. Mishra, S., & Khurana, M. (2022). A snapshot review: In vitro characterization of lipid membranes and their applications. *MRS Advances*, *7*(27), 551–561. https://doi.org/10.1557/s43580-022-00323-1

102. Sezgin, E., Levental, I., Mayor, S., & Eggeling, C. (2017). The mystery of membrane organization: composition, regulation and roles of lipid rafts. *Nature Reviews Molecular Cell Biology*, *18*(6), 361–374. https://doi.org/10.1038/nrm.2017.16

103. Reconstitution of membrane proteins into liposomes - PubMed. (n.d.). Retrieved August 19, 2024, from https://pubmed.ncbi.nlm.nih.gov/14610807/

104. Chan, Y.-H. M., & Boxer, S. G. (2007). Model Membrane Systems and Their Applications. *Current opinion in chemical biology*, *11*(6), 581–587. https://doi.org/10.1016/j.cbpa.2007.09.020

105. Allen, T. M., & Cullis, P. R. (2013). Liposomal drug delivery systems: from concept to clinical applications. *Advanced Drug Delivery Reviews*, *65*(1), 36–48. https://doi.org/10.1016/j.addr.2012.09.037

106. Phospholipid bilayers made from monolayers on patch-clamp pipettes. - PMC. (n.d.). Retrieved August 19, 2024, from https://www.ncbi.nlm.nih.gov/pmc/articles/PMC1329252/

107. Karlsson, A., Sott, K., Markström, M., Davidson, M., Konkoli, Z., & Orwar, O. (2005). Controlled Initiation of Enzymatic Reactions in Micrometer-Sized Biomimetic Compartments. *The Journal of Physical Chemistry B*, *109*(4), 1609–1617. https://doi.org/10.1021/jp0459716

108. Chen, Z. (2023). Using Micropatterned Supported Lipid Bilayers to Probe the Mechanosensitivity of Signaling Receptors. In R. Zaidel-Bar (Ed.), *Mechanobiology: Methods and Protocols* (pp. 283–289). New York, NY: Springer US. https://doi.org/10.1007/978-1-0716-2851-5_18

109. Dean, J. M., & Lodhi, I. J. (2018). Structural and functional roles of ether lipids. *Protein & Cell*, *9*(2), 196–206. https://doi.org/10.1007/s13238-017-0423-5

110. Thai, T. P., Rodemer, C., Jauch, A., Hunziker, A., Moser, A., Gorgas, K., & Just, W. W. (2001). Impaired membrane traffic in defective ether lipid biosynthesis. *Human Molecular Genetics*, *10*(2), 127–136. https://doi.org/10.1093/hmg/10.2.127

111. Hutterer, R., & Hof, M. (2001). Dynamics in Diether Lipid Bilayers and Interdigitated Bilayer Structures Studied by Time-Resolved Emission Spectra, Decay Time and Anisotropy Profiles. *Journal of Fluorescence*, *11*(3), 227–236. https://doi.org/10.1023/A:1012253218489

112. Dorninger, F., Herbst, R., Kravic, B., Camurdanoglu, B. Z., Macinkovic, I., Zeitler, G., … Berger, J. (2017). Reduced muscle strength in ether lipid-deficient mice is accompanied by altered development and function of the neuromuscular junction. *Journal of Neurochemistry*, *143*(5), 569–583. https://doi.org/10.1111/jnc.14082

113. Levitan, I. (2021). Evaluating membrane structure by Laurdan imaging: Disruption of lipid packing by oxidized lipids. *Current topics in membranes*, *88*, 235–256. https://doi.org/10.1016/bs.ctm.2021.10.003

114. Mierke, C. T. (2022). Viscoelasticity, Like Forces, Plays a Role in Mechanotransduction. *Frontiers in Cell and Developmental Biology*, *10*. https://doi.org/10.3389/fcell.2022.789841

115. Zmurchok, C., Collette, J., Rajagopal, V., & Holmes, W. (2020). Membrane Tension Can Enhance Adaptation to Maintain Polarity of Migrating Cells. *Biophysical journal*, *119*. https://doi.org/10.1016/j.bpj.2020.08.035

116. About Primary Cells - PT. (n.d.). Retrieved August 11, 2024, from https://www.thermofisher.com/uk/en/home/life-science/cell-culture/primary-cell-culture/primary-cell-culture-resources/about-primary-cells.html

117. Human Primary Cells Overview | STEMCELL Technologies. (n.d.). Retrieved August 11, 2024, from https://www.stemcell.com/human-primary-and-cultured-cells-overview.html

118. Primary Cell Culture Basics. (n.d.). Retrieved August 11, 2024, from https://www.sigmaaldrich.com/PT/en/technical-documents/technical-article/cell-culture-and-cell-culture-analysis/primary-cell-culture/primary-cell-culture

119. Dazzoni, R., Grélard, A., Morvan, E., Bouter, A., Applebee, C. J., Loquet, A., … Dufourc, E. J. (2020). The unprecedented membrane deformation of the human nuclear envelope, in a magnetic field, indicates formation of nuclear membrane invaginations. *Scientific Reports*, *10*(1), 5147. https://doi.org/10.1038/s41598-020-61746-0

120. Huang, X., Xing, X., Ng, C. N., & Yobas, L. (2019). Single-Cell Point Constrictions for Reagent-Free High-Throughput Mechanical Lysis and Intact Nuclei Isolation. *Micromachines*, *10*(7), 488. https://doi.org/10.3390/mi10070488

121. Ibrahim, S. F., & van den Engh, G. (2007). Flow Cytometry and Cell Sorting. In A. Kumar, I. Y. Galaev, & B. Mattiasson (Eds.), *Cell Separation: Fundamentals, Analytical and Preparative Methods* (pp. 19–39). Berlin, Heidelberg: Springer. https://doi.org/10.1007/10_2007_073

122. Cytek® Biosciences Adds Ability to Detect Subcellular Particles to Its Industry-Leading Cell Analysis Systems | Cytek Biosciences. (n.d.). Retrieved August 12, 2024, from https://investors.cytekbio.com/news-releases/news-release-details/cytekr-biosciences-adds-ability-detect-subcellular-particles-its/

123. Lakowicz, J. R. (Ed.). (2006). Instrumentation for Fluorescence Spectroscopy. In *Principles of Fluorescence Spectroscopy* (pp. 27–61). Boston, MA: Springer US. https://doi.org/10.1007/978-0-387-46312-4_2

124. Lakowicz, J. R. (Ed.). (2006). Introduction to Fluorescence. In *Principles of Fluorescence Spectroscopy* (pp. 1–26). Boston, MA: Springer US. https://doi.org/10.1007/978-0-387-46312-4_1

125. Elliott, A. D. (2020). Confocal Microscopy: Principles and Modern Practices. *Current protocols in cytometry*, *92*(1), e68. https://doi.org/10.1002/cpcy.68

126. Confocal Microscopy | Principle & Applications. (n.d.). *ibidi*. Retrieved August 12, 2024, from https://ibidi.com/content/216-confocal-microscopy

127. Mokobi, F. (2024, April 11). Confocal Microscope: Principle, Parts, Types, Diagram, Uses. Retrieved August 12, 2024, from https://microbenotes.com/confocal-microscope/

128. Datta, R., Heaster, T. M., Sharick, J. T., Gillette, A. A., & Skala, M. C. (2020). Fluorescence lifetime imaging microscopy: fundamentals and advances in instrumentation, analysis, and applications. *Journal of Biomedical Optics*, *25*(7), 071203. https://doi.org/10.1117/1.JBO.25.7.071203

129. Fluorescence Lifetime Imaging Microscopy (FLIM). (n.d.). *ibidi*. Retrieved August 12, 2024, from https://ibidi.com/content/219-flim

130. Alexiev, U., Volz, P., Boreham, A., & Brodwolf, R. (2017). Time-resolved fluorescence microscopy (FLIM) as an analytical tool in skin nanomedicine. *European Journal of Pharmaceutics and Biopharmaceutics*, *116*, 111–124. https://doi.org/10.1016/j.ejpb.2017.01.005

131. The bh TCSPC Handbook 10th edition, 2023. (n.d.). *Becker & Hickl GmbH*. Retrieved from https://www.becker-hickl.com/literature/documents/flim/the-bh-tcspc-handbook/

132. Lakowicz, J. R. (Ed.). (2006). Time-Domain Lifetime Measurements. In *Principles of Fluorescence Spectroscopy* (pp. 97–155). Boston, MA: Springer US. https://doi.org/10.1007/978-0-387-46312-4_4

133. Lakowicz, J. R. (Ed.). (2006). Frequency-Domain Lifetime Measurements. In *Principles of Fluorescence Spectroscopy* (pp. 157–204). Boston, MA: Springer US. https://doi.org/10.1007/978-0-387-46312-4_5

134. Benninger, R. K. P., & Piston, D. W. (2013). Two-photon excitation microscopy for the study of living cells and tissues. *Current Protocols in Cell Biology*, *Chapter 4*, 4.11.1-4.11.24. https://doi.org/10.1002/0471143030.cb0411s59

135. nanowizard_handbook-6.0d.pdf. (n.d.).

136. Egerton, R. F. (2016). The Transmission Electron Microscope. In R. F. Egerton (Ed.), *Physical Principles of Electron Microscopy: An Introduction to TEM, SEM, and AEM* (pp. 55–88). Cham: Springer International Publishing. https://doi.org/10.1007/978-3-319-39877-8_3

137. Stachowiak, G. W., Batchelor, A. W., & Stachowiak, G. B. (2004). 8 - Surface Micrography and Analysis. In G. W. Stachowiak, A. W. Batchelor, & G. B. Stachowiak (Eds.), *Tribology Series* (Vol. 44, pp. 165–220). Elsevier. https://doi.org/10.1016/S0167-8922(04)80024-5

138. Transmission electron microscopy – About Tribology. (2024, September 15). Retrieved from https://www.tribonet.org/wiki/transmission-electron-microscopy/

139. Lea, W. A., & Simeonov, A. (2011). Fluorescence Polarization Assays in Small Molecule Screening. *Expert opinion on drug discovery*, *6*(1), 17–32. https://doi.org/10.1517/17460441.2011.537322

140. Sanchez, S., Tricerri, A., Gunther, G., & Gratton, E. (2007). *Laurdan Generalized Polarization: from cuvette to microscope. Biochemistry* (Vol. 2).

141. Owen, D. M., Rentero, C., Magenau, A., Abu-Siniyeh, A., & Gaus, K. (2012). Quantitative imaging of membrane lipid order in cells and organisms. *Nature Protocols*, *7*(1), 24–35. https://doi.org/10.1038/nprot.2011.419

142. Yu, W., So, P. T., French, T., & Gratton, E. (1996). Fluorescence generalized polarization of cell membranes: a two-photon scanning microscopy approach. *Biophysical Journal*, *70*(2), 626–636. https://doi.org/10.1016/S0006-3495(96)79646-7

143. da Costa, E., Melo, T., Moreira, A. S. P., Bernardo, C., Helguero, L., Ferreira, I., … Domingues, M. R. (2017). Valorization of Lipids from Gracilaria sp. through Lipidomics and Decoding of Antiproliferative and Anti-Inflammatory Activity. *Marine Drugs*, *15*(3), 62. https://doi.org/10.3390/md15030062

144. Lamis, A., Siddiqui, S. W., Ashok, T., Patni, N., Fatima, M., & Aneef, A. N. (n.d.). Hutchinson-Gilford Progeria Syndrome: A Literature Review. *Cureus*, *14*(8), e28629. https://doi.org/10.7759/cureus.28629

145. Huang, H.-L., Hsing, H.-W., Lai, T.-C., Chen, Y.-W., Lee, T.-R., Chan, H.-T., … Chan, H.-L. (2010). Trypsin-induced proteome alteration during cell subculture in mammalian cells. *Journal of Biomedical Science*, *17*(1), 36. https://doi.org/10.1186/1423-0127-17-36

146. Guilak, F., Tedrow, J. R., & Burgkart, R. (2000). Viscoelastic Properties of the Cell Nucleus. *Biochemical and Biophysical Research Communications*, *269*(3), 781–786. https://doi.org/10.1006/bbrc.2000.2360

147. Sugitate, T., Kihara, T., Liu, X.-Y., & Miyake, J. (2009). Mechanical role of the nucleus in a cell in terms of elastic modulus. *Current Applied Physics*, *9*(4, Supplement), e291–e293. https://doi.org/10.1016/j.cap.2009.06.020

148. A fluorescent membrane tension probe | Nature Chemistry. (n.d.). Retrieved September 17, 2024, from https://www.nature.com/articles/s41557-018-0127-3

149. Hannich, J. T., Umebayashi, K., & Riezman, H. (2011). Distribution and Functions of Sterols and Sphingolipids. *Cold Spring Harbor Perspectives in Biology*, *3*(5), a004762. https://doi.org/10.1101/cshperspect.a004762

150. Doole, F. T., Kumarage, T., Ashkar, R., & Brown, M. F. (2022). Cholesterol Stiffening of Lipid Membranes. *The Journal of Membrane Biology*, *255*(4–5), 385–405. https://doi.org/10.1007/s00232-022-00263-9

151. Mesa-Herrera, F., Taoro-González, L., Valdés-Baizabal, C., Diaz, M., & Marín, R. (2019). Lipid and Lipid Raft Alteration in Aging and Neurodegenerative Diseases: A Window for the Development of New Biomarkers. *International Journal of Molecular Sciences*, *20*(15), 3810. https://doi.org/10.3390/ijms20153810

152. Amaro, M., Reina, F., Hof, M., Eggeling, C., & Sezgin, E. (2017). Laurdan and Di-4-ANEPPDHQ probe different properties of the membrane. *Journal of Physics D Applied Physics*, *50*. https://doi.org/10.1088/1361-6463/aa5dbc

153. Bonarska-Kujawa, D., Pruchnik, H., & Kleszczyńska, H. (2012). Interaction of selected anthocyanins with erythrocytes and liposome membranes. *Cellular & molecular biology letters*, *17*, 289–308. https://doi.org/10.2478/s11658-012-0010-y